

Marine Cloud Brightening

On the Effects of Aerosol Injection on Marine Stratocumulus in DALES Simulations

S.W. de Baat

Delft University of Technology

Marine Cloud Brightening

On the Effects of Aerosol Injection on Marine Stratocumulus in DALES Simulations

by

S.W. de Baat

to obtain the degree of Master of Science
in Spaceflight - Space Exploration
at the Delft University of Technology,
to be defended publicly on Thursday August 12, 2021 at 14:00

Student number: 4420950
Project duration: September 11, 2020 – August 12, 2021
Thesis committee: Dr. D.M. Stam, TU Delft, supervisor
Dr. S.R. de Roode, TU Delft, supervisor
Dr. Ir. W. van der Wal, TU Delft, chair
Dr. P.M. Visser, TU Delft, external examiner

An electronic version of this thesis is available at <http://repository.tudelft.nl/>.

Abstract

Due to the insufficient worldwide efforts to reduce greenhouse gas emissions and related global warming, marine cloud brightening (MCB) is gaining interest as an instrument to artificially lower Earth's temperature. MCB is based on exploiting the aerosol-cloud effects to enhance the albedo of stratocumulus clouds and prolong their lifetime by injecting clouds with sea salt aerosols. As there are still many uncertainties in the expected output of MCB due to the unresolved questions related to cloud processes and feedback mechanisms, this thesis aims to assess the efficacy of MCB to enhance solar radiation reflection of stratocumulus clouds using the turbulence-resolving Dutch Atmospheric Large-Eddy Simulation model.

This assessment is made by investigating which cloud properties and processes that determine the cloud's radiative forcing are affected by the aerosol injection for different meteorological conditions and injection strategies in 30-hour simulations. The simulation domain has a horizontal size of $25.2 \times 25.2 \text{ km}^2$ and 2 km in the vertical, with a mesh size of 100 m horizontally and 20 m vertically. The two studied cloud cases are based on the measurements of the first and second research flights of the DYCOMS-II field experiment and are characteristic for a shallow stratocumulus-topped boundary layer (STBL). The investigated surface aerosol injection strategies are a horizontally uniform source and a point source that is restricted to a single grid cell. In addition, an assessment is made of the effects of differences in aerosol number concentrations between the STBL and the free troposphere on the cloud's aerosol number concentration and radiative properties. This is done in 6-hour simulations with and without a uniform aerosol source, based on the second research flight of DYCOMS-II. The simulated horizontal domain is $3.2 \times 3.2 \text{ km}^2$ and 2 km in the vertical, with a mesh size of 25 m horizontally and 20 m vertically.

Our simulations showed that boundary layers with relatively low background aerosol concentrations were most effective in generating a negative radiative forcing, compensating slightly less than half of the forcing related to the CO_2 doubling in the atmosphere. For boundary layers with an average background aerosol concentration, the radiative forcing approaches a quarter of this value, which diminishes to negligible effects for boundary layers with relatively high background aerosol concentrations. For precipitating boundary layers, the enhanced radiative forcing is mainly caused by its suppressing effect on precipitation. For non-precipitating boundary layers, the reduction in cloud droplet size showed to be the primary source of the enhancement. No pronounced differences in efficacy were found when using a homogeneously distributed aerosol source or a point source. For the two studied cloud cases, investigation of the contributions to changes in the liquid water path showed that to exploit the effect of aerosol injection on the liquid water path, it is most effective to suppress precipitation and enhance cloud cover.

The differences in aerosol number concentration between the STBL and the free troposphere significantly and consistently altered the aerosol number concentration in the cloud layer due to the entrainment of air from just above the cloud-top into the cloud layer. This indicates that these differences in aerosol number concentration need to be considered when modelling MCB, as they change the intended aerosol number concentration enhancement and thereby affect their cloud-modifying effects.

Preface

At the start of my second year of the Master's Spaceflight at the TU Delft, I had to decide on the topic of my thesis study. Fascinated by the idea of terraforming (creating Earth-like and habitable environments on other planets) at that time, I explored the possibilities of researching this topic for my thesis. This way, I came across the various concepts of geoengineering, which can be regarded as terraforming Earth itself. Through exploratory conversations with prof. Russchenberg and dr. De Roode, I eventually learned about marine cloud brightening and found my topic of choice.

As the concept of marine cloud brightening largely overlaps with the field of geosciences and in a lesser manner with aerospace engineering, I would like to express my gratitude to my supervisors dr. Stam and dr. De Roode for providing me with the opportunity to set up my thesis research at the faculty of Aerospace Engineering in conjunction with the faculty of Geosciences. I want to thank dr. De Roode for his enthusiastic guidance and discussions during the many (digital) meetings over the past academic year. Although my thesis work needed to be done from home entirely, and our discussions were nearly completely online due to the Corona pandemic, I believe we have made the best of the situation and were able to have fruitful discussions nonetheless. Secondly, I want to thank dr. Stam for her guidance of my thesis process in general and her feedback during the catch-up meetings. Our meetings were very helpful for defining and demarcating what (and specifically what not) would be investigated in my research, and for the composition of my thesis report.

Last of all, I would like to thank my family, friends and girlfriend for their interest in my project, their great support during busy and sometimes stressful times, their valuable comments on my initial report, the fun study days at the VU Amsterdam and tolerating my endless rambling about clouds, aerosols and crashing simulations.

S.W. de Baat
Rotterdam, July 2021

Contents

| | |
|---|------------|
| Abstract | iii |
| Preface | v |
| Nomenclature | ix |
| List of Figures | xi |
| List of Tables | xvi |
| 1 Introduction | 1 |
| 1.1 Motivation | 1 |
| 1.1.1 Global Warming | 1 |
| 1.1.2 Geoengineering | 1 |
| 1.1.3 Marine Cloud Brightening | 2 |
| 1.2 Research Objectives and Questions | 3 |
| 1.3 Outline | 4 |
| 2 Theoretical Background | 5 |
| 2.1 First Indirect Aerosol Effect. | 5 |
| 2.2 Second Indirect Aerosol Effect. | 8 |
| 2.2.1 The Role of Precipitation. | 9 |
| 2.2.2 The Role of Entrainment. | 9 |
| 2.3 Previous LES Research on MCB | 12 |
| 3 Methodology | 15 |
| 3.1 Dutch Atmospheric Large-Eddy Simulation | 15 |
| 3.2 Model Extensions | 16 |
| 3.2.1 Implementation of cloud droplet number concentration parameterisation | 16 |
| 3.2.2 Point Source Surface Flux. | 18 |
| 3.3 Case Description: DYCOMS-II | 19 |
| 3.3.1 Shared Parameters. | 20 |
| 3.3.2 Research Flight 02 | 20 |
| 3.3.3 Research Flight 01 | 20 |
| 3.4 General Settings | 21 |
| 4 Validation | 23 |
| 4.1 Simulation Setup. | 23 |
| 4.1.1 Aerosol Input | 24 |
| 4.1.2 Settings and Simulation Domain | 24 |
| 4.2 Validation of Model Adjustments | 24 |
| 4.3 Output Comparison with Other LES Models. | 25 |
| 5 Cloud Seeding Simulations | 29 |
| 5.1 Additional Theoretical Background | 29 |
| 5.1.1 Alternative Definition of Albedo | 30 |
| 5.1.2 LWP Tendency Contributors. | 31 |

| | | |
|----------|---|-----------|
| 5.2 | Simulation Setup. | 33 |
| 5.2.1 | Aerosol Input | 33 |
| 5.2.2 | Settings and Simulation Domain | 34 |
| 5.3 | Results: Wet STBL with Average and Clean Pollution Levels | 34 |
| 5.3.1 | Reflection Enhancement. | 34 |
| 5.3.2 | LWP Budget Analysis | 40 |
| 5.3.3 | Summary. | 44 |
| 5.4 | Results: Dry STBL with Average and Clean Pollution Levels | 45 |
| 5.4.1 | Reflection Enhancement. | 45 |
| 5.4.2 | LWP Budget Analysis | 49 |
| 5.4.3 | Summary. | 52 |
| 5.5 | Results: Wet and Dry STBL with High Pollution Levels | 53 |
| 5.5.1 | Reflection Enhancement. | 53 |
| 5.5.2 | LWP Budget Analysis | 56 |
| 5.5.3 | Summary. | 56 |
| 6 | Entrainment Aerosol Transport Simulations | 59 |
| 6.1 | Additional Theoretical Background | 59 |
| 6.2 | Simulation Setup. | 60 |
| 6.2.1 | Aerosol Input | 60 |
| 6.2.2 | Settings and Simulation Domain | 60 |
| 6.3 | Results: Excluding Surface Aerosol Source. | 61 |
| 6.4 | Results: Including Surface Aerosol Source | 64 |
| 7 | Conclusions and Recommendations | 67 |
| 7.1 | Conclusions | 67 |
| 7.2 | Recommendations. | 70 |
| A | Governing Equations of DALES | 79 |
| B | Choice of Advection Scheme For Aerosols | 81 |
| B.1 | The Kappa Advection Scheme | 81 |
| B.2 | The 52 Advection Scheme | 83 |
| B.3 | Conservation in the Kappa Advection Scheme | 83 |
| C | Additional Figures to MCB Simulations | 85 |
| C.1 | Two-Dimensional Figures for the W50 Experiments | 85 |
| C.2 | Indications of Decoupling. | 87 |
| D | Derivation of the Change of Aerosol Number Concentration in Time | 89 |
| E | Horizontal Boundary Nudging | 91 |

Nomenclature

Abbreviations

| Abbreviation | Definition |
|-----------------|---|
| ACK09 | Ackerman et al. (2009) |
| CCN | cloud condensation nuclei |
| CO ₂ | carbon dioxide |
| DALES | Dutch Atmospheric Large-Eddy Simulation |
| DNS | direct numerical simulations |
| DYCOMS-II | Second Dynamics and Chemistry of Marine Stratocumulus field study |
| GABLS | GEWEX Atmospheric Boundary Layers Study |
| GCCS | GEWEX Cloud System Study |
| GCM | general circulation models |
| KNMI | Royal Netherlands Meteorological Institute |
| LES | large-eddy simulation |
| MCB | marine cloud brightening |
| NaCl | sodium chloride |
| RF01 | research flight 01 |
| RF02 | research flight 02 |
| STBL | stratocumulus-topped boundary layer |
| WANG11 | Wang et al. (2011) |

Symbols

| Symbol | Definition | Unit |
|-------------------------|--|-------------------------------------|
| A | effective albedo | - |
| A_c | cloud albedo | - |
| c_p | specific heat at constant pressure | $\text{J kg}^{-1} \text{K}^{-1}$ |
| D | large-scale divergence rate | s^{-1} |
| D_c | geometrical cloud thickness | m |
| g | Earth's gravitational acceleration | m s^{-2} |
| h | cloud thickness | m |
| H | boundary layer depth | m |
| L_v | latent heat of evaporation | J g^{-1} |
| LWP | liquid water path | g m^{-2} |
| N_{ae} | aerosol number concentration | m^{-3} |
| N_{ae}^c | cloud-averaged aerosol number concentration | m^{-3} |
| N_{ae}^+ | aerosol number concentration just above the inversion height | m^{-3} |
| N_{ae}^- | aerosol number concentration just below the inversion height | m^{-3} |
| $N_{ae,g}$ | aerosol number concentration | kg^{-1} |
| N_d | cloud droplet number concentration | m^{-3} |
| $n(r)$ | drop number size distribution | m^{-4} |
| $q_{c,min}$ | cloud specific humidity threshold | kg kg^{-1} |
| q_l | liquid water mixing ratio | kg kg^{-1} |
| q_s | saturation specific humidity | kg kg^{-1} |
| q_t | total water mixing ratio | kg kg^{-1} |
| r | cloud droplet radius | m |
| r_e | effective radius | m |
| r_v | volume mean radius | m |
| $R_{r,base}$ | precipitation rate at cloud-base | mm day^{-1} |
| $R_{r,sfc}$ | precipitation rate at the surface | mm day^{-1} |
| RH_{FT} | relative humidity of the free-troposphere | - |
| S_0 | solar constant | W m^{-2} |
| $S_{N_{ae}}$ | surface spraying rate | $\text{m}^{-2} \text{s}^{-1}$ |
| SW_d | downwelling shortwave radiation | W m^{-2} |
| $SW_{d,sfc}$ | downwelling shortwave radiation reaching the surface | W m^{-2} |
| SW_u | upwelling shortwave radiation | W m^{-2} |
| T | temperature | K |
| u | westerly wind | m s^{-1} |
| v | southerly wind | m s^{-1} |
| w_e | entrainment rate | m s^{-1} |
| w_{ls} | large-scale vertical wind | m s^{-1} |
| $\bar{w}(z_i)$ | large-scale vertical velocity of the inversion height | m s^{-1} |
| $\frac{w'q_t^b}{w'q_t}$ | turbulent flux of the total water mixing ratio at the cloud-base | $\text{m s}^{-1} \text{kg kg}^{-1}$ |

| Symbol | Definition | Unit |
|--------------------------|---|-----------------------------------|
| $\overline{w'\theta'_l}$ | turbulent flux of the liquid water potential temperature at the cloud-base | $\text{m s}^{-1} \text{K}$ |
| $z_{c,base}$ | cloud-base height | m |
| z_i | inversion height | m |
| $z_{c,top}$ | cloud-top height | m |
| γ | change of saturation specific humidity with temperature | $\text{kg kg}^{-1} \text{K}^{-1}$ |
| δF_{rad} | difference between the longwave radiation at cloud-top and cloud-base | K m s^{-1} |
| δP | difference between the precipitation rate at cloud-top and cloud-base | K m s^{-1} |
| $\bar{\Delta}$ | grid size | m |
| ΔF | radiative forcing | W m^{-2} |
| η | accounts for the latent heat release and uptake due to condensation and evaporation | - |
| θ | potential temperature | K |
| θ_l | liquid water potential temperature | K |
| θ_z | solar zenith angle | degrees |
| Γ_{ql} | lapse rate of the liquid water specific humidity | $\text{kg kg}^{-1} \text{m}^{-1}$ |
| Π | Exner function | K K^{-1} |
| ρ_{air} | density of air | kg m^{-3} |
| ρ_w | liquid water density | kg m^{-3} |
| P_s | source density | km^{-2} |
| τ | optical thickness | - |

List of Figures

| | | |
|-----|--|----|
| 1.1 | Ship tracks observed by NASA's Aqua satellite in the eastern Pacific Ocean, representing the local albedo enhancement due to pollution from ship exhaust. The image is a natural-color image acquired on January 20, 2013 (Schmaltz, 2013). | 3 |
| 2.1 | The albedo and lifetime effect. Polluted clouds (bottom illustrations) contain more aerosols than clean clouds (top illustrations), causing an increase in cloud droplet number concentration and a reduction in cloud droplet radius, which ultimately leads to an increase in cloud brightness: the albedo effect. More aerosols lead to the suppression of precipitation as well, allowing the clouds to deepen and prolong their lifetime: the lifetime effect. The figure is obtained from Stevens and Feingold (2009) to which cloud droplets are added to clarify the albedo effect. | 5 |
| 2.2 | Mean cloud droplet number concentration versus sub-cloud aerosol number concentration with a minimum diameter of $0.10 \mu\text{m}$ of all DYCOMS-II research flights (Twohy et al., 2005). The solid line represents the regressive fit, described by the presented equation, with a correlation coefficient of determination of $r^2 = 0.90$. Flight numbers are given below the data points. The error bars indicate one standard deviation from the mean data. This fit is utilised to translate aerosol number concentrations to cloud droplet number concentrations. Note that this parameterisation is only valid in the measured range of approximately 60 to 400 cm^{-3} | 7 |
| 2.3 | Schematic overview of cloud adjustments and feedback mechanisms due to a reduction in cloud droplet size and cloud droplet number concentration enhancement (Karsset et al., 2020). | 8 |
| 2.4 | The two bounding mixing types of entrained free-tropospheric air within the cloud layer and their effect on cloud droplet number concentration and size (Karsset et al., 2020). Homogeneous mixing (left) causes partial evaporation of all the cloud droplets, such that their size is reduced and the number of cloud droplets remains unchanged. Extreme inhomogeneous mixing (right) causes some cloud droplets to evaporate completely, while the other cloud droplets remain unaffected. This way, the number of cloud droplets is reduced, but their size is unchanged. | 10 |
| 3.1 | Schematic representation of eddy filtering by Large-Eddy Simulation models (Sagaut, 2006). On the left various eddy length scales are shown on a grid with grid size $\bar{\Delta}$ in physical space. The right-hand-side shows the eddies' kinetic energy as a function of its length scale in Fourier space. In this schematic view, eddies with a smaller length scale than $\bar{\Delta}$ (or smaller wavenumber than $\frac{\pi}{\bar{\Delta}}$) are not resolved in the LES model. | 16 |
| 3.2 | Schematic top-view representation of regarding a single point source in the simulated domain with horizontal periodic boundary conditions as a sub-domain of a larger system of evenly-spaced point sources. | 19 |

| | | |
|-----|---|----|
| 3.3 | Idealised initial mean states of θ_l (left) and q_t (right) from Research Flight 01 and 02 (Ackerman et al., 2009; Stevens et al., 2005). Each profile is described by a two-layered structure and is used to initialize the performed simulations. | 21 |
| 4.1 | Time series of the domain-averages of (a) liquid water path, (b) entrainment rate, (c) the maximum of the variance in vertical velocity w and (d) the surface precipitation of the RF02 case. 'standard' (blue) represents the results of the unmodified standard DALES model, '+microphysics' (orange) represents the results after including the aerosol-cloud droplet parameterisation in the scheme treating the microphysics, and '+radiation' (green) represents the results after including both the aerosol-cloud droplet parameterisation in both the microphysics scheme and the radiation scheme. The black dotted lines represent the approximate ranges of the observations. | 25 |
| 4.2 | Time- and horizontally-averaged vertical profiles of (a) the liquid water potential temperature θ_l , (b) the total water mixing ratio q_t , (c) the liquid water mixing ratio q_l , (d) cloud fraction, (e) precipitation flux, (f) total flux of θ_l (including radiation and precipitation flux), (g) total flux of q_t (including precipitation flux), (h) buoyancy flux, (i) variance of the vertical velocity and (j) the skewness in the vertical velocity of the RF02 case. Time-averages are taken over the last four hours of the six-hour simulations. The coloured lines are represented as in Figure 4.1. | 26 |
| 5.1 | Effective albedo (left) and downwelling shortwave radiation at the surface (right) versus LWP at sunrise, noon and sunset, showing the dependency of the cloud's reflective capability on the angle at which the solar radiation enters the cloud layer. All other physical conditions are unchanged among the varying LWP and time of day, which therefore do not affect the cloud albedo. ΔA is the difference between albedo at sunrise and at noon. | 30 |
| 5.2 | Time series of the RF02 case with an average maritime aerosol number concentration (100 cm^{-3}), showing the domain-averaged values of: (a) effective albedo A and cloud albedo A_c , (b) difference in downwelling shortwave radiation at the domain surface with respect to the base case without aerosol source (here W100) $\Delta SW_{d,sfc}$, (c) cloud cover, (d) difference in liquid water path with respect to the base case ΔLWP , (e) cloud-top $z_{c,top}$ and cloud-base $z_{c,base}$, (f) cloud-base precipitation rate $R_{r,base}$ and surface precipitation rate $R_{r,sfc}$ and (g) average in-cloud cloud droplet number concentration N_d . The blue line indicates the base case, the orange line represents the case with a uniform aerosol source, and green represents the case with an aerosol point source. Subfigures (b) and (d) include an additional plot showing the trend of respectively $SW_{d,sfc}$ and LWP to indicate the order of magnitude of the parameters and their evolution in time. Shading between 0 and 5 hours and between 19 and 29.5 hours represents nighttime during the simulations. | 37 |
| 5.3 | Same as Figure 5.2, but for a clean maritime aerosol number concentration ($N_{ae,kg} = 50 \text{ cm}^{-3}$). | 38 |

| | | |
|------|---|----|
| 5.4 | Time series of the different contributions to the tendencies in LWP for the RF02 case with an average maritime aerosol number concentration (100 cm^{-3}), showing: (a) the total tendency determined with the budget equations of Van der Dussen et al. (2014) (solid lines) and directly obtained from the output (dotted), and the tendency contributions of (b) entrainment, (c) turbulent fluxes in q_t and θ_l near the cloud-base, (d) difference in net radiation at cloud-top and cloud-base, (e) difference in precipitation rate between cloud-top and cloud-base and (f) subsidence. The blue line indicates the base case using no aerosol source, the orange line represents the case with a uniform aerosol source, and green represents the case with an aerosol point source. Shading between 0 and 5 hours and between 19 and 19.5 hours represents nighttime during the simulations. | 42 |
| 5.5 | Same as Figure 5.4, but for a clean maritime aerosol number concentration ($N_{ae,kg} = 50 \text{ cm}^{-3}$). | 43 |
| 5.6 | Same as Figure 5.2, but for the drier and warmer RF01 case, with an average maritime aerosol number concentration ($N_{ae,kg} = 100 \text{ cm}^{-3}$). | 46 |
| 5.7 | Same as Figure 5.2, but for the drier and warmer RF01 case, with a polluted maritime aerosol number concentration ($N_{ae,kg} = 50 \text{ cm}^{-3}$). | 47 |
| 5.8 | Same as Figure 5.4, but for the drier and warmer RF01 case, with an average maritime aerosol number concentration ($N_{ae,kg} = 100 \text{ cm}^{-3}$). | 50 |
| 5.9 | Same as Figure 5.4, but for the drier and warmer RF01 case, with a polluted maritime aerosol number concentration ($N_{ae,kg} = 50 \text{ cm}^{-3}$). | 51 |
| 5.10 | Same as Figure 5.2, but with a polluted maritime aerosol number concentration ($N_{ae,kg} = 200 \text{ cm}^{-3}$). | 54 |
| 5.11 | Same as Figure 5.2, but for the drier and warmer RF01 case, with a polluted maritime aerosol number concentration ($N_{ae,kg} = 200 \text{ cm}^{-3}$). | 55 |
| 5.12 | Same as Figure 5.4, but with a polluted maritime aerosol number concentration ($N_{ae,kg} = 200 \text{ cm}^{-3}$). | 57 |
| 5.13 | Same as Figure 5.4, but for the drier and warmer RF01 case, with a polluted maritime aerosol number concentration ($N_{ae,kg} = 200 \text{ cm}^{-3}$). | 58 |
| 6.1 | Domain-averaged differences of cloud properties to those of the 0W100 experiment with a vertically uniform aerosol number concentration (N_{ae}), for simulations with a range of negative and positive jumps in N_{ae} across the inversion layer. No surface aerosol source is applied in these simulations. The legend labels represent the experiments as presented in Table 6.1. The Figures on the left side show the results of the experiments with a negative jump in N_{ae} across the inversion layer. On the right side, the results of a positive jump are shown. Figures (a1) and (a2) show the difference in N_{ae} averaged over the cloud layer, (b1) and (b2) the difference in inversion height, (c1) and (c2) the difference in entrainment rate, (d1) and (d2) the difference in precipitation rate near the cloud-base, (e1) and (e2) the difference in LWP and (f1) and (f2) the difference in cloud albedo. | 62 |
| 6.2 | Same as in Figure 6.1, with the addition of a uniform surface aerosol source applied in the simulations. The domain-averaged differences in cloud properties are again with respect to those of the 0W100 experiment. | 65 |

| | | |
|-----|---|----|
| C.1 | Cloud albedo A_c for every horizontal grid point at 6 hours, 9 hours, 12 hours, 15 hours and 18 hours into the simulation of the W50 experiments. The top row illustrations show the results of the unseeded W50 experiment, the middle row corresponds to the uniformly seeded W50-U experiment and the bottom row corresponds to the point source seeded W50-P experiments. | 85 |
| C.2 | Same as in Figure C.1, but showing the liquid water path LWP. | 86 |
| C.3 | Same as in Figure C.1, but showing the aerosol number concentration N_{ae} , integrated in the vertical. Values are clipped to a maximum of $275 \cdot 10^4 \text{ mm}^{-2}$ to prevent the results to be obscured by the highly concentrated values near the point source. | 87 |
| C.4 | The vertical profiles of the buoyancy flux (top) and vertical velocity variance for the W100 simulations. The values of all figures are clipped for visual clarity. . . | 88 |
| C.5 | Same as in Figure C.4, but for the drier and warmer D100 simulations. | 88 |
| E.1 | Example of a horizontal domain with an initial N_{ae} of 200 cm^{-3} , which is nudged to 0 cm^{-3} towards the edges using a cosine function starting at 20 grid points from each edge. | 92 |

List of Tables

| | | |
|-----|---|----|
| 5.1 | Overview of the MCB experiments. The dry (D) and wet (W) conditions correspond to the research flights RF01 and RF02, respectively. The uniform injection method refers to the uniform injection of aerosols across the entire surface area. The point source injection method indicates the aerosol injection from a single grid point of the surface area, located at the upwind corner of the domain. | 33 |
| 5.2 | Domain- and time-averaged effective albedo (\bar{A}), cloud albedo (\bar{A}_c), downwelling shortwave radiation at the surface ($\overline{SW}_{d,src}$) and their relative changes compared to the baseline simulations for the RF02 case with average (100 cm^{-3}) and clean (50 cm^{-3}) initial maritime aerosol number concentrations. The time-averages are taken over the last 24 hours of the 30-hour simulations. | 35 |
| 5.3 | Same as in Table 5.2, but for the drier and warmer RF01 case. | 35 |
| 5.4 | Same as in Table 5.2, but for both RF02 case and the drier and warmer RF01 case, with polluted (200 cm^{-3}) initial maritime aerosol number concentrations. | 35 |
| 6.1 | Overview of the entrainment aerosol transport experiments. The same notation as in 5.1 is used with an additional prefix resembling the difference in aerosol number concentration between the STBL and the free troposphere ($\Delta N_{ae,kg} = N_{ae,kg}^- - N_{ae,kg}^+$), expressed as a percentage of the aerosol concentration in the STBL. | 60 |

Introduction

This chapter introduces the main subject of this thesis, marine cloud brightening (MCB), by starting with the motivation behind the concept and why research on this matter is necessary. Secondly, this thesis' research objectives and questions will be provided, after which the outline of the remaining part of the report will be given.

1.1. Motivation

1.1.1. Global Warming

In 2015, 189 countries signed and ratified the Paris Climate Agreement. In this agreement, the parties express the commitment to undertake actions to reduce greenhouse gas emissions rapidly in order to hold the global temperature increase below 2°C above preindustrial levels and pursue efforts to limit a 1.5°C increase. Despite their expressed commitments, research by the Intergovernmental Panel on Climate Change (IPCC, 2019) shows that even if all stated actions will be implemented, a significant gap of greenhouse gasses to be reduced remains. On top of that, various studies, such as that of IPCC (2019) and Olivier and Peters (2020), show that nearly all countries have increased their greenhouse gas emissions since signing the agreement. This does not only call for a thorough review and update of the mitigating strategy, but gives rise to investigating alternative options to suppress global warming as well. These alternatives, known as geoengineering or climate engineering, could provide more time to reduce the emission of greenhouse gasses to the required level.

1.1.2. Geoengineering

The general concept of geoengineering is to counteract the effects of changes in atmospheric chemistry by large-scale engineering of our environment (Vaughan and Lenton, 2011). It aims to restore the balance of incoming (shortwave) solar radiation and outgoing (longwave) radiation. Geoengineering can be divided into two categories: carbon dioxide removal, which aims to capture carbon dioxide out of the air, and solar radiation management, which aims to reflect sunlight back into space partially. In this thesis, one concept of solar radiation management will be considered, namely the concept of marine cloud brightening.

Despite the scientific call for more research on geoengineering, the debate on whether more research and potential future deployment should be desired has grown considerably, especially on SRM techniques (Galbraith, 2021). Opponents of the research state the concerns about the potential loss of momentum on mitigation strategies and the uncertainties of actual outputs of the technologies, which may cause severe adverse side-effects. On the other

hand, proponents suggest that these side-effects appear to be less dangerous than those of significant temperature rises (Salter et al., 2008) and refer to the current pollution of Earth's atmosphere as uncontrolled climate engineering. They say that only with (early-state) research the risks and uncertainties can be properly assessed, and the optimal governance strategy can be determined for its potential implementation (Galbraith, 2021). In addition, they argue that these preliminary studies do not pose any threat to human welfare or the environment.

The debate moves more and more to the public domain, as can be noted by increased attention in newspapers such as the scientific special on geoengineering in the NRC (Wismans, 2020). Regardless of whether the public opinion shifts to either pro or con geoengineering, improved knowledge about its potential benefits, adverse effects, effectiveness and uncertainties contributes to a constructive debate and future public acceptance when deciding to either employ or refute the technique.

1.1.3. Marine Cloud Brightening

MCB is a technique that makes use of the indirect effects of added aerosols in the marine boundary layer (Latham, 1990). By seeding the marine boundary layer with sea salt aerosols, the reflectivity and longevity of marine stratocumulus clouds can be increased. This results in a reduced net radiative flux in the atmosphere, known as the radiative forcing, and global surface temperature. The physical processes behind this concept will be further described in Chapter 2. A commonly used benchmark to assess SRM techniques is its capability to provide a negative radiative forcing of $\Delta F = 3.7 \text{ W m}^{-2}$, which is associated with the offset of CO_2 doubling since the industrial revolution (Connolly et al., 2014). To offset a global radiative forcing of 3.7 W m^{-2} , calculations show that the mean radiative forcing resulting from seeding marine stratocumulus should be 21.1 W m^{-2} for the total area of suitable stratocumulus clouds, based on the crude assumptions that the oceans cover about 70% of the global surface, the fraction of the oceanic surface covered by non-overlapped marine stratiform clouds is 0.25, and all suitable oceanic stratiform clouds are seeded, which is similar to a cloud albedo enhancement of $\Delta A_c = 0.062$ (Latham et al., 2008).

Aerosol seeding is proposed to be done by conventional vessels or by (yet-to-be-developed) autonomous, wind-driven vessels (Salter et al., 2008). A mist of seawater is sprayed into the boundary layer from these vessels, where the salt particles act as cloud condensation nuclei. The effect of increased albedo is already noticeable in daily life, as the air is being seeded with additional cloud condensation nuclei by pollution. These human-altered clouds are commonly illustrated by the ship tracks, long and narrow clouds formed due to water vapour condensing on the aerosols emitted in the exhaust of ships, as shown in Figure 1.1 (Schmaltz, 2013).

Studies of Salter et al. (2008) and Vaughan and Lenton (2011) showed that MCB is considered to be one of the most technically and financially feasible SRM techniques. However, there is still much uncertainty on the actual output of the technique. There are significant gaps in our understanding of the feedback mechanisms between micro- and macrophysical cloud properties (Latham et al., 2012). This results in the inability to predict the beneficial effects and adverse effects of MCB accurately. Further research on this matter is needed to validate the viability of MCB to counteract global warming before moving on to (small-scale) field experiments. Therefore, this thesis aims to improve this knowledge by examining these processes in the light of MCB simulations. Although the importance of ethical, political, and governance considerations on the employment of MCB is recognised, it will not be discussed in this thesis.

Multiple previous studies have investigated MCB, using both global climate models and higher

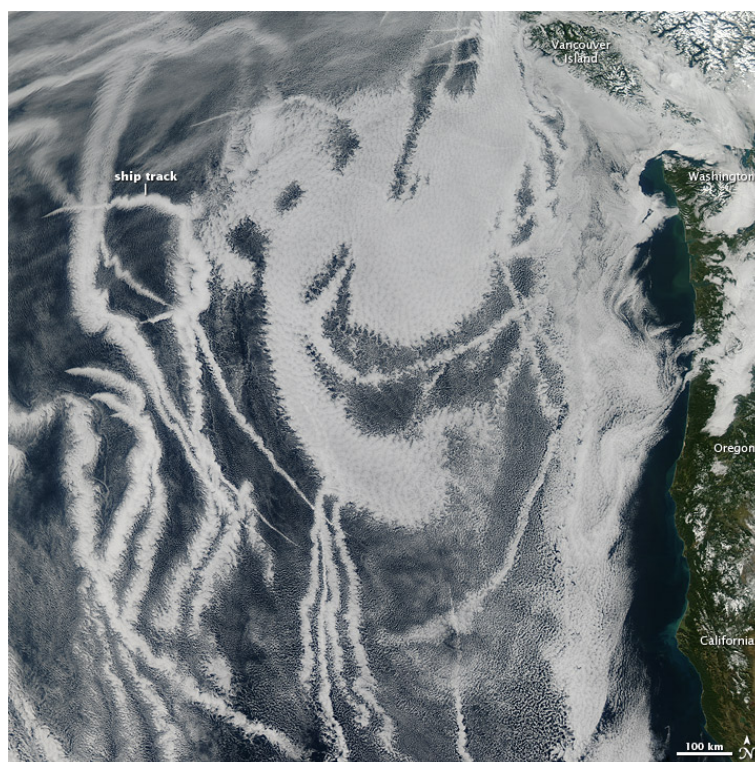


Figure 1.1: Ship tracks observed by NASA's Aqua satellite in the eastern Pacific Ocean, representing the local albedo enhancement due to pollution from ship exhaust. The image is a natural-color image acquired on January 20, 2013 (Schmaltz, 2013).

resolution models. The conclusions of the studies that are relevant for this thesis, more specifically the studies of Wang et al. (2011), Jenkins et al. (2013), and Possner et al. (2018), will be discussed in Section 2.3 after the theoretical background is provided, as this is helpful to understand their results.

1.2. Research Objectives and Questions

The main research objective of this thesis is to assess the effectiveness of deploying MCB to counter global warming by performing and analysing large-eddy simulation (LES) simulations that simulate cloud processes altered by aerosol injection. This research will be mainly focused on the inter-comparison with the study of Wang et al. (2011) (WANG11 from this point onward), who researched the responses of multiple cloud seeding strategies using a mesoscale cloud-resolving model (the Advanced Research WRF model in the LES mode). Their results show promising effects for MCB deployment on reducing the incoming solar radiation and a strong sensitivity of cloud properties to aerosol concentration enhancement. However, cloud-resolving models are known to being unable to simulate small scale mixing processes accurately (Wood and Ackerman, 2013). This is particularly the case for cloud-top entrainment, the mixing of air from just above the cloud-top into the cloud layer, which is a critical process in the response to aerosol concentration modifications. In addition, the results of one simulation model are insufficient to state scientifically valuable conclusions on the effectiveness of MCB. Thus, additional research with other simulation models and improved treatment of the mixing processes is required to predict the effects of MCB experiments accurately. In this thesis, an LES model will be used to simulate the same two meteorological cases and similar seeding strategies as in WANG11, but with an enhanced grid resolution. The results of these simulations will be analysed and compared to the results of WANG11.

To expand upon the earlier research, this thesis aims to assess the effectiveness of MCB under various negative and positive aerosol number concentration jumps between the atmospheric boundary layer and the free troposphere. Mixing of free-tropospheric air and the air at the top of the atmospheric boundary layer might cause aerosol number concentrations in the cloud layer to significantly increase or drop (depending on the sign of the concentration jump), which can affect the usefulness of MCB deployment. Results of these simulations will be compared to simulations with a vertically uniform aerosol number concentration. These two research objectives lead to the following research questions:

- How does surface aerosol injection affect marine stratocumulus cloud properties that determine its radiative forcing?
- How do increased aerosol concentrations affect the liquid water path and what are the main drivers of induced changes?
- What is the effect of aerosol concentration jumps between the atmospheric boundary layer and the free troposphere on radiation-affecting cloud properties and how does this affect the efficacy of MCB?

Although this thesis focuses on the processes affecting cloud brightness, it is noted that this thesis shines light upon more fundamental aerosol-cloud processes as well. As this is still an active field of research with many unsolved complexities, this subject is of broad interest.

1.3. Outline

The remaining part of this thesis consists of 6 chapters. In Chapter 2, the theoretical background for the physics controlling the effects of aerosol injection is provided, as well as previous research on MCB that use LES models and the background theory of the applied analysis methods. Next, the methodology is discussed, in which the introduction to the LES model, the modifications made to this model, the initial meteorological conditions and the general setup for the simulations are explained. Chapter 4 provides the methodology of the validation, after which the results are presented and discussed. The additional theoretical background, methodology, results and discussion of the cloud seeding simulations resembling the setup of WANG11 are presented in Chapter 5. The same is done for the simulations involving inversion jumps in aerosol number concentration in Chapter 6. The conclusions and recommendations for future research are provided in Chapter 7.

2

Theoretical Background

This chapter discusses the theoretical background to provide an overview of the relevant cloud physics, literature, and theory behind the analysis methodology. First, the physical processes that govern the effect of aerosol injection are provided, after which the findings of previous LES research on MCB are stated. Next, the background to the analysis methodology is provided.

2.1. First Indirect Aerosol Effect

The first indirect effect (also known as the Twomey or albedo effect) is the effect of aerosols on the optical thickness of a cloud and thereby on its albedo, assuming a constant liquid water path (LWP). First described by Twomey (1974), aerosols can act as cloud condensation nuclei to form cloud drops, which increases the cloud drop number concentration (N_d) and decreases the effective radius r_e of the cloud drops. A smaller r_e leads to an increase in optical depth and cloud albedo. This way, more solar radiation is reflected back into space, causing a cooling effect on Earth's surface. This effect is shown in Figure 2.1 by the upper two and lower two illustrations on the left side of the figure, showing a brighter cloud with more and smaller cloud droplets for the polluted cloud compared to the clean cloud.

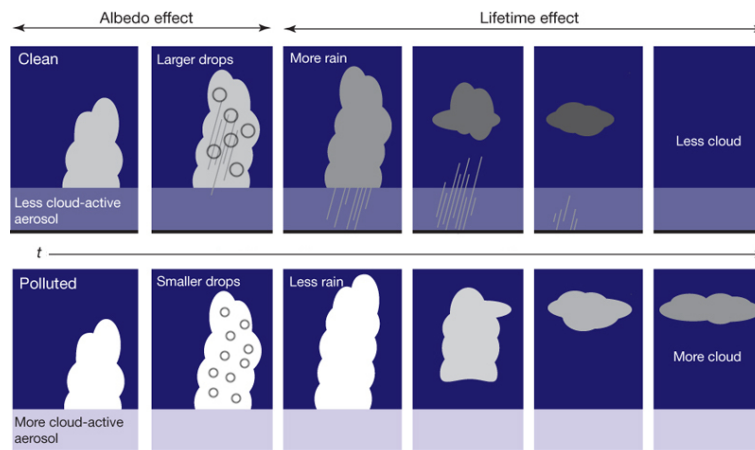


Figure 2.1: The albedo and lifetime effect. Polluted clouds (bottom illustrations) contain more aerosols than clean clouds (top illustrations), causing an increase in cloud droplet number concentration and a reduction in cloud droplet radius, which ultimately leads to an increase in cloud brightness: the albedo effect. More aerosols lead to the suppression of precipitation as well, allowing the clouds to deepen and prolong their lifetime: the lifetime effect. The figure is obtained from Stevens and Feingold (2009) to which cloud droplets are added to clarify the albedo effect.

The relation between LWP, r_e and cloud albedo can mathematically be shown, starting with the relation between cloud albedo and cloud optical thickness. An often used parameterisation for the mean cloud albedo of stratocumulus that shows the direct dependence on optical thickness is the expression of Zhang et al. (2005) (who follow Equation (19) of the study of Lacis and Hansen (1974) in their expression for the cloud albedo):

$$A_c = \frac{\tau}{6.8 + \tau}, \quad (2.1)$$

where A_c is the mean cloud albedo, τ is the cloud's optical thickness and the constant 6.8 is an empirically determined factor by Zhang et al. (2005) to fit their data. τ is then defined by:

$$\tau \approx \beta \pi \int_{D_c} \int_r r^2 n(r, z) dr dz, \quad (2.2)$$

where β is approximately equal to 2, D_c is the geometrical cloud thickness (ranging from cloud-base height to cloud-top height, defined as the height up to which the specific humidity $q_l > 0$ kg kg⁻¹), r is the cloud drop radius and $n(r, z)$ is the drop number size distribution within a cloud unit volume at the height z (Feingold et al., 2017). The next step in the derivation is the formulation of the LWP:

$$LWP = \int_z \rho_{air} q_l dz \quad (2.3)$$

Here, ρ_{air} is the air density in units of kg m⁻³ and q_l in kg kg⁻¹ (Zhang et al., 2005). The last step required for the expression combining τ , LWP and r_e , is defining the expression for r_e , which is a weighted mean of the cloud droplets' size distribution (Feingold et al., 2017):

$$r_e(z) = \frac{\int r^3 n(r, z) dr}{\int r^2 n(r, z) dr} \quad (2.4)$$

Combining Eqs. (2.2), (2.3) and (2.4), the equation for τ as a function of LWP and r_e is obtained:

$$\tau = \int_z \frac{3}{2} \frac{\rho_{air} q_l}{\rho_w r_e(z)} dz, \quad (2.5)$$

where ρ_w is the density of liquid water. For a constant LWP in time, the inverse relation between τ and r_e shows that by decreasing the effective cloud drop radius, due to increased N_d through cloud seeding, the optical thickness and albedo of the stratocumulus cloud are enhanced.

To relate r_e to N_d , the definition of the parameter k and the volume mean radius of the cloud drop size distribution r_v are used (Lu et al., 2007):

$$k = \frac{r_v^3}{r_e^3} = \frac{3\rho_{air} q_l}{4\pi r_e^3 \rho_w N_d} \quad (2.6)$$

Solving for r_e gives:

$$r_e = \left(\frac{4}{3} \pi \rho_w k \right)^{-1/3} (\rho_{air} q_l)^{1/3} N_d^{-1/3} \quad (2.7)$$

The result is the theoretical proof of reducing r_e by increasing N_d , which leads to an enhancement in albedo when all other parameters in Eq. (2.7) are assumed to be unaffected (Feingold et al., 2017).

The increasing N_d and decreasing r_e for increasing aerosol concentration is validated in practice by various field experiments, such as those of Twohy et al. (2005) and Lu et al. (2007). The results of the study by Twohy et al. (2005) are important in this thesis, as it forms the foundation

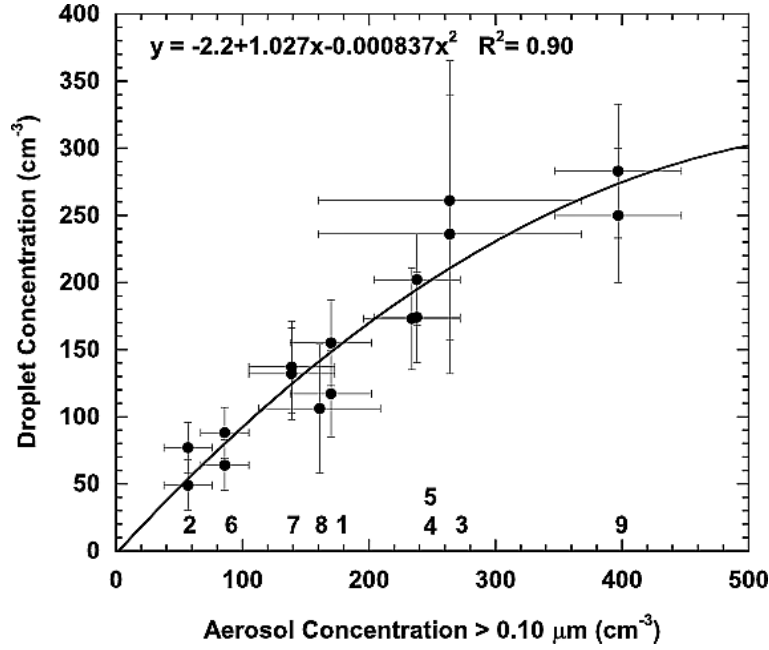


Figure 2.2: Mean cloud droplet number concentration versus sub-cloud aerosol number concentration with a minimum diameter of $0.10 \mu\text{m}$ of all DYCOMS-II research flights (Twohy et al., 2005). The solid line represents the regressive fit, described by the presented equation, with a correlation coefficient of determination of $r^2 = 0.90$. Flight numbers are given below the data points. The error bars indicate one standard deviation from the mean data. This fit is utilised to translate aerosol number concentrations to cloud droplet number concentrations. Note that this parameterisation is only valid in the measured range of approximately 60 to 400 cm^{-3} .

of the aerosol activation parameterisation (see Section 3.2.1). Twohy et al. (2005) analysed the measurements of the nine research flights of the DYCOMS-II field study (of which two are used as a meteorological case in this study, see Section 3.3) and fitted the cloud droplet concentrations against the sub-cloud aerosol number concentrations. When only aerosols with a minimum diameter of $0.10 \mu\text{m}$ are taken into account, which make up about 90% of the measured size distribution, a correlation coefficient of $r = 0.95$ is determined, indicating a strong correlation between N_d and N_{ae} . The retrieved equation for the N_{ae} -to- N_d parameterisation is given by:

$$N_d = -2.2 + 1.027N_{ae} - 0.000837N_{ae}^2, \quad (2.8)$$

where both N_d and N_{ae} are in cm^{-3} . This regressive fit, shown in Figure 2.2 is only valid in the measured N_{ae} interval, which ranges from approximately 60 to 400 cm^{-3} . The mean diameter of $0.8 \mu\text{m}$, which is the suggested size for the injected aerosols by Salter et al. (2008), is well above the minimum diameter of $0.10 \mu\text{m}$ for which the regression is made.

In addition, an equivalent anti-correlation between r_e and N_d ($r_e \sim N_d^{-1/3}$), as shown in Eq. (2.7), was found to close approximation by Twohy et al. (2005) for the relation between r_e and N_{ae} throughout the cloud layer ($r_e \sim N_{ae}^{-1/3}$). As the relation between N_d and N_{ae} is nearly linear for small values of N_{ae} , it may be assumed that also $r_e \sim N_d^{-1/3}$ for relatively small N_d . These relations play a significant roll for the first indirect aerosol effect. Looking at Eq. (2.5), the optical thickness is enhanced for decreasing r_e . Eq. (2.4) indicates that when the cloud contains larger cloud drops, r_e is increased. When few (soluble) aerosols are accessible for cloud droplet activation, the cloud drops can grow to larger sizes than when more of these aerosols were accessible. When many aerosols are accessible for activation, the cloud drops compete for the accessible water vapor. This suppresses individual drops to grow much beyond the size of the other particles and keeps the value for r_e small.

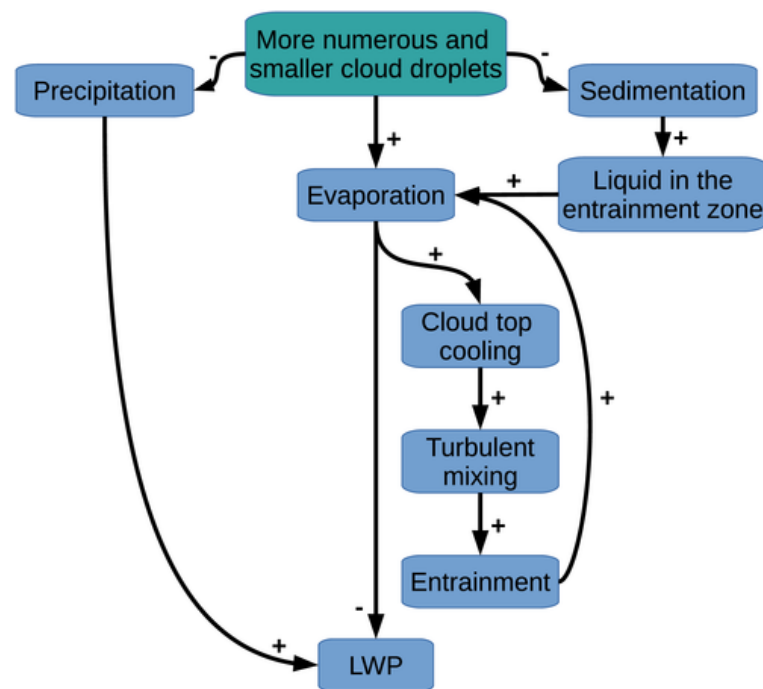


Figure 2.3: Schematic overview of cloud adjustments and feedback mechanisms due to a reduction in cloud droplet size and cloud droplet number concentration enhancement (Karset et al., 2020).

2.2. Second Indirect Aerosol Effect

The second indirect effect of aerosols on clouds was first described by Albrecht (1989) and is also known as the lifetime effect. It describes their macrophysical effect on the cloud's height, lifetime and water content. As stated earlier, the injection of aerosols causes the number of cloud droplets to increase and reduce in size. This has various effects on the cloud condition:

- The smaller cloud droplets are likely to reduce drop growth by collision and coalescence, resulting in the suppression of raindrop formation and precipitation (Latham et al., 2008).
- Precipitation often initiates cloud dissipation, which means that suppressing precipitation may prolong the lifetime of the cloud and increases cloud coverage (see Figure 2.1).
- Reduced cloud droplet size affects the time scale of evaporation and sedimentation of cloud droplets (Wood, 2012). This affects the entrainment rate at the cloud-top, which in its turn affects cloud droplet evaporation.

An overview of these cloud adjustments and feedback mechanisms resulting from a reduction in cloud droplet size and increase in N_d are shown in Figure 2.3 (Karset et al., 2020).

These indirect processes are currently not well understood and are some of the major challenges in understanding the impact of aerosols on the climate system. The response of the cloud's LWP to the aerosol seeding is a balance between the suppression of precipitation, which moistens the marine boundary layer and thickens the cloud, and the enhancement of cloud-thinning entrainment (Latham et al., 2008). Whether the net effect is cloud thickening or thinning depends on the time-specific conditions (Ackerman et al., 2004; Bretherton et al., 2007; Hill et al., 2009; Wang et al., 2011), which will be elucidated in Section 2.3 by using the budget equation for the LWP by Van der Dussen et al. (2014).

2.2.1. The Role of Precipitation

As stated earlier, when a large number of aerosols is available for cloud droplet activation through cloud seeding, the droplets will compete for the water vapour to grow. The result is a suppression of cloud droplet growth to the size and weight for which precipitation is initiated. It is crucial not to seed the cloud with giant aerosols (dry diameter larger than $\sim 1 \mu\text{m}$), which promote the Kelvin effect (the effect of larger aerosols requiring lower supersaturation than smaller ones) and droplet growth. Consequently, larger droplets increase the precipitation rate and reduce the cloud albedo (WANG11). The suppression of precipitation prolongs the longevity of the cloud and, thereby, its cooling effect. In both the simulation studies of WANG11 and Zhou et al. (2017), it was found that for shallow, drizzling, closed-cell structured stratocumuli the reduction of LWP dominates the decrease in cloud albedo, rather than the related change in cloud coverage or changes in r_e . For MCB, this indicates that it is more effective to retain cloud water (second indirect effect) than to reduce the effective radius of the cloud droplets (first indirect effect).

In addition, Ackerman et al. (2004) make a distinction in the effects of surface precipitation and cloud-top precipitation. In agreement with the findings of WANG11, they state that the LWP tends to increase due to decreased surface precipitation, while LWP is reduced by stronger entrainment due to decreased precipitation at the cloud-top. Ackerman et al. (2004) explain the latter finding by suggesting that precipitation dries out the cloudy air in updrafts, which reduces the water available for evaporative cooling in downdrafts. This reduces the turbulent mixing in the cloud layer and thereby decreases the entrainment rate. Inversely, the reduction of cloud droplet sizes by increasing N_{ae} reduces cloud-top precipitation, which then increases the entrainment rate.

A third consequence of precipitation is its effect on the stability of the atmospheric boundary layer by redistributing the latent heat (Curry and Webster, 1999). Drizzle settling from the top layer of the cloud removes water from that layer, which cannot be evaporated at that height subsequently. The effect of the drizzle is the net latent heating of the upper region of the cloud. In the layer below the cloud, the sub-cloud layer, the drizzle evaporates and hereby cools the sub-cloud layer. The effect is that the layer between the heated upper layer of the cloud and the cooled sub-cloud layer is stabilised. On the contrary, the upper layer of the cloud and the sub-cloud layer are destabilised. The negatively buoyant air parcels due to longwave cooling at the cloud top are not able to mix well through the sub-cloud layer, whereas the stable interface suppresses convection from the near-surface through this layer as well (Curry and Webster, 1999; Wood, 2012). In this case, the upper (cloud-containing) layer is decoupled from the surface moisture supply by the stabilised layer below. Due to sustained evaporation at the cloud-top, the cloud thins, LWP reduces, and the albedo decreases.

2.2.2. The Role of Entrainment

Contrary to the positive effect of precipitation suppression by aerosol injection on LWP and A_c , the effect of aerosol injection on cloud-top entrainment has a negative effect on LWP and A_c . In the transition zone between the cloud-top and free troposphere, called the entrainment interface layer, free-tropospheric air is cooled and moistened due to longwave radiation and evaporation of detrained cloudy air (Hoffmann and Feingold, 2019). When such a volume of negligible air is sufficiently cooled, it slowly sinks and mixes with the cloud layer until it homogenizes with the cloud.

The mixing of the entrained air is bounded by two types of mixing: homogeneous mixing, and extreme inhomogeneous mixing, each having its own effect on the cloud's microphysical composition as shown in Figure 2.4 (Hill et al., 2009; Hoffmann and Feingold, 2019; Karset et al.,

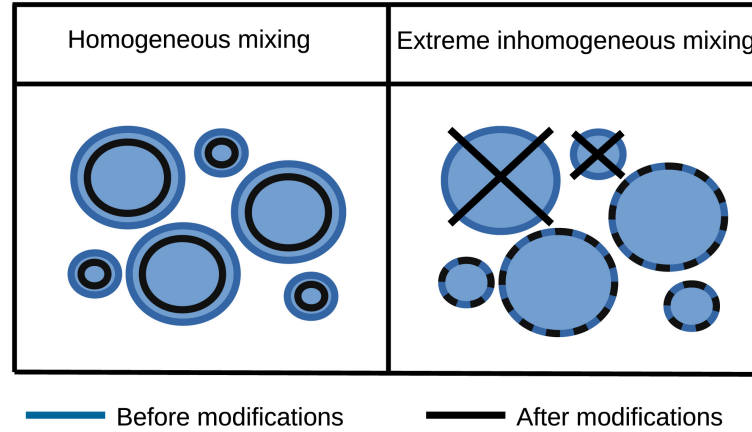


Figure 2.4: The two bounding mixing types of entrained free-tropospheric air within the cloud layer and their effect on cloud droplet number concentration and size (Kars et al., 2020). Homogeneous mixing (left) causes partial evaporation of all the cloud droplets, such that their size is reduced and the number of cloud droplets remains unchanged. Extreme inhomogeneous mixing (right) causes some cloud droplets to evaporate completely, while the other cloud droplets remain unaffected. This way, the number of cloud droplets is reduced, but their size is unchanged.

2020). Homogeneous mixing is caused by relatively faster turbulence, which generates a uniform subsaturation throughout the cloud layer. The result is partial evaporation of all cloud droplets, causing no change in N_d and a reduction in r_e . For extreme inhomogeneous mixing, the lack of effective turbulence causes the complete evaporation of cloud droplets locally. This results in no change in r_e , but a reduction in N_d . In the modelling study of Hoffmann and Feingold (2019) they found that inhomogeneous mixing causes the expected decrease in N_d . Moreover, the remaining droplets grew larger due to the reduced competition for the available water vapour. Although most observations of stratocumulus clouds show some degree of inhomogeneous mixing, standard LES and cloud-resolving models assume homogeneous mixing (Hill et al., 2009). It must be noted that this is also the case for the LES model (DALES) used in this thesis. The reduction in N_d and the increase in droplet size potentially enhance the precipitation rate and affect the evaporation- and sedimentation-entrainment effects. Therefore, it is expected that the incorporation of mixing types potentially has a significant impact on the simulation results.

Besides its effect on N_d and r_e , entrainment causes the stratocumulus-topped boundary layer (STBL) to deepen as well. While Wood (2007) suggested that the entrainment rate w_e increases with increasing cloud-base height $z_{c,base}$, the more recent study of Zheng et al. (2018) show that this relation holds the other way around as well. Cloud-top radiative cooling in a well-mixed marine STBL causes an increase in turbulence and hence in w_e , which elevates $z_{c,base}$. This indicates a positive feedback loop between w_e and $z_{c,base}$.

When the top of the STBL deepens beyond 1 km, it becomes difficult for the positively buoyant entrained air to be well-mixed throughout the entire STBL due to longwave cooling at the cloud-top (Wood, 2012; Zheng et al., 2018). This results in the separation of the cloud-containing layer from the moisture supply by a (weakly) stable layer in between. As stated earlier, the decoupling from the surface moisture supply leads to cloud thinning and eventually break-up. In addition, the entrainment of warmer and drier air raises the condensation level in the cloud layer, causing cloud thinning from below as well (Eastman and Wood, 2018).

The strength of entrainment depends on the conditions and feedback mechanisms within and outside the cloud layer, which will be explained below.

Evaporation-entrainment effect

Figure 2.3 shows the positive feedback between evaporation and entrainment, called the evaporation-entrainment effect. This cloud-modifying process is described as follows (Hill et al., 2009; Hoffmann and Feingold, 2019; Karset et al., 2020): at the cloud-top, entrained air causes some of the water droplets to evaporate, causing latent cooling of the cloud-top. This induces increased turbulence in the top layer of the cloud, which increases the level of entrainment. Upon increasing N_d and decreasing r_e by cloud seeding, the total droplet surface area is increased, which accelerates evaporation and thereby turbulent mixing and entrainment. To provide an estimation of the order of magnitude of its effect: in the study of Hill et al. (2009), this leads to greater entrainment warming of the boundary layer and reduction in LWP of about 7%, which is consistent with earlier studies.

Sedimentation-entrainment effect

The next part of the cloud adjustments depicted by Figure 2.3 is the effect of cloud droplet sedimentation on entrainment, and thereby on LWP. This effect has been examined in the LES study of Bretherton et al. (2007), who simulated the effects of sedimentation on a shallow non-drizzling nocturnal stratocumulus-topped well-mixed boundary layer (the first research flight (RF01) of the DYCOMS-II field experiment, also used for dry environment simulations in WANG11 and in this thesis). Contrary to the argument of Ackerman et al. (2004) on reduced turbulent mixing due to cloud-top precipitation, Bretherton et al. (2007) found that the decreased turbulence in the cloud layer due to cloud droplet sedimentation is minimal. In their study, the vertical motion approximately 50 m below the cloud-top remains unchanged when comparing the simulations with no, low and high levels of sedimentation. Furthermore, they found a reduction in the entrainment rate w_e and a significant increase in LWP for increasing sedimentation rates: -3% in w_e and +10% in LWP for low sedimentation, and -7% in w_e and +21% in LWP for high sedimentation. Bretherton et al. (2007) argue that cloud droplet sedimentation reduces the liquid water available for evaporation at the entrainment-zone at the cloud-top, which reduces the entrainment rate. They also attribute this process to the cloud-top precipitation related findings of Ackerman et al. (2004).

Coupling of evaporation-entrainment effect and sedimentation-entrainment effect

In addition, Bretherton et al. (2007) suggested that the reduction in entrainment rate was for about 90% due to the evaporation feedback. In other words, sedimentation initially causes a relatively small reduction in evaporation, but this reduction strongly diminishes further entrainment caused by the evaporation-entrainment effect. This coupling between the evaporation-entrainment and the sedimentation-entrainment effect is seen in the entrainment study of Hill et al. (2009) as well. However, they made a discrepancy between clean and polluted STBLs. Here, the LWP of the clean STBL ($N_{ae} = 100 \text{ cm}^{-1}$) reduces by approximately 21% due to the evaporation-entrainment effect only, but when including sedimentation to the entrainment scheme, the reduction is diminished to about 14%. This shows that in the clean STBL, stratocumulus clouds lose less water through entrainment due to the positive contribution of the sedimentation-entrainment effect to the LWP. However, when looking at the polluted STBL ($N_{ae} = 1000 \text{ cm}^{-1}$), the cloud's LWP seems to be unaffected by the introduction of the sedimentation-entrainment effect. Thus, increasing N_{ae} by aerosol injection reduces the cloud droplet sedimentation rate by reducing its size and falling velocity, which consequently has a negative effect on the cloud's LWP.

Effect of free-tropospheric conditions

Another factor that plays a role in the effect of cloud-top entrainment is the relative difference in atmospheric boundary conditions and the conditions within the free-troposphere.

Ackerman et al. (2004) found that when modifying the above-cloud relative humidity, the balance between the effects of changing N_d on LWP is affected. For relatively high values of free-tropospheric relative humidity $RH_{ft} \sim 70\%$, the LWP increases with N_d , but for a dry free-troposphere ($RH_{ft} \sim 10\%$) the entrainment effect dominates and LWP reduces with N_d . Intermediate values of RH_{ft} result in an increase in LWP for low-to-moderate N_d ($\sim 100 \text{ cm}^{-3}$), but a decrease for higher values of N_d . The positive effect of RH_{ft} on LWP is also analytically expressed by Wood (2007) where RH_{ft} contributes positively to thickening of the stratocumulus clouds.

This effect is explained by Eastman and Wood (2018), who state that increased humidity of the free-troposphere affects entrainment through two different mechanisms. A greater free-tropospheric humidity causes cloud droplets to evaporate less before the cloud-top reaches saturation, generating less cooling and entrainment. Secondly, it produces more downwelling longwave radiation. This reduces the energy loss of upwelling radiation, causing a reduction in cooling and entrainment. In addition, Wood (2012) states that entrained free-tropospheric air raises the cloud-base level as it decreases the relative humidity in the cloud-layer and consequently increases the level at which condensation takes place. Hence, a drier free-troposphere favours the increase in cloud-base height.

Another free-tropospheric condition that might be required to be taken into consideration is the free-tropospheric N_{ae} . In previous research on MCB using LES, which will be discussed in Section 2.3, an initially uniform N_{ae} is assumed for the background concentration. However, as shown by Dadashazar et al. (2018) who studied the vertical profiles of N_{ae} in the same region as the meteorological cases considered in this study, N_{ae} in the free troposphere can significantly deviate from that in the STBL. This difference in N_{ae} results in an additional source or sink of aerosols in the STBL through entrainment, which we call the entrainment aerosol transport, affecting the cloud's radiative properties. Additional theoretical background to this matter will be given in Chapter 6, in which the effects of vertically non-uniform N_{ae} on the radiation-affecting cloud properties will be investigated.

2.3. Previous LES Research on MCB

As MCB has gained interest in the scientific community over the recent years, multiple studies have been carried out on the subject. However, most of these studies are based on simulations of global climate models, which focus on the global climate response to aerosol number concentration enhancement over multiple decades (e.g., Alterskjær and Kristjánsson, 2013; Bala et al., 2011; Kim et al., 2020; Stjern et al., 2018; Zhu et al., 2021). Due to the required coarse resolution of these models, the representation of cloud processes, the feedback mechanisms and the role of aerosols as described earlier remains difficult to model (Bader et al., 2008). Although studies involving global climate models provide valuable insights into large-scale effects of MCB, such as its effect on the hydrological cycle (Bala et al., 2011) and the regional differences of the effects (Kim et al., 2020; Zhu et al., 2021), they give no direct insight into the evolution of a seeded cloud region. Therefore, the comparison of these types of studies with the study presented in this thesis is impractical. The focus will be on previous (higher resolution) studies in which the changes in cloud properties due to deliberate cloud seeding with the goal of MCB is investigated.

Currently, only three studies have explicitly modelled the surface aerosol injection strategy as

suggested by Salter et al. (2008) with the intended goal of MCB. These studies all investigate the efficacy of MCB with a different approach: WANG11 research the effect of MCB in a shallow STBL using different spray-source strategies, Jenkins et al. (2013) examine the effect of a point source aerosol spray in a shallow STBL when initiating the aerosol seeding at different times during the diurnal cycle and Possner et al. (2018) research the effect of a point source aerosol spray in a deeper STBL. The main conclusions derived from these studies are given below.

WANG11, on which the research of this thesis builds upon, examined the impact of the added aerosols on the microphysical processes and feedback mechanisms in a shallow marine boundary layer (from DYCOMS-II, see Section 3.3), using 30-hour simulations with the Advanced Research WRF cloud-resolving model in the LES mode. They simulated the time-varying effects of a surface-based single, triple and uniform aerosol source moving through the scene on the cloud's albedo, cloud fraction, LWP, rain rate, cloud top height and N_d . This was then done for a relatively clean maritime environment (low initial aerosol background concentration), average maritime environment and a polluted maritime environment. A wet and precipitating boundary layer and a non-precipitating, drier and warmer boundary layer were simulated for each environment. Their results show that the most efficient way to enhance the cloud albedo is to sustain cloud water by suppressing precipitation. To do so optimally, areal coverage and concentration of the aerosols should be balanced, which depends on the meteorological conditions and background aerosol concentration. Maximum areal coverage has shown to be most effective in weakly precipitating boundary layers. High concentrations (from a point source) is most effective in boundary layers with a limited number of aerosols, which occur after heavy depletion of aerosols due to heavy or persistent rainfall. MCB is less to ineffective in three regimes: in strongly precipitating regimes (aerosol replenishment is insufficient to cover the depletion caused by precipitation), in polluted, non-precipitating regimes (the cloud already have a high albedo, albedo enhancement is negligible due to LWP reductions caused by N_d increases) and in dry regimes (a very small fraction of the cloud condensation nuclei will be activated due to the limited available water vapour and albedo enhancement caused by increases in N_d is countered by LWP reduction due to cloud-top evaporation). In this study, the direct radiative effect of the added aerosols is not accounted for. Especially in the plumes of the aerosol sources, where concentrations are extremely high, they expect that this effect can be significant. In addition, the sensitivity to aerosol composition and size is not considered as well.

Jenkins et al. (2013) studied the albedo response to point source aerosol seeding initiated a different times during the diurnal cycle and investigated the direct aerosol effect from the concentrated injection by the point source. For this study, the same meteorological case was used as by WANG11. The ideal time of seeding to enhance the all-sky albedo (the average albedo of the entire domain) for a weakly precipitating regime is the early morning (03:00 h local time). This is due to sustaining the LWP and suppressing precipitation, consistent with the results of WANG11. The high concentrations of aerosols cause aerosols that are too small to be activated to accumulate above the cloud. The reflective effect of these aerosols appears to mask the enhancement in the cloud albedo, which suggests that the direct aerosol effect could have a significant impact when performing MCB with highly concentrated aerosol sources.

In the study of Possner et al. (2018) the aerosol-cloud radiative effects in a deep STBL (1500 m) with open-cell precipitating stratocumuli are investigated using simulations with the same model used by WANG11. The simulated maritime environment was much cleaner compared to the clean environment of WANG11 ($\sim 30 \text{ cm}^{-3}$ vs 50 cm^{-3}) Similar to the point source strategy in WANG11, they implemented a moving point source spraying aerosols into the boundary layer with an equal spraying rate and source velocity. Although their results do not show a

distinct albedo enhancement in the form of ship tracks (see Figure 1.1), but the domain-mean all-sky albedo showed an enhancement similar to the one found by WANG11 for a shallow STBL. The obtained cloud brightening belonged to the albedo enhancement of optically thin detrained cloud sheets (so-called veil clouds) encircled by the convective cell walls of the open cells. The vertical transport of aerosols is mostly done within these cell walls, because of the strong vertical stratification of the sub-cloud layer. The brightening is predominantly caused by increases in cloud fraction, and the contribution of the modification of cloud microphysical properties (e.g. N_d and LWP) was of secondary importance.

Altogether, the conclusions drawn in these three studies are somewhat preliminary, as they all investigate different aspects of MCB, and no other comparable studies using the same approaches have been carried out. As in the studies of both WANG11 and Jenkins et al. (2013) the LWP turned out to be the most significant factor for MCB, it is of interest to determine what processes drive the changes in LWP due to aerosol seeding. However, as stated in Section 1.2, the cloud-resolving models of WANG11 and Jenkins et al. (2013) are unable to simulate small scale mixing processes such as cloud-top entrainment accurately, which is critical in studying the effects of aerosol injections on the LWP. By performing an inter-comparison with the study of WANG11, we aim to add to the robustness of their conclusions, while adding to the knowledge of the processes affecting the LWP.

3

Methodology

In this chapter, we describe our methodology. First, the simulation model chosen for this thesis will be introduced and motivated, after which the adjustments to the standard version required for the presented research are stated. The meteorological cases serving as the simulation input will be described next, including the vertical profiles of the meteorological parameters. Finally, the general setup of the simulations will be given, which apply to all ran simulations. For the purpose of clarity, the specific setups per simulation purpose (validation, MCB and entrainment aerosol transport) are provided in Chapters 4, 5 and 6, respectively.

3.1. Dutch Atmospheric Large-Eddy Simulation

Within the atmospheric boundary layer, the scale of the turbulent motions, named eddies, vary significantly. While the largest eddies have a length scale in the order of the atmospheric boundary layer itself, the smallest eddies responsible for the viscous dissipation of energy have a length scale in the order of millimetres. In fluid dynamics, the central equations to be numerically solved are the Navier-Stokes equations, which ideally is done for all length scales to obtain high accuracy. This can be done with the use of direct numerical simulations (DNS). However, these models have the disadvantage of requiring a very small mesh size to include the smallest turbulent flows in their calculations. The result is that to apply such a method to atmospheric research, like presented in this report, the number of grid points would be too large to be practically feasible in terms of computational costs.

Consequently, the smallest eddies have to be parameterised. On the other side of the spectrum with respect to DNS are the general circulation models (GCMs). GCMs are often used for global climate studies, which require a very coarse mesh size in the order of tens to hundreds of kilometres. Consequently, nearly all eddies require to be parameterised in these models and are therefore impractical for the study presented in this report.

A solution for this problem is given by the method of large-eddy simulations (LES), in which the turbulent scales larger than a specific filter size are resolved, and smaller eddies are parameterised (Heus et al., 2010). As such, the Navier-Stokes equations are explicitly solved for the larger-scale eddies that dominate the turbulent energy budget of the system, whereas smaller-scale eddies are parameterised in subgrid models. The filter size is a function of the grid size of the simulation, and therefore, the grid size determines the cut-off length scale below which eddy flow is parameterised. This method is shown in Figure 3.1, which schematically represents various eddy sizes with respect to a grid size $\bar{\Delta}$ (left) and the corresponding cut-off

wave number in Fourier space (right) below which eddies are resolved and above which they require parameterisation (Sagaut, 2006). Note that in this example, the filtering size is taken equal to the grid size.

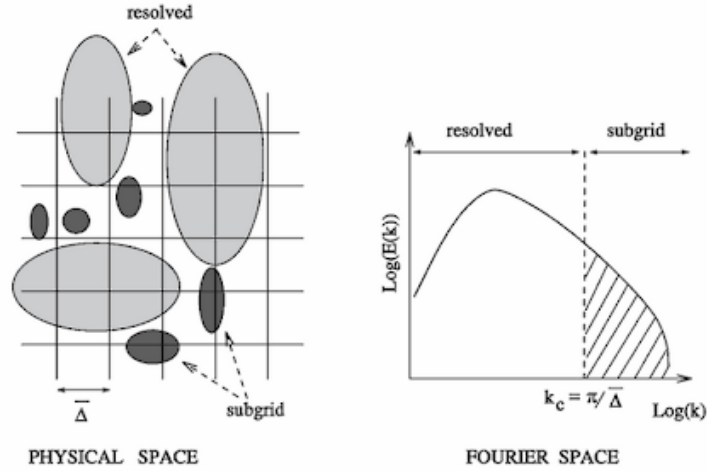


Figure 3.1: Schematic representation of eddy filtering by Large-Eddy Simulation models (Sagaut, 2006). On the left various eddy length scales are shown on a grid with grid size $\bar{\Delta}$ in physical space. The right-hand-side shows the eddies' kinetic energy as a function of its length scale in Fourier space. In this schematic view, eddies with a smaller length scale than $\bar{\Delta}$ (or smaller wavenumber than $\frac{\pi}{\bar{\Delta}}$) are not resolved in the LES model.

In this thesis, we use the Dutch Atmospheric Large-Eddy Simulation (DALES) model (Heus et al., 2010). Together with researchers from the Royal Netherlands Meteorological Institute (KNMI), Wageningen University and the Max Planck Institute for Meteorology, researchers from Delft University of Technology have developed and currently maintain DALES. It has joined a wide variety of inter-comparison studies such as the GEWEX Atmospheric Boundary Layers Study (GABLS), which looks at the clear boundary layer, and the GEWEX Cloud System Study (GCCS) Boundary Layer Cloud Working Group, which mainly focuses on shallow cumulus and stratocumulus clouds. The meteorological cases used in this thesis (DYCOMS-II, see Section 3.3) were part of the GCCS as part of the studies by Stevens et al. (2005) and Ackerman et al. (2009) (ACK09 from this point onward). Next to the studies on convective, stable and cloud-topped boundary layers, DALES has been used on a broad spectrum of other applications related to flows in the atmospheric boundary layer and has been extensively used and compared to observations by the KNMI. Altogether, this makes DALES a very well-tested LES model and a proper tool for our simulations.

We use the most recent version of DALES, namely DALES 4.3, which is written in the programming language Fortran 90. In Section A, the governing equations of DALES will be briefly discussed, and information on the boundary conditions and forcings that are relevant for our simulations will be provided in Section 3.4. Additional information on DALES and its applications can be found in the paper of Heus et al. (2010).

3.2. Model Extensions

3.2.1. Implementation of cloud droplet number concentration parameterisation

The main subject in this thesis is the effect of aerosol number concentration enhancement on cloud dynamics and cloud properties. Therefore, the activation of these cloud condensation nuclei plays a central role. In the standard, unmodified DALES model, the role of aerosols is not included in the parameterisation of the cloud droplet number concentration N_d . Instead, N_d is set to a constant value, which is ideally based on measurements, for every grid point

where the local liquid water mixing ratio q_l is larger than the cloud specific mixing ratio threshold $q_{c,min} = 10^{-7} \text{ kg kg}^{-1}$ and is thus independent on local aerosol number concentrations. Consequently, N_d is vertically uniform within the cloud-layer, which is approximately validated for stratocumulus clouds by both aircraft observations and LES simulations (Grosvenor et al., 2018).

However, following the Köhler theory, an ideal simulation model includes a microphysical scheme that determines the cloud droplet number concentration based on aerosol number concentration N_{ae} , the local supersaturation of the ambient air and the critical supersaturation of the aerosol (Hede, 2013). This additionally requires the definition of the aerosol's chemical composition, the mass distribution and size distribution for every type of aerosol present in the simulated atmospheric boundary layer. Moreover, this scheme has to explicitly model droplet growth (by condensation and autoconversion), aerosol number concentration reduction (due to processes such as precipitation, coalescence scavenging and coagulation) and concentration enhancements by natural aerosol sources (such as surface emissions, local nucleation and transport from the free-troposphere). In reality, such a model cannot be realised due to the limited current understanding of aerosol properties and the fact that this would require too much computer power to be practically feasible (Wang et al., 2021). Hence, aerosol activation to cloud droplet concentration needs to be parameterised.

In order to make the N_d parameterisation in DALES aerosol-dependent, we extended the standard DALES version with a new scheme that makes use of the regressive fit by Twohy et al. (2005) (see 2.1), that is based on the meteorological conditions used in this thesis¹. The advantage of utilising the regressive fit of Twohy et al. (2005) for parameterising aerosol activation is that the various chemical compositions do not need to be specified, as well as the aerosol size and mass distributions, because they are all included in the fitted parameterisation. This means that for a certain N_{ae} , the parameterisation assumes to consist of the chemical compositions, sizes and masses corresponding to the measured values. The downside of this method is that when increasing N_{ae} by aerosol seeding, the injected aerosols are assumed to consist of the same aerosol conditions as the background value. Hence, it is not possible to simulate a surface aerosol source of a prescribed chemical composition and size and mass distribution when using this parameterisation, which could enhance the number of activated aerosols (Salter et al., 2008).

The roll-off of the curve at the higher aerosol number concentrations in Figure 2.2 indicates the suppression of supersaturation, and a smaller fraction of the number of aerosols are activated (Twohy et al., 2005). This roll-off is consistent with the other data sets presented in the study of Twohy et al. (2005) and satellite observations. This way, the effect of N_{ae} activation on the supersaturation and vice versa is indirectly incorporated in the parameterisation scheme.

N_{ae} is represented in DALES by a scalar, whose initial vertical profile is prescribed in the input profiles. DALES requires the scalar units to be with respect to the mass of air (kg^{-1}) instead of volume (cm^{-3}) in order to apply the advection schemes rightfully. Consequently, this alters the parameterisation equation (Eq. (2.8)). In addition, two conditions² are added to Eq.

¹Please note that the parameterisation used here is specifically based on the measurements made during DYCOMS-II and is not suited to be used when simulating other meteorological cases than obtained in the research flights of this field experiment. The relationship between N_{ae} and N_d strongly depends on the cloud type and geographical location (through the influence of continental air masses), affecting the aerosols' chemical composition and size and mass distributions. However, the N_{ae} activation parameterisation specified for DYCOMS-II can be adjusted to be used for other meteorological cases by replacing the equation resulting from the regressive fit by a new fitting curve (such as those presented in Twohy et al. (2005) for various maritime environments or in Gultepe and Isaac (1996) for both continental and maritime environments).

²These conditions are included for the sake of completeness. With the applied background concentrations and

(2.8) to prevent two unphysical phenomena to occur: for values of $N_{ae} < 2.15 \text{ cm}^{-3}$, N_d is set to an arbitrary small value³ (here 10^{-10} cm^{-3}) to prevent negative cloud droplet number concentrations, which could occur from numerical artefacts of the advection scheme. For $N_{ae} > 613.50 \text{ cm}^{-3}$, corresponding to the top of Eq. (2.8), N_d is set to a constant value of 312.83 cm^{-3} to prevent a negative relation between N_d and N_{ae} . The final equation that is implemented into DALES is therefore:

$$N_d = \begin{cases} 10^{-10} \text{ cm}^{-3}, & \text{if } \rho_{air}(z)N_{ae,kg} < 2.15 \text{ cm}^{-3} \\ -2.2 + 1.027\rho_{air}(z)N_{ae,kg} - 0.000837 [\rho_{air}(z)N_{ae,kg}]^2, & \text{if } 2.15 \text{ cm}^{-3} < \rho_{air}(z)N_{ae,kg} < 613.50 \text{ cm}^{-3} \\ 312.83 \text{ cm}^{-3}, & \text{otherwise} \end{cases} \quad (3.1)$$

where $N_{ae,kg}$ is the aerosol number concentration in kg^{-1} and $\rho_{air}(z)$ is in kg cm^{-3} . For the scalar $N_{ae,kg}$, a surface flux can be prescribed to mimic the aerosol injection. Other natural aerosol sources or sinks, such as those stated earlier, are currently not incorporated in the DALES model and remain for future work. Notably, this outstanding point of improvement exists for the standard DALES model as well, as a balance between aerosol sinks and sources is also implicitly assumed by assuming a constant N_d .

The observant reader might notice that for a well-mixed boundary layer, for which a vertically uniform $N_{ae,kg}$ is assumed, N_d is no longer vertically uniform due to the decreasing $\rho_{air}(z)$ with height. However, when taking $N_{ae,kg} = 100 \text{ mg}^{-1}$ the maximum difference in N_d for a cloud with a cloud-top at 800m and a cloud-base at 400m would be approximately 3.5%. This difference is in a good approximation of the observations and compared to the approximation of the vertically uniform N_d in the presented cases by Grosvenor et al. (2018), this difference is sufficiently small to be said to be approximately uniform as well.

By using a scalar representation for $N_{ae,kg}$, the direct aerosol effect, which accounts for the reflection of solar radiation of the aerosols themselves, is not taken into consideration. Although this is also not accounted for in the standard DALES model, studies of both Jenkins et al. (2013) and Ahlm et al. (2017) show that the direct aerosol effect might have significant implications on the radiative forcing from MCB. Whether it causes a cooling or warming effect is currently unclear, as these two studies show opposite results for the net radiative forcing.

3.2.2. Point Source Surface Flux

In the standard DALES model, the aerosol surface fluxes that can be prescribed apply to all grid points of the bottom of the domain and are thus homogeneously applied. We apply a point source for the aerosol number concentration as well to mimic the spraying emissions from a single Flettner rotor ship as described in Salter et al. (2008). This is done by prescribing the surface flux only at the location of the point source instead of prescribing the surface flux to all grid points. For horizontal periodic boundary conditions, the source can be chosen at any arbitrary location, because aerosols that are advected out of the domain at one edge are advected back into the domain on the opposite side. For our simulations, the point source is located in the upwind corner of the domain. As a result of the horizontal periodic boundary conditions, the simulated domain can be regarded as part of a larger system undergoing MCB with evenly-spaced aerosol point sources, spaced at exactly the horizontal domain dimensions. This is illustrated in Figure 3.2, which schematically shows the horizontal paths of the

surface aerosol sources in our simulations, the values for N_{ae} will be well between the range of 2.15 cm^{-3} and 613.50 cm^{-3} . Therefore, the added conditions will not affect N_d .

³An arbitrary small value for N_d is chosen for the lower limit of the parameterisation instead of 0 cm^{-3} to prevent model instabilities, which may occur if another DALES equation divides by N_d .

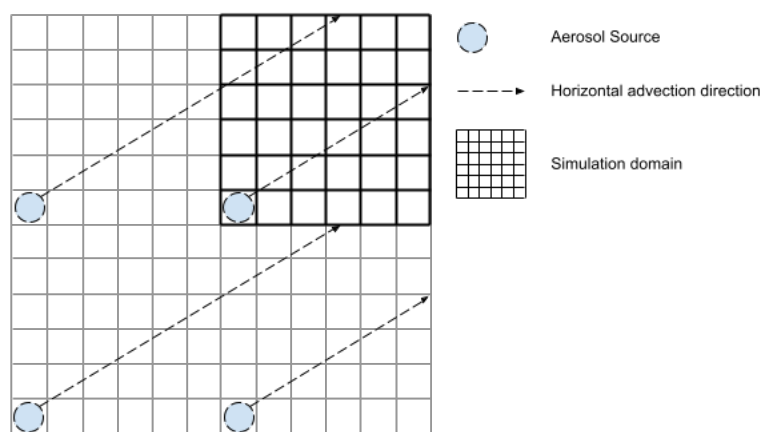


Figure 3.2: Schematic top-view representation of regarding a single point source in the simulated domain with horizontal periodic boundary conditions as a sub-domain of a larger system of evenly-spaced point sources.

injected aerosols inside the simulated domain and of two virtually neighbouring domains. As can be noted, at the opposite location of where the paths exit the domain edges, the virtual aerosol paths enter the simulated domain.

3.3. Case Description: DYCOMS-II

The meteorological environments for our simulations are retrieved from the second Dynamics and Chemistry of Marine Stratocumulus (DYCOMS-II) field study performed in July 2001. The focus of DYCOMS-II was to perform measurements that help to examine the entrainment rate and drizzle amount in stratocumulus decks (Stevens et al., 2003). During nine nocturnal flights over the northeastern Pacific in the general region of $122^{\circ}W$ $31^{\circ}N$, both remote sensing and in situ data were obtained. The forcings of nocturnal stratocumuli tend to be more stationary than daytime stratocumuli due to the absence of incoming solar radiation. This reduces the temporal variations of the energetics and simplifies the analysis and characterisation of the cloud. With this data, the mean state of the boundary layer of the target area was determined, which forms the initial state of the boundary layer for the performed simulations.

The research flights of interest are the first and second research flights (RF01 and RF02, respectively). The choice of these two flights is because the environments obtained from these flights were used in the MCB study of WANG11, which is used for the inter-comparison of the results. Conveniently, RF02 also has been used in the LES inter-comparison study of ACK09, in which DALES took part as well. Therefore, this study will be used for qualitative validation of the performance of DALES with respect to that of earlier LES models in the eye of generating comparable results to the measured quantities. RF01 is used for simulating a drier and warmer meteorological state compared to RF02. Simulating different meteorological states is important in assessing the global effectiveness of MCB, as MCB requires to be deployed on a large scale, and thus on a variety of meteorological states, to be globally effective.

For both flights, the measurements were obtained between around 06:00:00 and 16:00:00 UTC, and they are both characterised by a relatively well-mixed boundary layer (Stevens et al., 2005). Relative to RF02, RF01 had a slightly more persisting cloud layer of over 99 % throughout the night, compared to 97% for RF02. The relevant parameters that serve as input for the simulations will be provided in the subsections below, starting with the shared parameters, followed by the differences in the input parameters used for the simulations of RF02 and RF01. A more detailed explanation of the research flights concerning flight paths,

measurement instrumentation, and more can be found in the studies of Stevens et al. (2003) and ACK09.

3.3.1. Shared Parameters

In this research, the basis of the meteorological state will be that of RF02, and all parameters will be set to this state accordingly, except that of the vertical profiles of θ_l and q_t . This enables the ability to better demarcate the effect of changes in these parameters and disregard the effect of other parameters such as wind velocity, solar zenith angle, and others.

The latitude of the simulated domain is set to 31.5°W and the longitude to 240.5°E . The measurements were taken on day 195 of the year 2001. As stated in Section 5.1.1, both the domain location and the time of year affect the solar zenith angle and consequently the radiation received at the top of the domain. The time of sunrise is 05:00 h local time, and the sun sets at 19:00 h.

For both RF01 and RF02, the large-scale vertical wind is given by $w_{ls} = -Dz$, with D the uniform large-scale divergence rate of $D = 3.75 \cdot 10^{-6} \text{ s}^{-1}$. The horizontally-averaged measured profiles of the westerly wind u and southerly wind v of RF02 are found to be $u = 3 + \frac{4.3z}{1000} \text{ m s}^{-1}$ and $v = -9 + \frac{5.6z}{1000} \text{ m s}^{-1}$, which serve as the initial profiles of the geostrophic winds.

The initial sea surface temperatures (SST) are not identical, but are calculated from the lowest θ_l value of the vertical profile (see Subsections 3.3.2 and 3.3.3). The turbulent surface fluxes of θ_l and q_t are set to respectively 0.0131 mK s^{-1} and $0.0305 \text{ g kg}^{-1} \text{ s}^{-1}$, which are equal to the values used in the inter-comparison study of ACK09.

The other parameters, such as domain size, aerosol input profiles, and aerosol surface fluxes, vary between the simulations according to their purpose and will be stated explicitly per purpose in Sections 4.1, 6.2 and 5.2.

3.3.2. Research Flight 02

The input parameters that differ between the simulations representing the initial states of RF01 and RF02 are the initial vertical profiles of θ_l and q_t . The mean state of RF02 has been determined by averaging all measurements and idealizing the profiles in a two-layered structure in θ_l and q_t , demarcated by the inversion height z_i (ACK09). The vertical profile of θ_l is given by:

$$\theta_l = \begin{cases} 288.3 \text{ K}, & \text{if } z < z_i \\ 295(z - z_i)^{1/3} \text{ K}, & \text{otherwise,} \end{cases} \quad (3.2)$$

where θ_l was derived from the measured air temperature and the initial inversion height z_i which for RF02 is 795 m. The initial SST equates to about 289.8 K. The total water mixing ratio for RF02 is given by:

$$q_t = \begin{cases} 9.45 \text{ g kg}^{-1}, & \text{if } z < z_i \\ 5 - 3(1 - e^{(z-z_i)/500}) \text{ g kg}^{-1}, & \text{otherwise} \end{cases} \quad (3.3)$$

3.3.3. Research Flight 01

Similar to RF02, the meteorological state of the second research flight has been idealised to a two-layered structure as well (Stevens et al., 2005), which are given in Eqs. (3.4) and (3.4). Compared to RF02 the free-tropospheric air above the inversion layer of RF01 is warmer and drier (see Figure 3.3). For a 50 m inversion layer, RF01 has inversion jumps for θ_l and q_t

of about $\Delta\theta_l = 12.05$ K and $\Delta q_t = 7.5$ g kg⁻¹, whereas for RF02 these are approximately $\Delta\theta_l = 10.12$ K and $\Delta q_t = 4.68$ g kg⁻¹.

$$\theta_l = \begin{cases} 289.0 \text{ K}, & \text{if } z < z_i \\ 297.5 + (z - z_i)^{1/3} \text{ K}, & \text{otherwise} \end{cases} \quad (3.4)$$

Originally for RF01 z_i is initially at 840 m. However, in order to exclude the effect of the difference in initial inversion height, this is set to the height of RF02 where $z_i = 795$ m. With a θ_l of 289.0 K below at the domain's surface, initial SST for RF01 is approximately 290.5 K. The profile of the total water mixing ratio q_t is given by:

$$q_t = \begin{cases} 9.0 \text{ g kg}^{-1}, & \text{if } z < z_i \\ 1.5 \text{ g kg}^{-1}, & \text{otherwise} \end{cases} \quad (3.5)$$

The differences in the vertical profiles between RF02 and RF01 are shown in Figure 3.3 below:

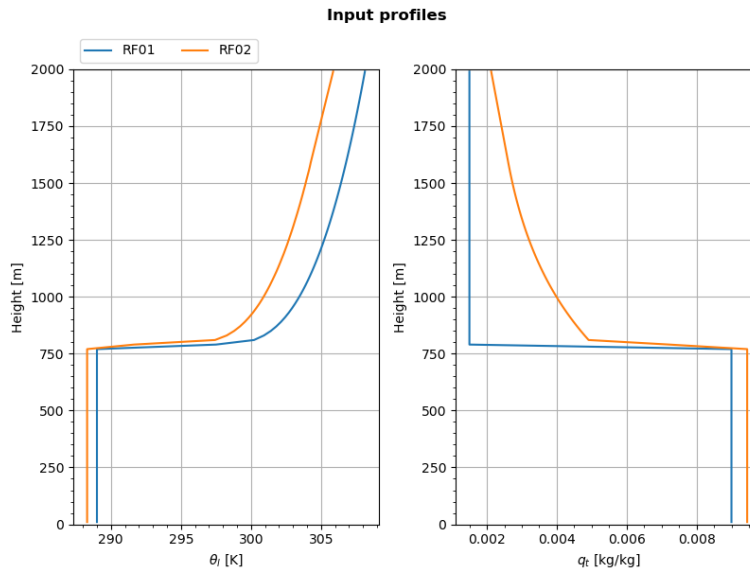


Figure 3.3: Idealised initial mean states of θ_l (left) and q_t (right) from Research Flight 01 and 02 (Ackerman et al., 2009; Stevens et al., 2005). Each profile is described by a two-layered structure and is used to initialize the performed simulations.

3.4. General Settings

To properly assess the effects of the cloud seeding and the differences in θ_l and q_t , it is essential to preserve the model settings among the simulations as much as possible. Utilizing different radiation or advection schemes may result in significantly altered outcomes, obscuring the conclusions that can be drawn. Therefore, the same radiation and advection setups are used among the simulations.

We make use of the most detailed radiation transfer model available in DALES, which is based on the Fu-Liou radiation scheme (Heus et al., 2010). This scheme includes multiple wavebands in its calculations as well as the vertical profiles of temperature, ozone and humidity up to the top of the atmosphere. The radiative forcings are updated every 60 seconds in simulated time instead of every time step to reduce computation costs. Variations of cloud properties are relatively small for this time interval. Hence, the effect of this lower calculation frequency is assumed to be negligible. It should be noted that the position of the cloud changes within the time interval. Consequently, the radiative forcings do not act on the actual

position of the cloud, but lag maximally 60 seconds in time. Further decreasing the radiation calculation frequency reduces this effect, but increases the computational costs of the simulation. Additionally, the Monte Carlo Spectral Integration is used to further reduce computation costs Pincus and Stevens (2009). In this approach, one waveband instead of ten is randomly selected for every column of the domain to calculate the radiative effects for each column. For an individual column, this induces significant error relative to when all wavebands are taken into account. However, this error reduces with $1/\sqrt{n}$ (with n the number of columns). When taking a sufficient number of columns, the resulting radiative effects are statistically nearly invariant with respect to that of the calculations using all wavebands.

As introduced earlier, this research implements a strong surface aerosol source with respect to the background conditions. This generates a strong gradient in aerosol number concentration at the bottom of the domain. Due to the dispersive nature of often-used higher-order advection schemes, this causes the system to generate non-physical negative aerosol number concentrations and subsequently affects the microphysics of the simulation. Therefore, the applied advection scheme in this research requires to be either positive definite (generating no negative values) or monotonic (producing no new minima or maxima). The disadvantage of these schemes is that they are relatively more dissipative with respect to higher-order advection schemes. Positive definite schemes have the undesirable characteristic of enhancing local maxima, which strongly affects cloud-aerosol interactions (Wang et al., 2009). Monotonic schemes that influence cloud-aerosol interactions have shown to minimize dispersion errors and preserve strong gradients sufficiently. The available (strictly) monotonic advection scheme in DALES is the Kappa advection scheme, which is based on the method of Hundsdorfer et al. (1993). It makes use of a limiter function, which serves as a switch between higher-order advection and first-order upwind in case of strong upwind gradients of the calculated scalar tendency. To validate that this advection scheme can be properly used for our simulations, the order of magnitude of the produced tendencies is mathematically determined in Section B of the Appendix.

Next to the Kappa advection scheme that is used to calculate the advection of $N_{ae,kg}$, the scheme that is applied for the advection of momentum, turbulent kinetic energy, potential liquid water temperature and the total water mixing ratio is the 52 advection scheme. This scheme does the advection with the fifth-order upwind scheme in the horizontal direction and the second-order upwind scheme in the vertical. The 52 advection scheme is often used, as it is more accurate with respect to lower-order schemes. Applying the second-order scheme in the horizontal direction instead of the fifth-order would significantly reduce its accuracy. Replacing the vertically used second-order scheme with the fifth-order scheme would further increase the accuracy of the calculated advection, but has the downside of coming with increased computational costs.

Finally, horizontal boundary conditions are not required to be specified, because DALES makes use of periodic horizontal boundary conditions. As stated earlier for the aerosols in Subsection 3.2.2, this means that quantities that are advected outside of the domain at one edge are advected back into the domain on the opposite side.

4

Validation

This chapter presents and discusses the effects of the adjustments made to the DALES model to enable the representation of aerosol concentrations. Before any justifiable conclusions can be drawn from the simulations that use the modified DALES model, the performance of this new model needs to be validated. The goal is to qualitatively validate that the new model can simulate the RF02 case in agreement with the standard DALES model. Secondly, the results generated by this new model need to be compared to the observations and the results of the earlier inter-comparison study by ACK09. This is important, as differences in how physical processes are modelled among the models may influence the modelled effects of MCB for similar meteorological cases.

In this chapter, the setup of the validation simulations will be provided first. Secondly, the validation will be done with respect to the results of the standard DALES model. Next, the results are compared to the results of the model inter-comparison study of ACK09, which incorporates both the results of various models and the data of the observations. This is done to give insight into how the generated physical quantities by DALES with respect to those generated by other LES models may influence the results presented in the remaining part of the thesis. The presented parameters are chosen in correspondence with those presented in the work of ACK09 to be able to compare results.

4.1. Simulation Setup

The standard (unmodified) DALES model will be used to simulate RF02 conform the study of ACK09. As the aerosol-cloud droplet parameterisation is applied in two schemes of DALES (the microphysics and radiation scheme), one additional simulation will be performed with the parameterisation included in only the microphysics scheme and one with the parameterisation included in both the microphysics and radiation scheme. An inter-comparison will be made of the results of these three models by the hand of both time- and domain-averaged vertical profiles of parameters that give insight into the state of the simulated STBL and time evolutions of a selection of parameters to further elucidate the effects of incorporating the parameterisation. The selected parameters to be assessed are the same as the parameters in ACK09, which enables the assessment of the STBL state and the comparison of the simulated profiles by DALES and the results presented in ACK09.

4.1.1. Aerosol Input

In the standard DALES model, a constant cloud droplet number concentration is prescribed, which is also the case for some of the models tested in the literature mentioned above. To be able to compare the output of the modified model with the literature, a constant N_d in terms of m^{-3} is required here as well. To implement a constant N_d and to prevent the occurrence of aerosol advection due to gradients in N_{ae} in the modified model, the modified subroutines make use of the standard Twohy parameterisation as in Eq. (2.8) instead of Eq. (3.1). Consequently, the input profiles of N_{ae} are constant as well and have a unit of m^{-3} instead of kg^{-1} . The cloud droplet number concentration used in ACK09, and therefore also for the RF02 validation simulations, is $N_d = 55 \text{ cm}^{-3}$. Using Eq. (2.8), this equates to a N_{ae} of 58.5 cm^{-3} .

4.1.2. Settings and Simulation Domain

Corresponding to ACK09, the horizontal grid is 128 by 128 points horizontally and 160 points vertically with a grid spacing of 25 m and 10 m in the horizontal and vertical direction, respectively. The simulation time is 6 hours, in which every 60 seconds statistics are sampled. These samples are averaged every 300 seconds and written to the output files.

As the measurements were obtained during nighttime, in which shortwave radiation is absent, shortwave radiation is set to zero throughout the simulation. This way, solar radiation does not play a role in the duration of the simulation. This is comparable with the approach of the study of ACK09, in which only longwave radiation is considered in the radiation budget.

It must be noted that the radiation scheme applied in this research differs from the scheme used in the study of ACK09, which uses the more basic radiation scheme described in Stevens et al. (2005). In this scheme, the net longwave radiative flux is based on simplified parameterisations of cloud-top cooling, cloud-base warming and free-tropospheric cooling. The radiation scheme applied for this research performs more detailed parameterisation by considering multiple wavebands and physical parameters in its calculations.

4.2. Validation of Model Adjustments

Figure 4.1 shows the time evolutions of LWP, w_e , the maximum of the vertical velocity variance and the precipitation rate at the surface $R_{r, sfc}$ for the models building up to the final model used for this thesis. The standard DALES model is represented by the solid blue line. The model with adjustments in the microphysics scheme is represented by the dashed orange line. The green dotted line corresponds to the final model, including both the adjustments in the microphysics scheme and the radiation scheme. The generated time evolutions of the quantities show differences between the model versions. After approximately one hour, the results start to differentiate slightly, after which deviations become more pronounced. The differences after about one hour can be attributed to the difference in how the models treat parameters that represent the cloud droplet number concentration in the simulation schemes. As stated earlier, the standard DALES model represents N_d as a constant, which is exactly equal to 55 cm^{-3} in this simulation. In the modified versions, however, N_d is a parameter that is dependent on $N_{ae, kg}$, which is represented by a prognostic scalar. Although the effects of subsidence, advection and diffusion are kept to a minimum for these simulations by assuming a vertically uniform air density, the generated tendencies of $N_{ae, kg}$ and consequently for N_d are unequal to zero, which is the case for a constant N_d in the standard DALES model. As time progresses, these minimal changes cause accumulating small perturbations in the parameters that are influenced by N_d , which eventually generates more pronounced deviations such as found in Figure 4.1. Due to the feedback mechanisms between the physical parameters, small early-phase perturbations can be amplified as time progresses. This amplification is found in

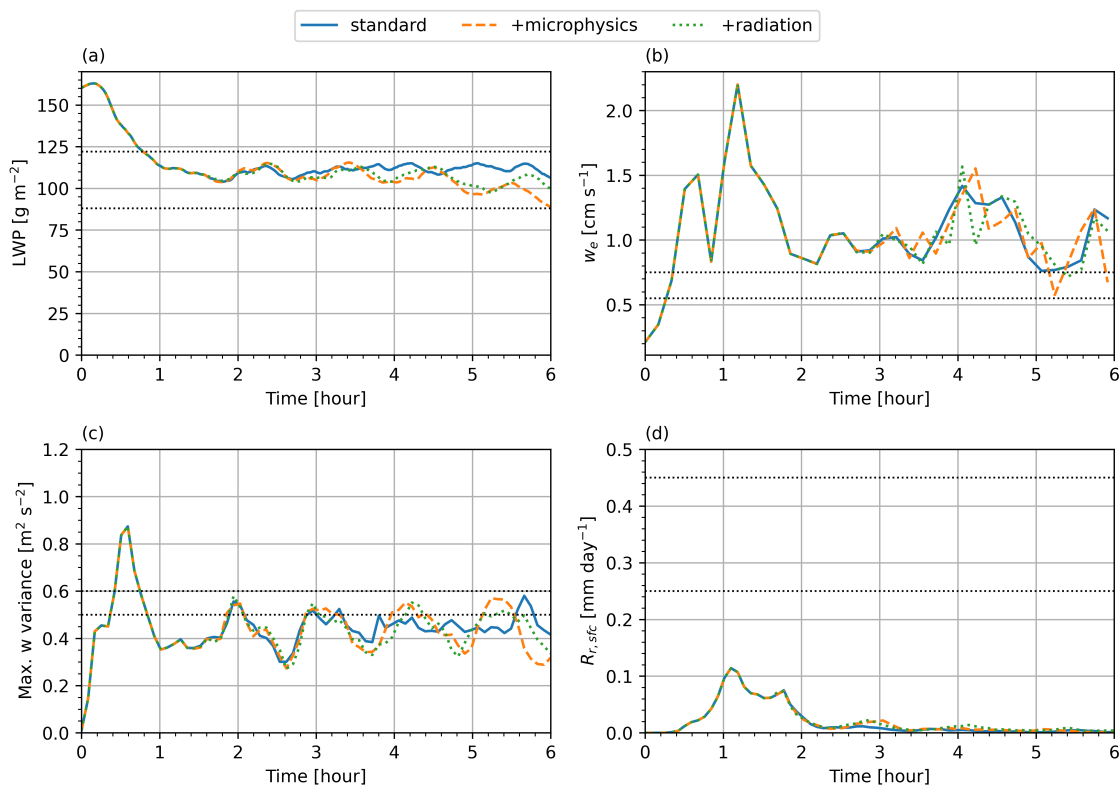


Figure 4.1: Time series of the domain-averages of (a) liquid water path, (b) entrainment rate, (c) the maximum of the variance in vertical velocity w and (d) the surface precipitation of the RF02 case. 'standard' (blue) represents the results of the unmodified standard DALES model, '+microphysics' (orange) represents the results after including the aerosol-cloud droplet parameterisation in the scheme treating the microphysics, and '+radiation' (green) represents the results after including both the aerosol-cloud droplet parameterisation in both the microphysics scheme and the radiation scheme. The black dotted lines represent the approximate ranges of the observations.

the study of Jansson et al. (2021) as well, who showed (using DALES) that small perturbations in initial parameter quantities, such as N_d , generate significantly varying results at the end of the simulations.

Figure 4.2 shows vertical profiles of various parameters, time-averaged over the last four hours of the six-hour simulations. Despite that the time evolutions in Figure 4.1 are not exactly alike, the nearly exact agreement of the mean vertical profiles suggests no significant artefacts due to the adjustments made to the standard DALES model. This indicates that the state of the simulated boundary layer can be assumed to be unchanged despite the changes in the DALES model. This puts confidence in the appropriateness of the model modifications and the reliability of the new model. The implications of the profiles are discussed in Section 4.3.

4.3. Output Comparison with Other LES Models

In Figure 4.1(a), it is shown that the generated LWP suits the observed range (represented by the black dotted lines) of LWP very well and corresponds closely to the mean LWP time series found in the study of ACK09. This indicates no significant under- or overestimation of the LWP in the DALES simulations compared to the other model simulations and a similar net balance between the processes that contribute to the LWP budget. If there were a significant difference in generated LWP, various cloud parameters would be affected, such as cloud albedo, precipitation rate, and sedimentation rate, which causes differences to be magnified through

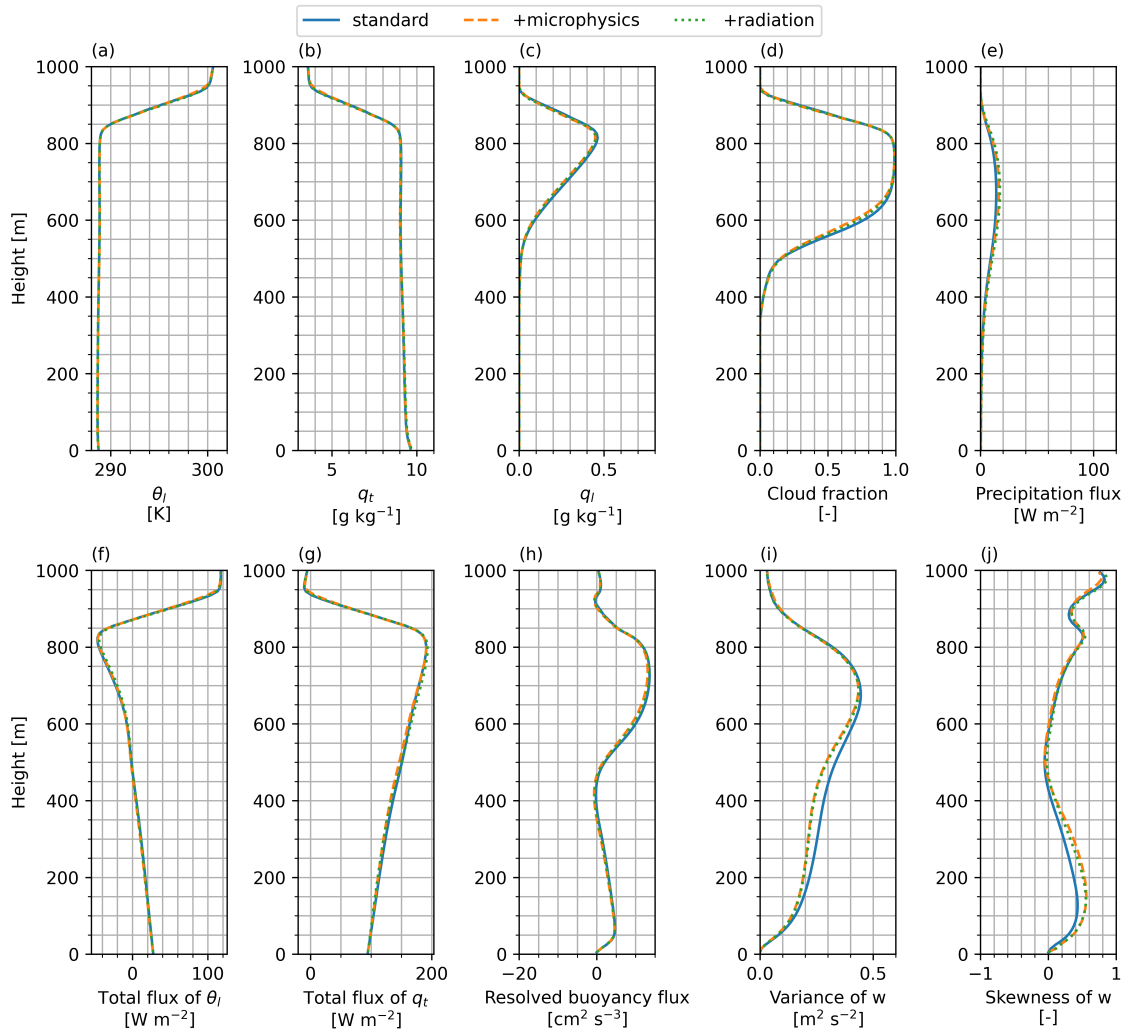


Figure 4.2: Time- and horizontally-averaged vertical profiles of (a) the liquid water potential temperature θ_l , (b) the total water mixing ratio q_t , (c) the liquid water mixing ratio q_l , (d) cloud fraction, (e) precipitation flux, (f) total flux of θ_l (including radiation and precipitation flux), (g) total flux of q_t (including precipitation flux), (h) buoyancy flux, (i) variance of the vertical velocity and (j) the skewness in the vertical velocity of the RF02 case. Time-averages are taken over the last four hours of the six-hour simulations. The coloured lines are represented as in Figure 4.1.

the feedback mechanisms. However, the net balance of the processes that govern the LWP budget may be similar, but when the magnitudes of these processes differ compared to those generated by the other models (which can be found in ACK09), this could change the state of the STBL. For example, a mainly entrainment-driven LWP loss deepens the boundary layer depth, whereas a more precipitation-driven LWP loss can cause decoupling to occur. Because the state of the STBL implies different reactions to an enhancement in N_d , it is important to analyse the other profiles of Figures 4.1 and 4.2 to assess the generated differences in the state of the STBL.

Figures 4.2(a), (b), (c) and (d) are in close agreement with the profiles generated by the models in ACK09 and will therefore not be further analysed. The precipitation flux in Figure 4.2(e) generated by DALES is significantly less than the mean profile found in ACK09, showing a peak precipitation flux of about 80 W m^{-2} and a precipitation flux at the surface of around 5 W m^{-2} . In addition, the time evolutions of the surface precipitation rates modelled by DALES in Figure 4.1(d) correspond to the smallest results generated by the models in ACK09. The mean precipitation rate generated by these models is consistent throughout the entire simulation and more than double the maximum precipitation rate generated in the DALES simulations. This indicates that either precipitation is considerably evaporated before reaching the surface, or the precipitation on all levels is relatively small. If the former is true, this can cause the sub-cloud layer to cool, stabilising the boundary layer and causing decoupling. If the latter is true, aerosol concentration enhancement to suppress precipitation will be less effective in maintaining the LWP when using DALES than when using other models with higher precipitation rates.

The total fluxes of θ_t and q_t in Figures 4.2(f) and 4.2(g), respectively, include the advective, subgrid-scale and precipitation fluxes, and for θ_t radiation fluxes as well. The negative slope with height of the total flux in θ_t shows warming of the boundary layer, which is also found in the simulations of the other models in ACK09, although to a smaller degree. The more negative slope and the smaller surface flux of θ_t , which is around 40 W m^{-2} in ACK09, is mostly attributed to the smaller precipitation flux in our simulations. The positive slope of the total water mixing ratio flux indicates drying of the boundary layer, which is in disagreement with the mean of the other models, that shows no gradient except a small indication of a moistening tendency (negative gradient) near the cloud top (ACK09).

Figures 4.2(h) and (i) and 4.1(c) show indications of decoupling: The maximum in the variance of vertical velocity w indicates the intensity of the convection in the boundary layer. The mean values of the other models show an underestimation compared to the observation range with a nearly constant value of about $0.35 \text{ m}^2 \text{ s}^{-2}$. DALES shows a higher maximum vertical velocity over time and corresponds more closely to the observations, although generally still smaller. ACK09 suggest that the smaller simulated convection intensity is an indication for decoupling. The slightly negative buoyancy flux at the cloud-base and the cloud-base minimum in vertical velocity variance in Figure 4.2(h) further support this suggestion (Stevens et al. (2005)). The skewness in Figure 4.2(j) is more neutral near the cloud-base with respect to the positively skewed mean value in ACK09, indicating a more balanced ratio between updrafts and downdrafts near the cloud-base. The profile generated in our simulations is in better agreement with the observations, which even show a negatively skewed vertical velocity near the cloud-base.

The last figure to be discussed is Figure 4.1(b), showing the entrainment rate in time. The entrainment generated by DALES is relatively large compared to entrainment rates of the other models, which show a mean value of approximately 0.6 cm s^{-1} over the last four hours and correspond well to the observations. The higher entrainment rate causes the cloud to dissolve

faster at the cloud-top and deepens the boundary layer quicker than simulated by the other models. That the LWP profile of our simulations still matches the mean LWP profile found in ACK09 is mainly attributed to the difference in the modelled longwave radiation. The parameterised longwave radiation applied in ACK09, which can be found in the study of Stevens et al. (2005), generates weaker longwave radiative cooling at the cloud-top than generated by the radiation transfer model that is applied in our simulations. This compensates for the loss of LWP due to the higher entrainment rate. In addition, the smaller surface precipitation rate in our simulations causes the cloud to lose less water and maintain a higher LWP as well.

As already shortly stated for the deviations in the modelled precipitation rates, the differences in the STBL properties and state have consequences in the effect of MCB activities. Both the relatively higher entrainment rate and lower precipitation rate modelled by DALES have a diminishing effect on the efficacy of cloud seeding. The higher entrainment rate causes the cloud to lose its LWP quicker through evaporation at the cloud-top, which is expected to be enhanced due to the smaller cloud droplets. Due to the lower precipitation rate, the potential positive effect on the LWP of precipitation suppression is reduced, which decreases the efficacy of MCB as well.

5

Cloud Seeding Simulations

In this chapter, we discuss and analyse the marine cloud brightening simulations. These simulations are comparable in setup with the simulations in WANG11, but with higher accuracy in the modelling of small-scale mixing processes. First, additional theoretical background will be provided to explain how the results are analysed. Next, the simulation setup for the MCB simulations will be given, after which the results will be analysed. The analysis is split into two parts: similar to previous research, the first part consists of the analysis on a selection of key cloud properties for the solar radiation reflection. In the second part, we aim to expand the knowledge of previous research by analysing the processes contributing to the LWP tendencies and their feedback effects.

For the result analysis, the cases that showed the most promising results on the efficacy for albedo enhancement in the study of WANG11 are discussed first and most extensively. For conciseness, only the results that deviate from these cases will be discussed for the other experiments. To provide the reader with a clear overview of the results, each section in which the results are discussed ends with a summary of the most important findings.

In both the analysis of the reflection enhancement and the LWP, we use the domain-averaged values of the parameters, as this is most practical for our analysis. However, additional figures are provided in Section C of the appendix for visualisation, showing the two-dimensional horizontal plane of the cloud albedo A_c , liquid water path LWP and the vertically integrated aerosol number concentration N_{ae} of the W50 experiments, for a range of moments during daytime. When assumed useful, these figures will be referred to in this chapter's footnotes, providing a brief explanation. We chose to provide the two-dimensional figures for the W50 experiments only, because they show the most considerable differences in the shown parameters compared to the other cases, as will become evident in the result analysis, and are sufficient to provide additional explanation to the results concisely.

5.1. Additional Theoretical Background

To assess the effect of the MCB activities performed in this thesis, the analysis will be performed by examining the first and the second indirect aerosol effect. Therefore, the focus will be on the changes in albedo and LWP. The former is done with the use of an alternative definition of albedo with respect to the one defined in Eq. (2.1) and thus requires additional explanation. The latter is done based on the research of Van der Dussen et al. (2014) and its approach for the LWP analysis will be explained as well.

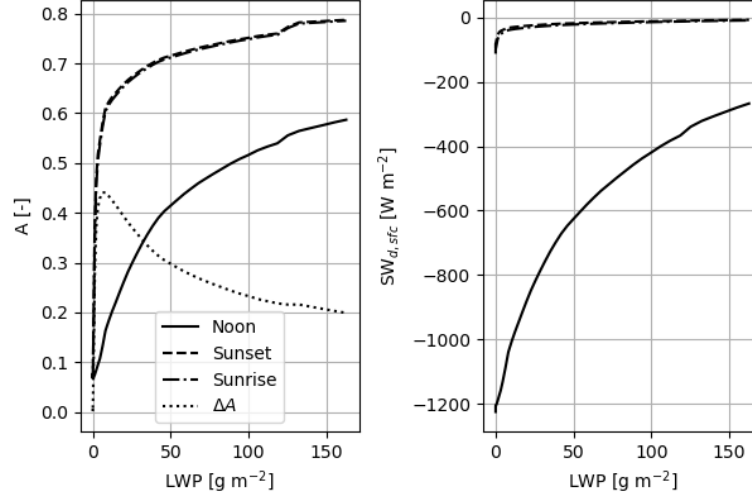


Figure 5.1: Effective albedo (left) and downwelling shortwave radiation at the surface (right) versus LWP at sunrise, noon and sunset, showing the dependency of the cloud's reflective capability on the angle at which the solar radiation enters the cloud layer. All other physical conditions are unchanged among the varying LWP and time of day, which therefore do not affect the cloud albedo. ΔA is the difference between albedo at sunrise and at noon.

5.1.1. Alternative Definition of Albedo

As stated, we use a different definition for the albedo than the commonly used cloud albedo (A_c), whose definition is based on the physical cloud parameters such as in Eq. (2.1). Instead, we define the so-called effective albedo (A), which is the ratio of the horizontally-averaged upwelling and downwelling shortwave radiation (SW_u and SW_d , respectively) at a fixed altitude:

$$A = \frac{SW_u}{SW_d} \quad (5.1)$$

The reason for using this definition for the albedo is that the reflective capability of the cloud depends on the angle at which incoming solar radiation reaches the cloud layer. This angle, the solar zenith angle (θ_z), relies on the day of the year, time of day and the location of the simulated cloud on Earth's surface (Cronin, 2014). θ_z is the angle between the incoming solar radiation and the line perpendicular to the surface plane. For large θ_z (corresponding to sunrise and sunset), the retrieved A differs for clouds with the same microphysical conditions and hence equal A_c . Figure 5.1 shows A and the downwelling shortwave radiation reaching the surface $SW_{d,src}$ as a function of LWP for one-second simulations at sunrise, noon and sunset. All other physical conditions are kept equal, such that it does not influence the cloud conditions. Hence, changes in LWP is proportional to changes in r_e and directly related to modifying the optical thickness τ (see Eq. (2.5)). Figure 5.1 shows that the time of day is crucial for the reflectivity of the cloud. First of all, $SW_{d,src}$ in the absence of clouds (LWP = 0 g m⁻²) is much lower at sunrise (or sunset) than at noon. This indicates that when an average radiative forcing of -21.1 W m^{-2} is desired, modifications in A are most effective when the sun is located highest in the sky. Moreover, the figure on the left shows that the difference between A at sunrise (or sunset) and at noon is significant for all LWP. This can be explained by the fact that the angle at which the radiation is incident on the cloud determines the path length through the cloud layer. Arriving at the cloud at an angle increases the path length in which the solar radiation can be reflected. Figure 5.1 shows that for small θ_z , the enhancement in A is only efficient in the lowest LWP (and thus τ) region with respect to enhancement during the middle of the day.

This indicates that not the time-averaged difference in cloud albedo A_c due to cloud seeding

is of interest, but rather the connection between the time of day and the corresponding albedo enhancement. In other words: A gives more insight into the actual effectiveness of MCB on the radiative budget, because it takes the effect of θ_z into account. An increase in either LWP or r_e is thus less effective for large θ_z than for small θ_z . This is not the case for A_c , which could be misleading when deriving the effectiveness of MCB.

In addition, the objective to enhance the cloud albedo with 0.062, as determined by Latham et al. (2008), is derived using the average solar irradiance received at the surface of the Earth. This suggests that the 24-hour-average of A_c of every stratocumulus cloud over Earth's oceans should be increased by 0.062. However, when assessing the MCB effectiveness locally, the distribution of the enhancement in time should be taken into consideration, as explained above. It is noted that this is not done in the research of WANG11, which only looks at A_c over the last 24 hours of the simulation and does not state the results of the generated radiative forcing. The reason for using A_c instead of A remains unclear for their study, but can be explained by that this either allows them to include the albedo during nighttime, or that a diurnal mean solar irradiance is applied, which does not incorporate the solar zenith angle. Values of A_c corresponding to nighttime are thus taken into consideration as well by WANG11, which do affect the average A_c over 24 hours but not the radiative forcing on the simulated domain. Because their results show significant enhancement during daytime well above 0.062, this does not refute their conclusions.

In order to prevent potential misjudgement of the simulations results, the profiles of A will be used to show if the enhancements in N_{ae} are effective in increasing the fraction of reflected solar radiation. Although A can be high when the radiative fluxes are low, A provides insight into the reflective capability of the cloud, even when SW_{d,sf_c} is low. However, using SW_{d,sf_c} is most suitable to assess the effectiveness of MCB activities, as it directly indicates whether the objective of 21.1 W m^{-2} (as derived by Latham et al. (2008)) can be met.

5.1.2. LWP Tendency Contributors

To assess the second indirect aerosol effect, the effect of the aerosol injection to the cloud's LWP, the study of Van der Dussen et al. (2014) is used. In this study, a budget equation for the LWP of a vertically well-mixed stratocumulus cloud layer is derived that allows for the separate analysis of the different physical mechanisms that contribute to a net cloud thinning or thickening effect. Without going into the derivations of the budget equation, the total LWP tendency consists of the contributions of five physical processes: the turbulent fluxes at the cloud base (abbreviated with Base), entrainment (Ent), radiation (Rad), precipitation (Prec) and subsidence (Subs):

$$\frac{\partial LWP}{\partial t} = \frac{\partial LWP}{\partial t} |_{Ent} + \frac{\partial LWP}{\partial t} |_{Base} + \frac{\partial LWP}{\partial t} |_{Rad} + \frac{\partial LWP}{\partial t} |_{Prec} + \frac{\partial LWP}{\partial t} |_{Subs} \quad (5.2)$$

The contribution of entrainment to the LWP tendency is given by:

$$\frac{\partial LWP}{\partial t} |_{Ent} = \rho_{air} w_e (\eta \Delta q_t - \Pi \gamma \eta \Delta \theta_l - h \Gamma_{q_l}) \quad (5.3)$$

Here, ρ_{air} is the total air density at the cloud-top and w_e is the entrainment rate. η is a variable that accounts for the latent heat release and uptake as a consequence of condensation and evaporation, respectively. It is given by $\eta = \left(1 + \frac{L_v \gamma}{c_p}\right)^{-1}$, where L_v is the latent heat of vaporization of water, $\gamma = \frac{\partial q_s}{\partial T}$ is the change of saturation specific humidity q_s with temperature T and c_p is the specific heat capacity of air. Further, $\Pi = \frac{T}{\theta}$ is the Exner function, which assumed

to be approximately constant throughout the cloud layer, with θ the potential temperature. $\Delta\theta_l$ is the difference in θ_l just above the inversion layer and just below it. $\Gamma_{q_l} = \frac{\partial q_l}{\partial z} = \frac{q_l^t}{h}$ is the lapse rate of the liquid water specific humidity, where q_l is assumed to vary approximately linearly with height in the cloud layer and q_l^t is the value of q_l at the cloud-top. Eq. (5.3) shows that a moist free-troposphere reduces the thinning effect due to entrainment, whereas warmer free-tropospheric air increases cloud thinning.

The LWP tendency due to the turbulent fluxes at the cloud base is given by:

$$\frac{\partial LWP}{\partial t} \Big|_{Base} = \rho_{air}\eta(\overline{w'q_t^b} - \Pi\gamma\overline{w'\theta_l^b}), \quad (5.4)$$

where $\overline{w'q_t^b}$ and $\overline{w'\theta_l^b}$ are the turbulent fluxes at the cloud-base of q_t and θ_l , respectively. The turbulent flux of q_t has a moistening and thickening effect at the cloud base, whereas the turbulent flux of θ_l has a drying and thinning effect.

The effect of longwave radiation in the cloud layer is taken into account in the follow equation:

$$\frac{\partial LWP}{\partial t} \Big|_{Rad} = \rho_{air}\eta\gamma\delta F_{rad} \quad (5.5)$$

Here, δF_{rad} (in K m s^{-1}) indicates the difference between the longwave radiation at cloud-top and cloud-base, such that $\delta F_{rad} > 0$ due to the strong longwave cooling at the cloud-top (Wood, 2012)¹. As described in Section 2.2.1, precipitation reduces the LWP of the cloud layer:

$$\frac{\partial LWP}{\partial t} \Big|_{Prec} = -\rho_{air}\delta P, \quad (5.6)$$

where δP is the difference between the precipitation rate at cloud-top and cloud-base. As no precipitation enters the cloud layer from above and the precipitation flux is defined negative downward, $\delta P > 0$ and is equal to the precipitation at cloud-base in m s^{-1} . Finally, the contribution of the large-scale subsidence to the LWP tendency is given by:

$$\frac{\partial LWP}{\partial t} \Big|_{Subs} = -\rho_{air}h\Gamma_{q_l}\overline{w}(z_i) \quad (5.7)$$

Here, $\overline{w}(z_i)$ is the large-scale vertical velocity of the inversion height. As Γ_{q_l} is negative, a positive $\overline{w}(z_i)$ indicates thickening of the cloud.

It is important to state that this analysis method does not account for the interactions between the cloud-governing processes and is based on the instantaneous state of the cloud layer. Changes in LWP of the cloud layer affect the radiative fluxes, precipitation and entrainment on a short time scale, whereas the inversion jumps Δq_t and θ_l as well as the humidity flux at the cloud base are affected on a longer time scale. However, it does give insight into how changes in these parameters due to cloud seeding and due to feedback mechanisms influence the cloud thickness and thereby its effect on the radiative balance.

¹What was not accounted for in the study of Van der Dussen et al. (2014), was the radiative effect of the humidity that overlays the entraining humidity of the free-troposphere. Eastman and Wood (2018) show that the downwelling longwave radiation of the humidity above the STBL reduces the energy loss to upwelling radiation at the cloud-top. This reduces cloud-top cooling and lowers the stability of the STBL, which causes an increase in entrainment, deepening of the STBL and ultimately breakup of the stratocumulus cloud. The effects of entraining humidity and radiating humidity on the cloud lifetime thus seem to compete and require both to be taken into account when studying cloud lifetime and cloud feedback processes.

Table 5.1: Overview of the MCB experiments. The dry (D) and wet (W) conditions correspond to the research flights RF01 and RF02, respectively. The uniform injection method refers to the uniform injection of aerosols across the entire surface area. The point source injection method indicates the aerosol injection from a single grid point of the surface area, located at the upwind corner of the domain.

| Experiment | Initial LWP [g m ⁻²] | Background $N_{ae,kg}$ [mg ⁻¹] | Injection method |
|------------|-------------------------------------|---|------------------|
| W100 | 152 | 100 | None |
| W100-U | 152 | 100 | Uniform |
| W100-P | 152 | 100 | Point source |
| W50 | 152 | 50 | None |
| W50-U | 152 | 50 | Uniform |
| W50-P | 152 | 50 | Point source |
| W200 | 152 | 200 | None |
| W200-U | 152 | 200 | Uniform |
| W200-P | 152 | 200 | Point source |
| D100 | 40 | 100 | None |
| D100-U | 40 | 100 | Uniform |
| D100-P | 40 | 100 | Point source |
| D50 | 40 | 50 | None |
| D50-U | 40 | 50 | Uniform |
| D50-P | 40 | 50 | Point source |
| D200 | 40 | 200 | None |
| D200-U | 40 | 200 | Uniform |
| D200-P | 40 | 200 | Point source |

5.2. Simulation Setup

The MCB simulations make use of Eq. (3.1) for the aerosol activation parameterisation. In these simulations, both the RF01 and RF02 cases will be simulated, to which no source, a homogeneous source and a point source for the aerosols will be implemented at the surface of the domain. Following the notation used by WANG11, simulations based on RF01 will be referred to as dry (D) and on RF02 as wet (W) in the experiment name, followed by its initial aerosol background concentration and injection method (U for uniform and P for point source). An overview of the simulations is given in Table 5.1.

5.2.1. Aerosol Input

Three initial background conditions for $N_{ae,kg}$ are used to represent an average ($N_{ae,kg} = 100$ mg⁻¹), a cleaner ($N_{ae,kg} = 50$ mg⁻¹) and a more pollute ($N_{ae,kg} = 200$ mg⁻¹) maritime environment. All initial background conditions are vertically uniform. For the clean environment, the aerosol number concentration is $N_{ae} = \rho_{air}(z)N_{ae,kg} \approx 55$ cm⁻³ at the altitudes at which the clouds are formed, which is slightly below the approximate minimum value of the range to which the parameterisation of Eq. (2.8) applies. However, near this minimum value the equation is nearly linear and no significant error is expected when extrapolating the parameterisation to this concentration.

The aerosol source rate is set to $1.45 \cdot 10^6$ m⁻² s⁻¹ as suggested by Salter et al. (2008) and used by WANG11. For the homogeneous source, the injected aerosols are uniformly distributed over all grid boxes, whereas for the point source, it is concentrated in a single grid box upon injection. In the study of Salter et al. (2008), it is assumed that one source is able to seed an area of $7.72 \cdot 10^{10}$ m², which is about a factor 100 larger than the area of our

simulations. This results in a point source rate that is approximately 100 times smaller than what is assumed to be maximally feasible by Salter et al. (2008).

WANG11 included an additional source to account for the loss of aerosols due to cloud drop coalescence and wet removal with a steady source rate of $2 \text{ mg}^{-1} \text{ h}^{-1}$. As stated earlier, our simulations do not include the aerosol sinks due to these processes. This can be regarded as a simplification in which removed aerosols are instantly and fully replenished. Hence, we add no additional steady source in our simulations.

5.2.2. Settings and Simulation Domain

The simulations are set up in such a manner that is as much in line with the setup of the study of WANG11. However, some deviations were required for the practicality of this thesis. The first deviation is made for the domain settings. The large domain of size $60 \times 120 \times 1.5 \text{ km}^3$ with a grid spacing of 300 m horizontally and approximately 30 m in the vertical, as simulated by WANG11, was not feasible for this thesis due to computational costs. The domain size used here is $25.2 \times 25.2 \times 2 \text{ km}^3$ with a 100 m horizontal and 10 m vertical grid spacing. The advantage of the finer grid spacing is that the contribution of the sub-grid eddy parameterisation is smaller. The disadvantage is that the simulations including the point source will have a higher number of sources per square kilometre (or source density P_s) than simulated in the study of WANG11. In the simulations of this report $P_s \approx 1.6 \cdot 10^{-3} \text{ km}^{-2}$ compared to $P_s \approx 1.4 \cdot 10^{-4} \text{ km}^{-2}$ for the point source in the study of WANG11.

The second deviation is the horizontal movement of the point source through the domain. In our simulations, the sources are stationary and the horizontal distribution of the aerosols is regulated by the winds. WANG11, however, mimicked the wind-driven spray-vessels proposed by Salter et al. (2008) by moving the point source at a steady velocity (5 m s^{-1}) through the domain. By removing the mean winds from the initial soundings to prevent significant advection of the sprayer tracks, they let the source movement be the main driver of the horizontal distribution instead of the winds in our simulations.

5.3. Results: Wet STBL with Average and Clean Pollution Levels

The simulations that we discuss firstly are the meteorological cases corresponding to RF02 (the moister STBL) with initial $N_{ae,kg}$ of 100 cm^{-3} and 50 cm^{-3} , corresponding to respectively average and clean maritime pollution levels. These two cases appeared to be most susceptible to cloud injections of aerosols in WANG11.

5.3.1. Reflection Enhancement

Figures 5.2 and 5.3 show the results of respectively the W100 and W50 experiments using no source (W100, W50, the base case), a uniformly distributed aerosol source (W100-U, W50-U) and an aerosol point source (W100-P, W50-P). The effective albedo (A) and cloud albedo (A_c) as a function of time in Figure 5.2(a) show correlation by decreasing during daytime to a minimum after around 14 hours and restoring until the start of the second night. As mentioned in Section 5.1.1, the effective albedo accounts for both the solar zenith angle and the amount of cloud cover in the domain, which is evident from the more pronounced reduction of A compared to A_c . Relative changes in A due to cloud seeding are minimal for the W100 simulations, showing mean enhancement of 0.008 (W100-U) and 0.004 (W100-P) taken over the last 24 hours of the simulation, as can be seen in Table 5.2². The aerosol injection causes a mean reduction in $SW_{d,afc}$ compared to the base case W100 for both the uniform and the point

²Tables 5.3 and 5.4 are shown in advance for the ease of comparison, but will be discussed in Sections 5.4 and 5.5.

source seeding strategy. The difference in downwelling shortwave radiation at the surface with respect to the base case W100 $\Delta SW_{d,sfc}$ (presented in Figure 5.2(b)) shows moments where $\Delta SW_{d,sfc}$ is positive. A positive $\Delta SW_{d,sfc}$ indicates an increase in shortwave radiation reaching the surface and a negative $\Delta SW_{d,sfc}$ indicates a reduction in shortwave radiation reaching the surface. These positive peaks in $\Delta SW_{d,sfc}$ correspond to a slightly lower A , LWP and cloud fraction for the seeded cases compared to the base case.

Although the LWP and cloud fraction of W50-U are smaller than that of W50 between 12 and 18 hours, $\Delta SW_{d,sfc}$ is only positive shortly around 14 hours. This can be attributed to the positive effect of the increase in N_d having a larger impact on the cloud reflectivity than the negative effect of the reduction in LWP compared to the base case.

Table 5.2: Domain- and time-averaged effective albedo (\bar{A}), cloud albedo (\bar{A}_c), downwelling shortwave radiation at the surface ($\overline{SW_{d,sfc}}$) and their relative changes compared to the baseline simulations for the RF02 case with average (100 cm^{-3}) and clean (50 cm^{-3}) initial maritime aerosol number concentrations. The time-averages are taken over the last 24 hours of the 30-hour simulations.

| Experiment | W100 | W100-U | W100-P | W50 | W50-U | W50-P |
|--|-------|--------|--------|-------|-------|-------|
| \bar{A} [-] | 0.350 | 0.358 | 0.355 | 0.321 | 0.340 | 0.339 |
| \bar{A}_c [-] | 0.327 | 0.338 | 0.341 | 0.296 | 0.324 | 0.325 |
| $\overline{SW_{d,sfc}}$ [W m^{-2}] | 274.1 | 270.7 | 270.9 | 286.6 | 277.9 | 277.3 |
| $\Delta \bar{A}$ [-] | - | 0.008 | 0.004 | - | 0.018 | 0.018 |
| $\Delta \bar{A}_c$ [-] | - | 0.011 | 0.015 | - | 0.028 | 0.029 |
| $\Delta \overline{SW_{d,sfc}}$ [W m^{-2}] | - | -3.5 | -3.2 | - | -8.7 | -9.3 |

Table 5.3: Same as in Table 5.2, but for the drier and warmer RF01 case.

| Experiment | D100 | D100-U | D100-P | D50 | D50-U | D50-P |
|--|-------|--------|--------|-------|-------|-------|
| \bar{A} [-] | 0.320 | 0.331 | 0.335 | 0.299 | 0.322 | 0.317 |
| \bar{A}_c [-] | 0.283 | 0.307 | 0.309 | 0.260 | 0.294 | 0.297 |
| $\overline{SW_{d,sfc}}$ [W m^{-2}] | 300.8 | 296.5 | 294.6 | 311.0 | 301.4 | 302.9 |
| $\Delta \bar{A}$ [-] | - | 0.010 | 0.015 | - | 0.023 | 0.018 |
| $\Delta \bar{A}_c$ [-] | - | 0.024 | 0.026 | - | 0.034 | 0.037 |
| $\Delta \overline{SW_{d,sfc}}$ [W m^{-2}] | - | -4.3 | -6.3 | - | -9.6 | -8.1 |

Table 5.4: Same as in Table 5.2, but for both RF02 case and the drier and warmer RF01 case, with polluted (200 cm^{-3}) initial maritime aerosol number concentrations.

| Experiment | W200 | W200-U | W200-P | D200 | D200-U | D200-P |
|--|-------|--------|--------|-------|--------|--------|
| \bar{A} [-] | 0.363 | 0.367 | 0.364 | 0.337 | 0.343 | 0.342 |
| \bar{A}_c [-] | 0.351 | 0.357 | 0.361 | 0.312 | 0.328 | 0.326 |
| $\overline{SW_{d,sfc}}$ [W m^{-2}] | 266.7 | 266.2 | 267.3 | 293.2 | 290.3 | 291.9 |
| $\Delta \bar{A}$ [-] | - | 0.004 | 0.001 | - | 0.006 | 0.005 |
| $\Delta \bar{A}_c$ [-] | - | 0.006 | 0.010 | - | 0.015 | 0.013 |
| $\Delta \overline{SW_{d,sfc}}$ [W m^{-2}] | - | -0.5 | 0.6 | - | -2.9 | -1.2 |

Notably, the second positive peak in $\Delta SW_{d,sfc}$ at around 16 hours in Figure 5.2(b) is not evident from the differences in A_c , where the seeded cases have an about equal A_c as the base case. However, the cloud fractions of W100-U and W100-P are lower than that of W100, and less solar radiation encounters a cloud layer on its path. This stresses the importance of the cloud fraction, which causes an increase in $\overline{SW_{d,sfc}}$ when the cloud fraction is reduced, even if the remaining cloud has a higher A_c . The cloud fraction is most important at midday when the solar radiation incidence is perpendicular to the cloud layer. As stated earlier, the definition

of A indirectly incorporates the role of the cloud fraction. Because the cloud cover of W100-P is generally lower during the day compared to the cloud cover of W100-U, this explains the smaller difference in effective albedo $\Delta\bar{A}$ of W100-P than found for W100-U, despite the larger difference in cloud albedo $\Delta\bar{A}_c$ found for W100-P compared to that of W100-U.

For the W100 cases, the aerosol seeding-induced enhancement of A_c is most pronounced during the second night. Naturally, nighttime-albedo enhancement has no effect on cooling the Earth's surface and including these values in the assessment of the efficacy of MCB can be misleading. The difference in mean cloud albedo over the daytime only is about 0.008 for W100-U and 0.01 for W100-P. The effective reduction in downwelling shortwave radiation at the surface indicates that the contribution is approximately one-sixth of the 21.1 W m^{-2} reduction proposed by Latham et al. (2008).

Figure 5.3(a) shows that the aerosol concentration enhancement induces a stronger effect on both A and A_c in the clean environment than in the average environment, especially throughout the first half of the day and during the second night. This is reflected in the day-averaged differences in A and A_c shown in Table 5.2, which are both significantly larger than for the W100 cases. This causes the aerosol concentration enhancement to have a stronger cooling effect than for W100, as shown in the nearly tripled reduction of $SW_{d,afc}$ for W50 with respect to the reduction generated by the aerosol injection in the W100 case.

The loss in both A and A_c corresponds to the fast reducing LWP starting just before sunrise, as shown in Figures 5.2(d) and 5.3(d)³. After reaching the minimum, the LWP shows a slight increase until sunset, which is reflected in the increase in A_c in the same time interval for all simulations of W100 and W50. What processes are the drivers of the LWP loss will be examined in detail in Section 5.3.2. The strong influence of entrainment is already indicated in Figures 5.2(e) and 5.3(e), as entrainment at the cloud-top causes the cloud-top to rise and the drier and the cloud layer to warm, which increases in the cloud-base height.

Both aerosol seeding strategies in the W50 cases cause the cloud to hold more liquid water before the start of the day. In combination with the increased N_d , this positively contributes to the enhancement of A and A_c ⁴. That the LWP mainly drives the albedo enhancement during sunset and sunrise can be deduced from the fact that the enhancement of N_d for W100 and W50 are approximately equal, but no albedo enhancement is generated in the W100 cases where the LWPs are about the same at the start of the day. With the same enhancement in N_d but an increased LWP, the seeded cases of W50 do show an increase in albedo.

The cloud-base and surface precipitation rates of the W100 cases are shown in Figure 5.2(f). As expected from the second indirect aerosol effect, cloud seeding causes the precipitation rate to diminish. This is most effective for a uniform aerosol source, which shows the largest decrease in precipitation rate near cloud-base. The uniform aerosol spray covers the entire domain and is able to suppress a larger fraction of the initial precipitation. The more concentrated point source might locally suppress rain-out more effectively, but has less effect over the domain as a whole. Only a minimal amount of precipitation reaches the surface, which indicates that nearly all precipitation is evaporated between the cloud-base and the surface. This can contribute to decoupling and the cloud layer being disconnected from the moisture supply. The indication of decoupling is additionally indicated by the vertical profile of the buoyancy flux showing negative values near cloud-base between 8 and 16 hours and the minimum

³The reduction in LWP and A_c in time are shown in respectively Figures C.2 and C.1 as well, showing domain-wide compact cloud structures for all W50 experiments at 6 hours, which break down towards the end of the day.

⁴The enhancement in LWP and A_c at the start of the day is reflected in the slightly brighter domain in Figures C.2 and C.1

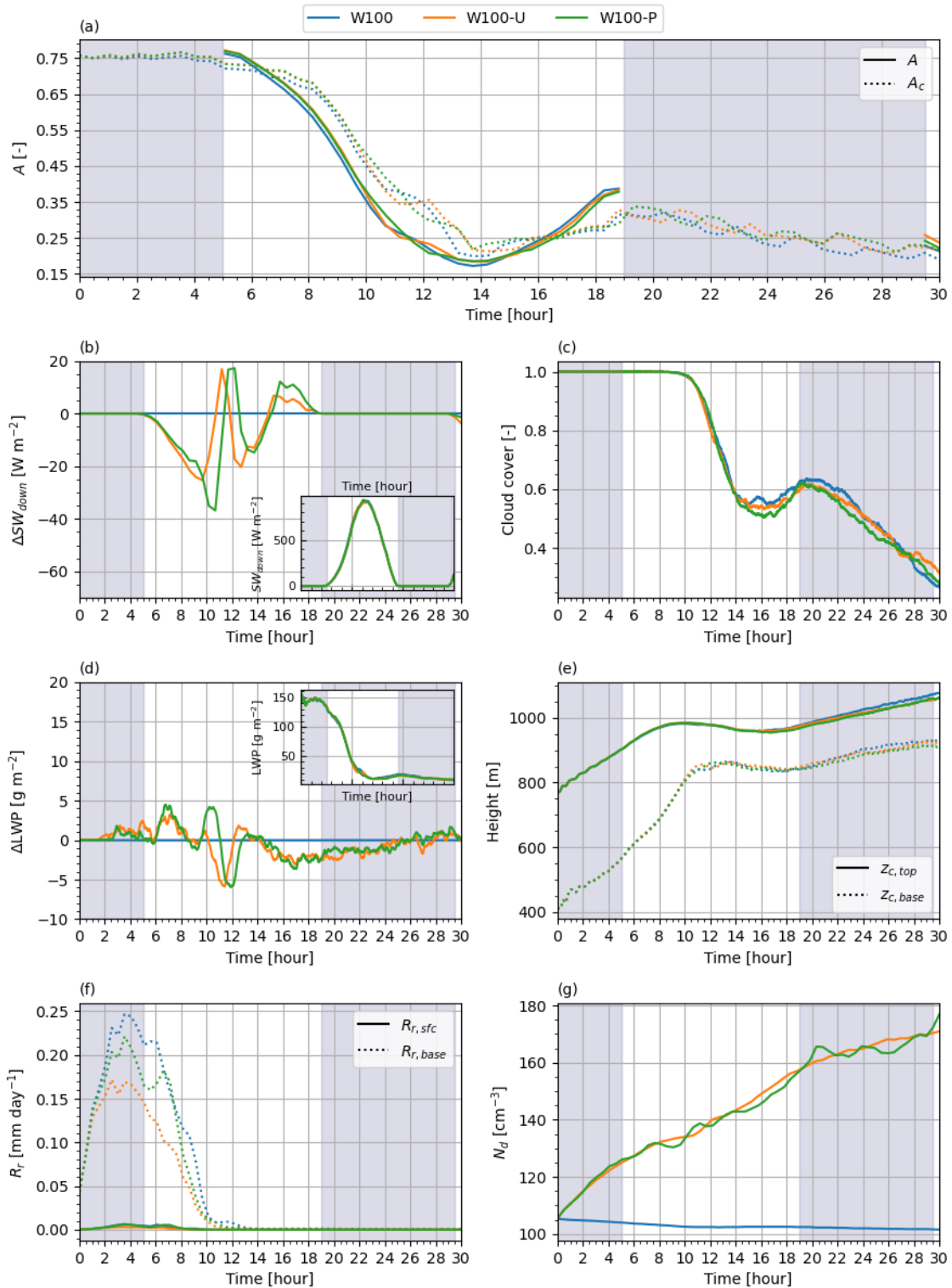


Figure 5.2: Time series of the RF02 case with an average maritime aerosol number concentration (100 cm^{-3}), showing the domain-averaged values of: (a) effective albedo A and cloud albedo A_c , (b) difference in downwelling shortwave radiation at the domain surface with respect to the base case without aerosol source (here W100) $\Delta SW_{d,sfc}$, (c) cloud cover, (d) difference in liquid water path with respect to the base case ΔLWP , (e) cloud-top $Z_{c,top}$ and cloud-base $Z_{c,base}$, (f) cloud-base precipitation rate $R_{r,base}$ and surface precipitation rate $R_{r,sfc}$ and (g) average in-cloud cloud droplet number concentration N_d . The blue line indicates the base case, the orange line represents the case with a uniform aerosol source, and green represents the case with an aerosol point source. Subfigures (b) and (d) include an additional plot showing the trend of respectively $SW_{d,sfc}$ and LWP to indicate the order of magnitude of the parameters and their evolution in time. Shading between 0 and 5 hours and between 19 and 29.5 hours represents nighttime during the simulations.

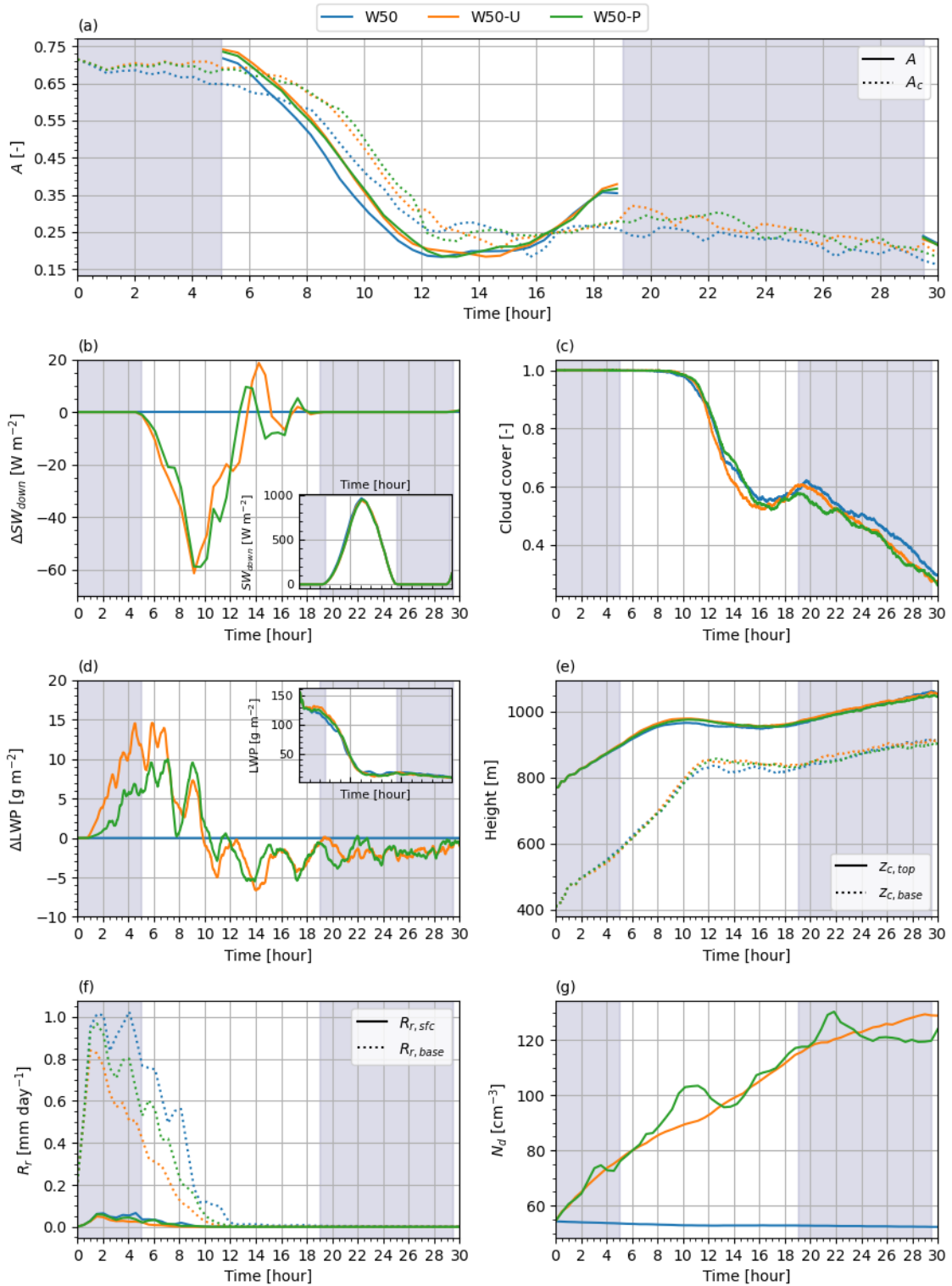


Figure 5.3: Same as Figure 5.2, but for a clean maritime aerosol number concentration ($N_{ae,kg} = 50 \text{ cm}^{-3}$).

variance in the vertical velocity near cloud-base during the same time-interval (see Figure C.4). Decoupling has a thinning effect on the cloud, as this reduces the moisture supply from the surface into the cloud layer. The subfigures in Figure 5.2(d) and 5.3(d) show a slight LWP enhancement in the afternoon until the start of the second night. This suggests that the cloud is not fully decoupled, and moisture is supplied from the sub-cloud layer.

Similar results are shown for the W50 simulations in Figure 5.3(f). Here, the precipitation rates are still relatively small, but considerably higher than for W100. This is a consequence of the lower N_{ae} and corresponding N_d values, which enable the cloud droplets to grow larger and form rain droplets more quickly upon collision of these cloud droplets. The largest precipitation suppression is again generated by the uniform spraying strategy. Decoupling of the cloud layer is also indicated here in the difference in cloud-base and surface precipitation rate. The buoyancy fluxes and vertical velocity variances of the W50 simulations show similar characteristics related to decoupling as the W100 experiments.

The average cloud droplet number concentration N_d in the cloud layer in Figures 5.2(g) and 5.3(g) shows the expected approximate linear increase in time due to the aerosol injections. The role-off towards the end of the simulation and the slight reduction in the base cases W100 and W50 can be explained by the increase in cloud-layer height and consequently the reduction in air density, reducing the number of aerosols per cubic metre of air. The N_d for the point source experiments shows more variance in time, which can be attributed to the more concentrated initial aerosol distribution upon injection⁵. Transport into the cloud layer can be either more or less effective depending on the local vertical velocity. Although it is not shown in these figures, it must be noted that N_d is not uniform throughout the cloud layer due to the surface aerosol sources. As the aerosols enter the cloud from below, the concentrations are largest at the cloud-base and diminish towards the cloud-top. However, the deviations from the mean values shown in the figures are minor and in the order of minus a few percent below and plus a few tenths of percent above the mean.

The efficacy of MCB in terms of LWP retention and A_c enhancement is smaller for the two considered cases compared to the results of WANG11. The most dominant factor to which this can be attributed is the difference in generated surface precipitation. This is in the order of 1 mm day^{-1} in WANG11 and significantly larger than the DALES-modelled rates. The loss of liquid water is coupled to the loss of aerosols in the cloud layer in the microphysics scheme of WANG11, both of which cause A_c to diminish. The positive feedback between aerosol reduction and precipitation amplifies rain production. Our simulations do not include the coupling between precipitation and aerosol concentration, and consequently, this runaway process is not included. The generated precipitation in WANG11 is larger, so suppressing the precipitation by replenishing the aerosol concentration with the surface sources has a larger effect on the LWP. This is most evident in their W100-U case, in which the precipitation is completely suppressed, and the cloud fraction is maintained at unity.

The persistent precipitation in WANG11 causes the cloud-top to lower as well. The precipitation rates of the base cases in our simulations are low, and therefore, the cloud-top does not lower but instead rises due to entrainment at the cloud-top. The combination of generally lower precipitation rate and higher entrainment rate generated by DALES compared to the other LES models, as shown in Section 4.3, causes the cloud-tops of all our W100 and W50 cases to rise with comparable speed to the W100-U case modelled in WANG11. Therefore, cloud seeding does not affect the deepening of the cloud in our simulations, as seen in the simulation results of WANG11.

For the cases in WANG11, in which precipitation is not completely suppressed, N_d is significantly less than in our simulations. The higher N_d in our simulations causes the cloud droplets to be smaller, which causes entrainment to increase through the evaporation-entrainment and sedimentation-entrainment effect and the LWP to be further reduced.

⁵This is evident in the bottom row illustrations in Figure C.3, which show high local concentrations of aerosols near the aerosol point source (top left corner of the domain).

Even though the differences in outcomes are mainly due to the differences in generated precipitation rates, both our simulations and the simulations of WANG11 show that for seeding W100 the uniform spraying strategy is most effective to reduce the incoming solar radiation at the Earth's surface. For W50, the more locally concentrated point source strategy is most effective.

5.3.2. LWP Budget Analysis

Figures 5.4 and 5.5 show the time evolutions of the total LWP tendency and the five contributing factors to this tendency, as earlier explained in Section 5.1.2, for respectively the W100 and W50 simulations. It is important to note beforehand that the calculated tendencies in this thesis, using the budget equations of Van der Dussen et al. (2014), are an approximation of the true LWP tendencies of the simulations. This is reflected by the differences in the solid 'budget' lines and dotted 'true' lines in Figures 5.4(a) and 5.5(a). The inability of resembling the true LWP tendency results most likely from the broken cloud structure. This makes it difficult to maintain a well-mixed STBL, which is implicitly assumed for the LWP budget analysis. In addition, the contributions to the LWP tendency are sensitive to the cloud-top, cloud-base and inversion height. Not only defining these heights with the available output data can be complex, but the vertical mesh size of 20 m results in the under- and overestimation of the heights and consequently in the budget equations. However, the same calculations for cloud-top, cloud-base and inversion height are applied for each of the simulations such that the results can be compared qualitatively nonetheless.

For the W100 experiments, the LWP budget is mostly determined by the negative effects of entrainment and positive effects of the fluxes near cloud-base and radiation. The effects of precipitation and large-scale subsidence are an order of magnitude smaller than the aforementioned contributions.

It is expected that the negative contribution of entrainment reduces during the day, due to the reduction in the temperature inversion strength. Figure 5.4(b) shows that the entrainment contribution becomes less negative from sunrise until approximately 15 hours. The incoming solar radiation causes radiative cooling at the cloud-top to diminish, which reduces the turbulence in the cloud layer and thereby the entrainment rate. This effect is evident for the contribution of the fluxes near cloud-base as well, which show to contribute the most in the absence of solar radiation and have minimal contribution around noon. Next to the influence of solar radiation, the reduction of the contribution of entrainment can be attributed to the interplay between LWP and w_e . At first, when LWP is relatively high, w_e is sustained or might be amplified by the evaporation-entrainment effect. When LWP strongly reduces, as is seen in Figure 5.2, the difference in q_t and θ_l is diminished as well, limiting the strength of the entrainment contribution.

There are no clear differences in the profiles of entrainment contribution due to aerosol seeding that can be distinguished with certainty. Both for W100-U and W100-P, the entrainment contributions fluctuate marginally above and below the entrainment contribution of the unseeded case W100. The enhancement of N_d does not directly affect w_e , Δq_t , $\Delta \theta_l$ and $h\Gamma_{q_l}$, which control the entrainment contribution, but these parameters are rather modified indirectly through processes such as cloud-base fluxes, precipitation, and radiation. This, in combination with the feedback mechanisms between the process, makes determining what causes the fluctuations too complex with the use of this analysis method alone.

During the first night, the contribution of radiation (shown in Figure 5.4(d)) is approximately constant at around $80 \text{ g m}^{-2} \text{ h}^{-1}$, which is significantly reduced due to the incoming solar

radiation that reduces the net radiative cooling of the cloud layer. The reduction of radiation contribution from the start of the second night onward can be explained by the reduction in cloud cover, such that the overall difference in radiation at cloud-top and cloud-base diminishes. As the effect of N_d enhancement on the cloud albedo is minimal at the start of the second night for the W100 cases, cloud cover shows to be the main cause of the relative differences in radiation contributions between W100, W100-U and W100-P through its effect on the difference in radiation between cloud-top and cloud-base.

The relatively large LWP at the start of the simulations triggers precipitation, resulting in the thinning contribution presented in Figure 5.4(e). The production of precipitation decreases as the cloud's LWP reduces, which causes the precipitation to approach steady-state at $0 \text{ g m}^{-2} \text{ h}^{-1}$ after approximately 13 hours. Precipitation is partially suppressed by the enhancement of N_d , resulting in a reduced thinning effect of precipitation. In agreement with Figure 5.2(f), uniform aerosol injection is most effective in sustaining the cloud's LWP with an approximate maximum difference of $4 \text{ g m}^{-2} \text{ h}^{-1}$ with respect to the unseeded base case. Point source seeding reduces the loss of LWP due to precipitation as well, but due to the more local N_d enhancement, its effect is less pronounced.

The negative contribution of subsidence to the LWP budget is shown in Figure 5.4(f). Due to the rapid cloud thinning, the role of subsidence in the LWP budget diminishes through its dependency on cloud thickness h in Eq. (5.7). Between 14 and 24 hours, the experiments including cloud seeding show a slightly less negative contribution of subsidence, which matches the period of reduced cloud cover compared to the unseeded base case. The reduced cloud cover corresponds to a domain-averaged reduction of q_i^t (liquid water mixing ratio at cloud-top), which affects the subsidence contribution by its dependence on $\Gamma_{q_i} = \frac{q_i^t}{h}$.

Similar trends for the different contributions to the LWP tendency are found for the W50 experiments shown in Figure 5.5, where entrainment, cloud-base fluxes and radiation are again the main contributors to the LWP tendency. The loss of LWP due to precipitation is larger than for the W100 experiments due to the higher precipitation rate for the cleaner environment. As a result of the larger precipitation rate, the absolute effect of precipitation suppression on the LWP budget by the aerosol injection is larger as well, with a maximum difference of around $20 \text{ g m}^{-2} \text{ s}^{-1}$ and $12 \text{ g m}^{-2} \text{ s}^{-1}$ with respect to W50 for W50-U and W50-P, respectively.

The contribution of entrainment is slightly more negative for the seeded cases from before sunrise to about noon, which causes the LWP of W50-U and W50-P in Figure 5.3 to be smaller compared to W50 after the positive effect of precipitation suppression has become minimal. The period of more negative LWP tendency due to entrainment correlates with the period of precipitation suppression. As a consequence of the reduced precipitation, more liquid is available to be evaporated by entrainment, reducing the LWP. The more negative entrainment contribution for the seeded cases diminishes after noon, which may be attributed to the LWP reaching equal levels with respect to W50. Clear evidence of enhanced LWP loss due to reduced droplet size can not be deduced from the results. A potential explanation for this is the relatively low LWP, such that cloud droplets are already of such small size that further reduction due to cloud seeding has minimal effect on the evaporation rate.

The positive effect of precipitation suppression to the LWP is partially compensated by the negative effects on the fluxes near cloud-base and to a lesser extent by the more negative contribution of subsidence within the same period. The smaller contribution of the cloud-base fluxes is surprising, as one might expect that the suppression of precipitation reduces evaporative cooling of the sub-cloud layer and warming of the cloud layer, which results in the enhancement of turbulence. However, next to its effect on the sub-cloud turbulence, precip-

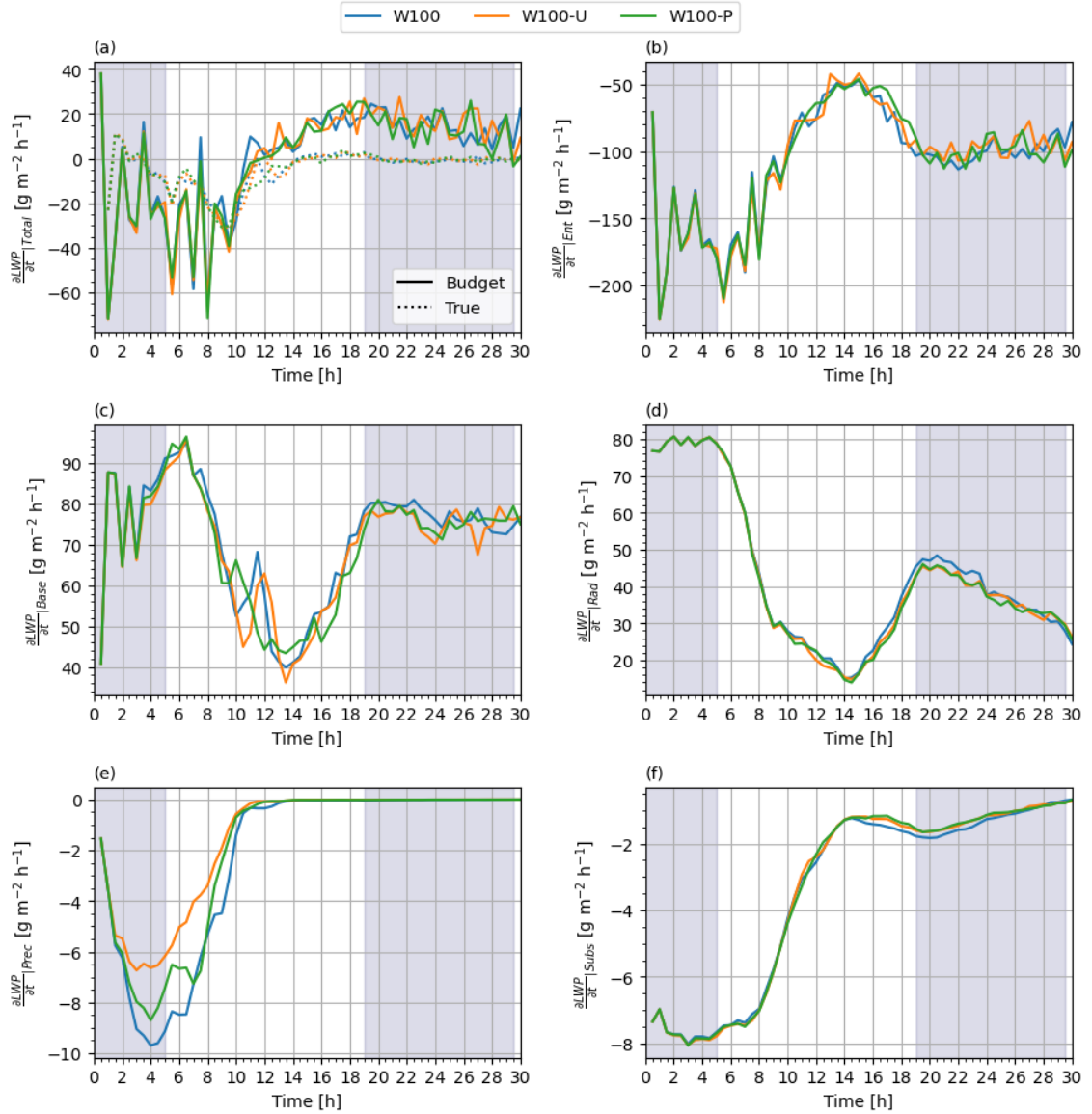


Figure 5.4: Time series of the different contributions to the tendencies in LWP for the RF02 case with an average maritime aerosol number concentration (100 cm^{-3}), showing: (a) the total tendency determined with the budget equations of Van der Dussen et al. (2014) (solid lines) and directly obtained from the output (dotted), and the tendency contributions of (b) entrainment, (c) turbulent fluxes in q_t and θ_l near the cloud-base, (d) difference in net radiation at cloud-top and cloud-base, (e) difference in precipitation rate between cloud-top and cloud-base and (f) subsidence. The blue line indicates the base case using no aerosol source, the orange line represents the case with a uniform aerosol source, and green represents the case with an aerosol point source. Shading between 0 and 5 hours and between 19 and 19.5 hours represents nighttime during the simulations.

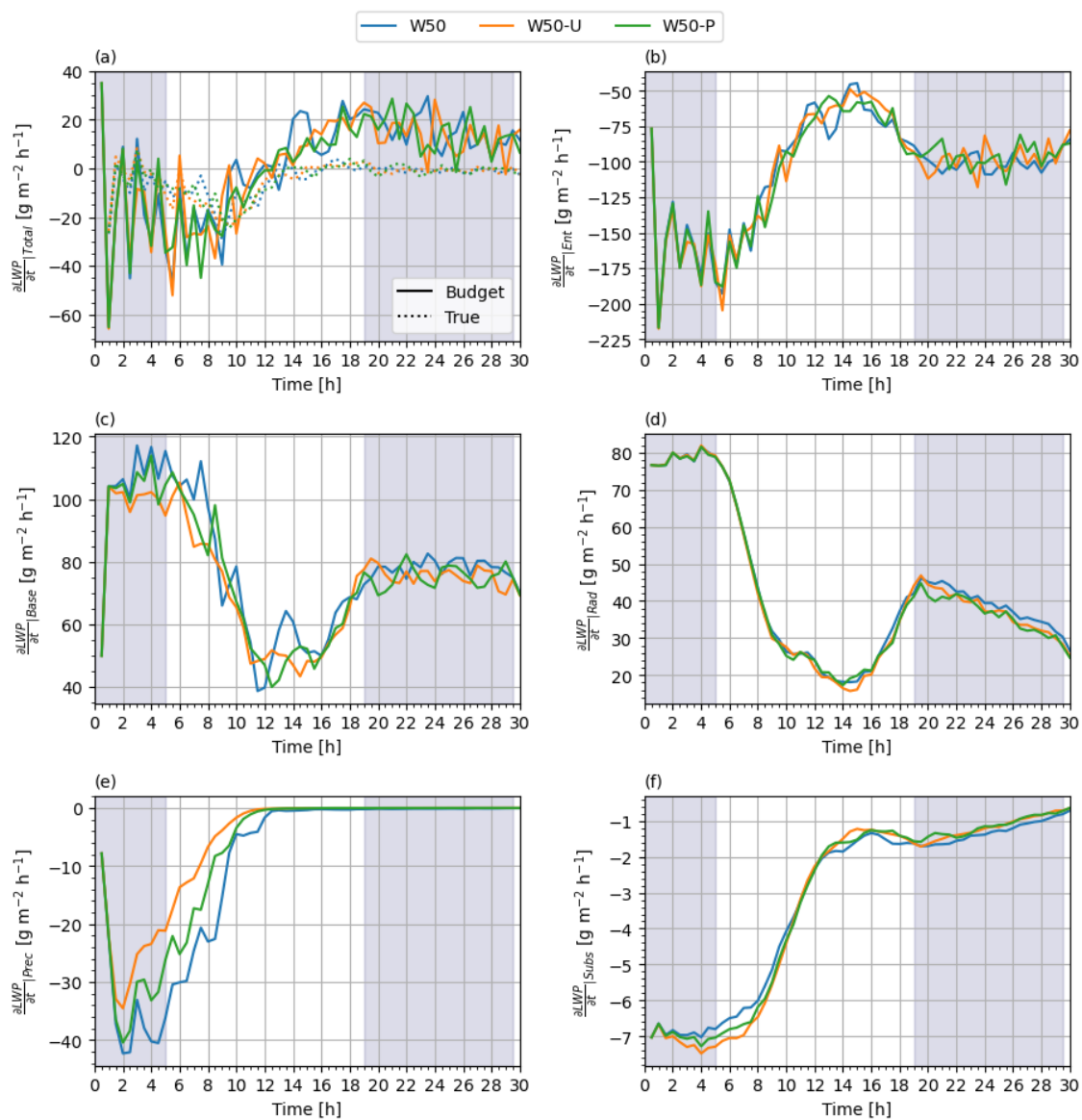


Figure 5.5: Same as Figure 5.4, but for a clean maritime aerosol number concentration ($N_{ae,kg} = 50 \text{ cm}^{-3}$).

itation redistributes the water content in the sub-cloud layer as well, which is then available to be transported back into the cloud through turbulent eddies. Consequently, a decreased precipitation rate due to N_d enhancement reduces q_t , diminishing the contribution of the turbulent fluxes at cloud base to the LWP tendency. For the particular simulations of W50-U and W50-P, the effect of relative sub-cloud layer warming with respect to W50 has less effect on the turbulent fluxes at cloud-base than the changes in sub-cloud q_t , resulting in a net reduced contribution of cloud-base fluxes due to cloud seeding.

For the W100 experiments, it was stated that differences in cloud cover mainly cause the difference in the radiation contribution for the seeded and unseeded experiments. For the W50 experiments, however, the difference in cloud cover is approximately zero and the differences in cloud albedo are relatively large between 5 and 10 hours. It is expected that the higher cloud albedo of the seeded experiments increases the contribution of radiation through enhanced shortwave radiation reflection at the cloud-top, which is not evident from Figure 5.5(d). This can be explained by the effect of the increase in cloud-top height of W50-U and W50-P with respect to that of W50, which causes the radiative cooling at the cloud-top to be smaller and hence compensates the enhanced shortwave reflection.

The larger q_i^t , as a consequence of the reduced precipitation rate due to the cloud seeding, cause the more negative contribution of subsidence before noon. The differences after noon are related to the differences in cloud thickness h among the W50 experiments.

5.3.3. Summary

To summarise the most important findings for the experiments of the wet stratocumulus-topped boundary layer (RF02) with average and clean pollution levels, as presented in Figures 5.2, 5.3, 5.4 and 5.5:

- Seeding the RF02 case with clean pollution levels generates a mean reduction in solar radiation reaching the surface of about half of the objective value of 21.1 W m^{-2} . For the RF02 case with average pollution levels, this diminishes to a reduction of about a sixth of 21.1 W m^{-2} , due to the relatively smaller increase in aerosol number concentration.
- During sunrise and sunset, an increase in the liquid water path is more effective to increase the effective cloud albedo than an increase in the cloud droplet number concentration.
- For the RF02 cases with average pollution levels, the uniform spraying strategy (W100-U) generates more reduction in solar radiation reaching the surface compared to the point source spraying strategy (W100-P), due to a temporary higher cloud fraction. For the RF02 cases with clean pollution levels, the point source spraying strategy (W50-P) is slightly more effective in reducing solar radiation reaching the surface than the uniform spraying strategy (W50-U). This is in agreement with the findings of WANG11.
- Shown for the RF02 cases with average pollution levels (W100), a higher cloud cover causes an increase in the radiation contribution to the liquid water path, as it increases the difference in radiation between the cloud-top and cloud-base.
- Shown for the RF02 cases with clean pollution levels (W50), the radiation contribution to the liquid water path reduces as the cloud-top rises, due to the reduced cloud-top radiative cooling.
- The increase in cloud droplet number concentration partially suppresses precipitation and increases the cloud's liquid water path. The larger precipitation rate for the RF02

case with clean aerosol pollution levels (W50) causes a larger suppression of precipitation due to aerosol injection compared to the case with average aerosol pollution levels (W100).

- Precipitation suppression is most effective using the uniform spraying strategy for both the RF02 cases with average (W100-U) and clean (W50-U) pollution levels, due to the larger covered domain of the enhancement in cloud droplet number concentration.
- The positive effect of precipitation suppression to the liquid water path is compensated by a reduction in the contributions of entrainment and cloud-base turbulent fluxes to the liquid water path, because more liquid water is available for evaporation near the cloud-top and less water is available below the cloud-base to be transported into the cloud-layer.
- The smaller increase in liquid water path and cloud albedo found in our simulations compared to those found by WANG11 is most likely due to the difference in generated precipitation rate, which can then be (partially) suppressed by the cloud injection of aerosols.

5.4. Results:Dry STBL with Average and Clean Pollution Levels

In this section, we present and discuss the results of the different spraying strategies on the cloud properties and physical processes in a drier and warmer STBL, the RF01 case. The considered cases have again average and clean pollution levels (initial $N_{ae,kg}$ of 100 cm^{-3} and 50 cm^{-3}), which are abbreviated to D100 and D50, respectively.

5.4.1. Reflection Enhancement

The initial value of A_c of the D100 cases shown in Figure 5.6(a) is about 0.3 lower than initially obtained for their moister counterparts of the W100 cases, due to the lower initial LWP. The effective albedo at the start of the day is only reduced by approximately 0.12, resulting from the large solar zenith angle. The minima of A are approximately the same with respect to the values found for the W100 cases. Both A and A_c of the seeded cases are consistently above the values of the base case, showing the largest increases from late afternoon (about 16 hours) towards the night. Due to the consistency in effective albedo enhancement, the resulting mean differences $\overline{\Delta SW_{d,sfc}}$ are -4.3 W m^{-2} and -6.3 W m^{-2} for the uniform and point source seeding strategy, respectively (see Table 5.3).

Similar results can be deduced from Figure 5.7(a) for the clean maritime pollution levels of the D50 cases. Compared to the moister W50 cases, the values of A and A_c are initially 0.35 and 0.14 lower, respectively, due to the lower initial LWP. Throughout the simulations, both A and A_c of the seeded cases are consistently above the unseeded base case, with the largest increases starting at 16 hours. For W50-U, the resulting mean difference $\overline{\Delta SW_{d,sfc}}$ is -9.6 W m^{-2} , and for W50-P, it is -8.1 W m^{-2} .

The daytime cloud cover and ΔLWP in Figure 5.6(c) and (d) show slight reductions for the uniformly seeded simulation D100-U compared to the base case D100, whereas for the point source simulation D100-P the cloud cover is increased and ΔLWP is approximately unchanged. This indicates that for D100-U, the enhanced N_d causes minimal cloud thinning, whose effect on A and A_c is more than compensated by its cloud brightening effect of reduced aerosol size. For D100-P, the increased cloud cover in combination with unchanged LWP suggests that the LWP reduction is more localised, due to the more concentrated aerosol injection, leaving a domain-averaged cloud cover. Together with the increased N_d , this adds to more reflected solar radiation than for D100 and D100-U.

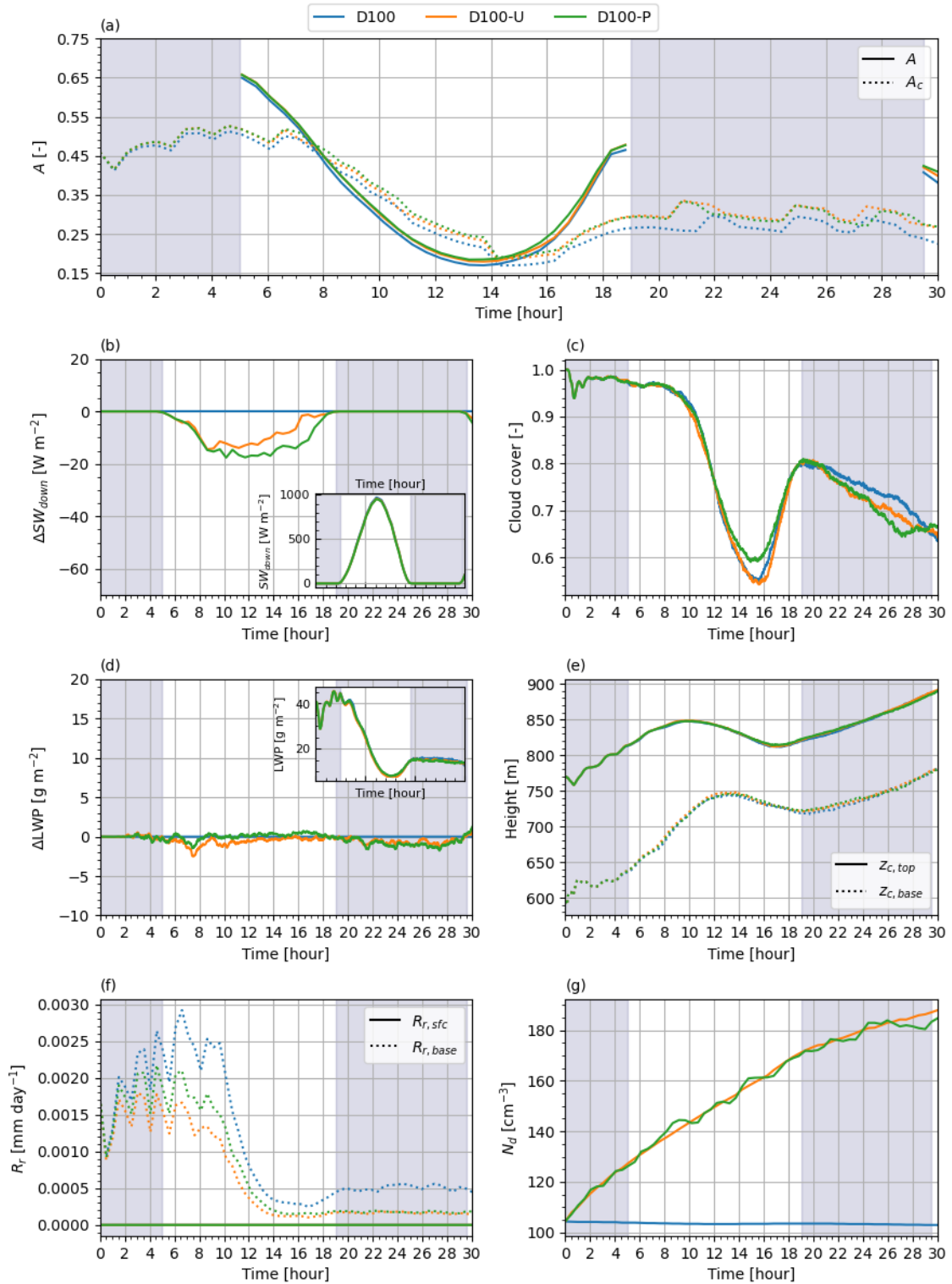


Figure 5.6: Same as Figure 5.2, but for the drier and warmer RF01 case, with an average maritime aerosol number concentration ($N_{ae,kg} = 100 \text{ cm}^{-3}$).

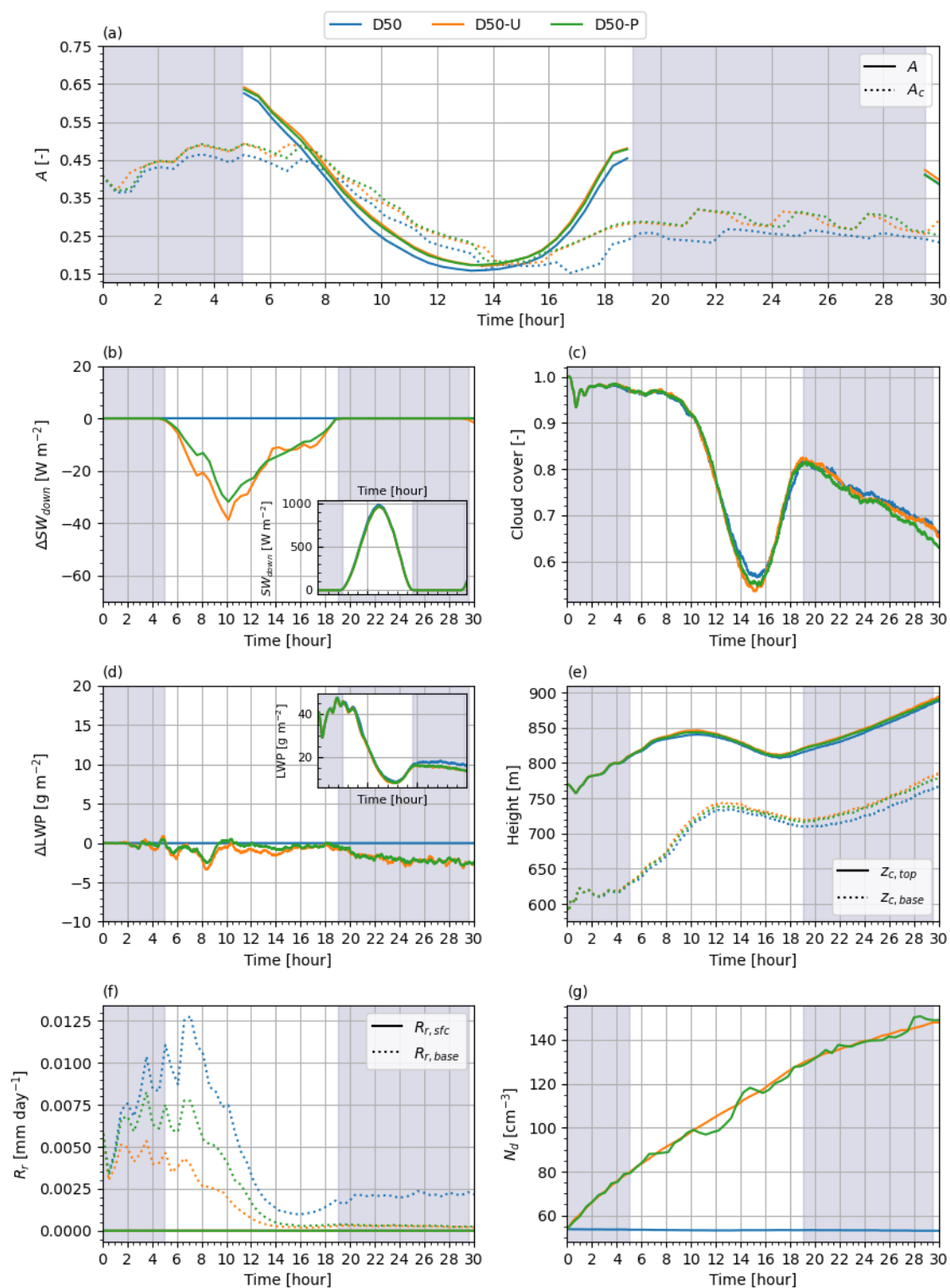


Figure 5.7: Same as Figure 5.2, but for the drier and warmer RF01 case, with a polluted maritime aerosol number concentration ($N_{ae,kg} = 50 \text{ cm}^{-3}$).

Although the cloud cover is slightly larger and ΔLWP is slightly less negative for D50-P compared to D50-U between sunrise and 13 hours (see Figure 5.7(c) and (d)), the reduction in $SW_{d,sfc}$ is larger for D50-U than for D50-P. This can be attributed to the more evenly distributed cloud droplet number concentration enhancement for D50-U⁶, which has a higher positive effect on the cloud's reflectivity as a whole compared to a more local reflection enhancement caused by the point source strategy.

The moderate reduction in LWP with respect to the base case values is seen for the seeded D50 cases in Figure 5.7(d) as well. For both D50-U and D50-P, this reduces the cloud cover between about 13 and 16 hours. Although LWP and cloud cover loss diminishes the A and A_c , the strong increase in N_d makes up for this loss, attributing to the net increase in A and A_c . This indicates that for both D100 and D50, which are nearly non-precipitating dry STBLs, the effect of aerosol seeding is dominated by the first indirect aerosol effect. This contrasts with the findings of WANG11 for lightly precipitating STBLs, in which the second indirect aerosol effect dominates the effect of cloud seeding.

Due to the warmer and drier STBL, the height at which condensation starts is higher than in the cooler and moister STBL. The result is a higher cloud-base and thinner cloud for the D100 cases, as shown in Figure 5.6(e), compared to the W100 cases. Similar but less drastic than for the W100 cases, the evaporation of liquid water by entrained air drives the loss of LWP and causes the cloud-top to rise. The cloud-base rises due to the warming of the cloud layer until approximately 10 hours and 12 hours into the simulation, respectively. Hereafter, the cloud-top and -base slightly lower until the start of the second night, due to the reduction of entrainment-driven evaporation for the low LWP levels and the more dominant effect of subsidence. Due to the slower rise of the cloud-top height, the mean N_d before the start of the second night (at 19 hours) is higher in the seeded dry experiments than in the seeded wet experiments, with a maximum N_d of approximately 170 cm^{-3} compared to nearly 160 cm^{-3} for the dry and wet experiments, respectively. Consequently, this contributes to the higher $\overline{\Delta SW_{d,sfc}}$ found for the seeded D100 experiments compared to the W100 experiments.

The cloud-top and cloud-base height show a similar trend for the D50 simulations. The seeded experiments show a slightly faster rise than the unseeded base case, resulting in a maximum difference in cloud thickness of a few tens of metres. What causes the faster rise will be determined in Section 5.4.2. Similar to the seeded D100 experiments, the N_d found at the end of the day of the seeded D50 experiments is approximately 130 cm^{-3} . This is larger than found for the seeded W50 experiments with approximately 115 cm^{-3} , due to the lower cloud layer of the D50 experiments. However, as this difference is relatively small and because the LWP of the seeded W50 experiments is slightly larger than for D50, the difference in the first and second indirect aerosol effect balance out and the resulting $\overline{\Delta SW_{d,sfc}}$ are of similar magnitude.

The precipitation rates at cloud-base in Figure 5.6(f) and 5.7(f) are about a tenth of the already low rates of the W100 and W50 experiments, and the raindrops are completely evaporated before reaching the surface. Point source seeding shows to be more effective in suppressing the light rain-out compared to uniform seeding. As cloud-base precipitation is relatively small, the evaporation in the sub-cloud layer is small as well, and its effect on decoupling is minimal. This is validated by their vertical buoyancy and vertical velocity profiles shown in Figure C.5, showing no negative buoyancy and minimum vertical velocity variance near cloud-base.

⁶The more evenly distributed cloud droplet number concentration enhancement can be deduced from Figure C.3 (although these results correspond to the W50 experiments), which shows more local variations in the aerosol number concentration for the point source strategy (bottom row illustrations) compared to the relatively uniform distribution of aerosols for the uniform source strategy (middle row illustrations).

WANG11 modelled the D100 experiments as well. In agreement with our simulations, they found a small reduction in LWP due to cloud seeding and similar time-averaged LWP. WANG11 show that the fraction of activated aerosols is limited by the low supersaturation level due to the small LWP. Consequently, N_d does not longer increase with the number of available aerosols. This causes their N_d for the unseeded base case to be approximately half of our value. The increase in N_d of the seeded experiments is significantly smaller than in the simulations presented here ($\sim 30 \text{ cm}^{-3}$ vs $\sim 50 \text{ cm}^{-3}$) as well, which causes their enhancement of A_c to be approximately half of our values.

The differences in retrieved N_d of the simulations of WANG11 and our simulations stress the importance of an aerosol activation scheme that interacts with microphysical parameters such as supersaturation once more. Our modified DALES model implicitly assumes the reduction of aerosol activation due to its reducing effect on the supersaturation by the roll-off for higher aerosol concentrations. However, this parameterisation is constructed from the observations during which LWP was in the order of magnitude of the values found in the first night of the simulations when supersaturated water is relatively abundant. For much lower LWP, as found in our simulations during daytime, the effect of activated aerosols on the supersaturation is much larger and significantly fewer aerosols are activated in reality than in our parameterisation. The result is an overestimation in N_d and consequently in A and A_c .

5.4.2. LWP Budget Analysis

Figure 5.8 shows the contributions of the different cloud processes to the LWP tendency and the total LWP tendency for the D100 experiments. Among the experiments, the profiles show strong similarities. This can be attributed to the minimal contribution of precipitation and consequently to precipitation suppression by N_d enhancement. This is reflected in the nearly equal contributions of the cloud-base surface fluxes. Especially during the first night, the cloud-base fluxes contributions are significantly smaller than those of the W100 experiments. This is caused by the drier STBL and the higher initial cloud-base height.

The deviating results of the contributions of radiation and subsidence during the second night in Figures 5.8(d) and (f) are correlated with the differences in cloud cover as shown in Figure 5.6(c), which is also evident from the W100 and W50 experiments. In addition, the contribution of the turbulent fluxes and entrainment are correlated with cloud cover as well. The more extensive cloud cover for D100 compared to D100-U and D100-P during the second night generates more radiative cooling at the cloud-top, inducing more turbulence in the cloud layer and larger turbulent fluxes near the cloud-base, which results in a more negative contribution of entrainment and an increase in the positive contribution of cloud-base turbulent fluxes.

The LWP tendency contributions of the D50 experiments are similar to those found for the D100 experiments. The contributions of precipitation are slightly larger, but still of negligible magnitude. The correlation between cloud cover and contribution of radiation is evident here as well, showing a diminished positive LWP tendency between 12 and 16 hours and during the second night for the seeded experiments D50-U and D50-P with respect to D50.

The differences in the entrainment rate between seeded and unseeded experiments, which were evident for the W50 experiments, are only shortly evident between 6 and 8 hours for the D50 experiments. The general absence of increased loss of LWP due to entrainment is because the LWP is not enhanced (such as for the seeded W50 experiments). Therefore, this does not affect Δq_t and $\Delta \theta_t$ of Eq. (5.3). The reducing effect of enhanced N_d on the droplet size does not seem to enhance the LWP loss due to entrainment significantly. The lack of enhanced LWP loss can be attributed to the limited liquid water available near the cloud-top

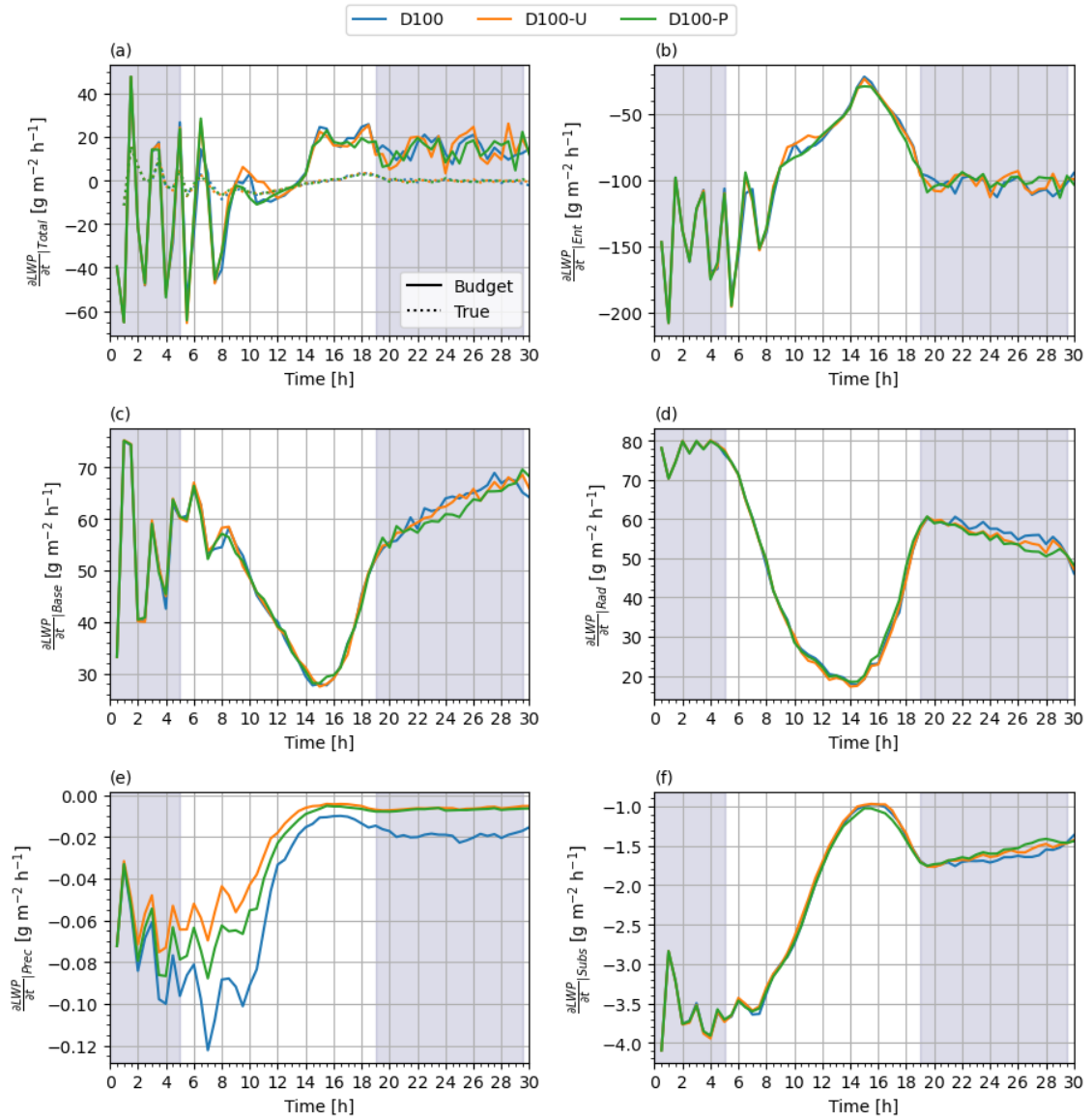


Figure 5.8: Same as Figure 5.4, but for the drier and warmer RF01 case, with an average maritime aerosol number concentration ($N_{ae,kg} = 100 \text{ cm}^{-3}$).

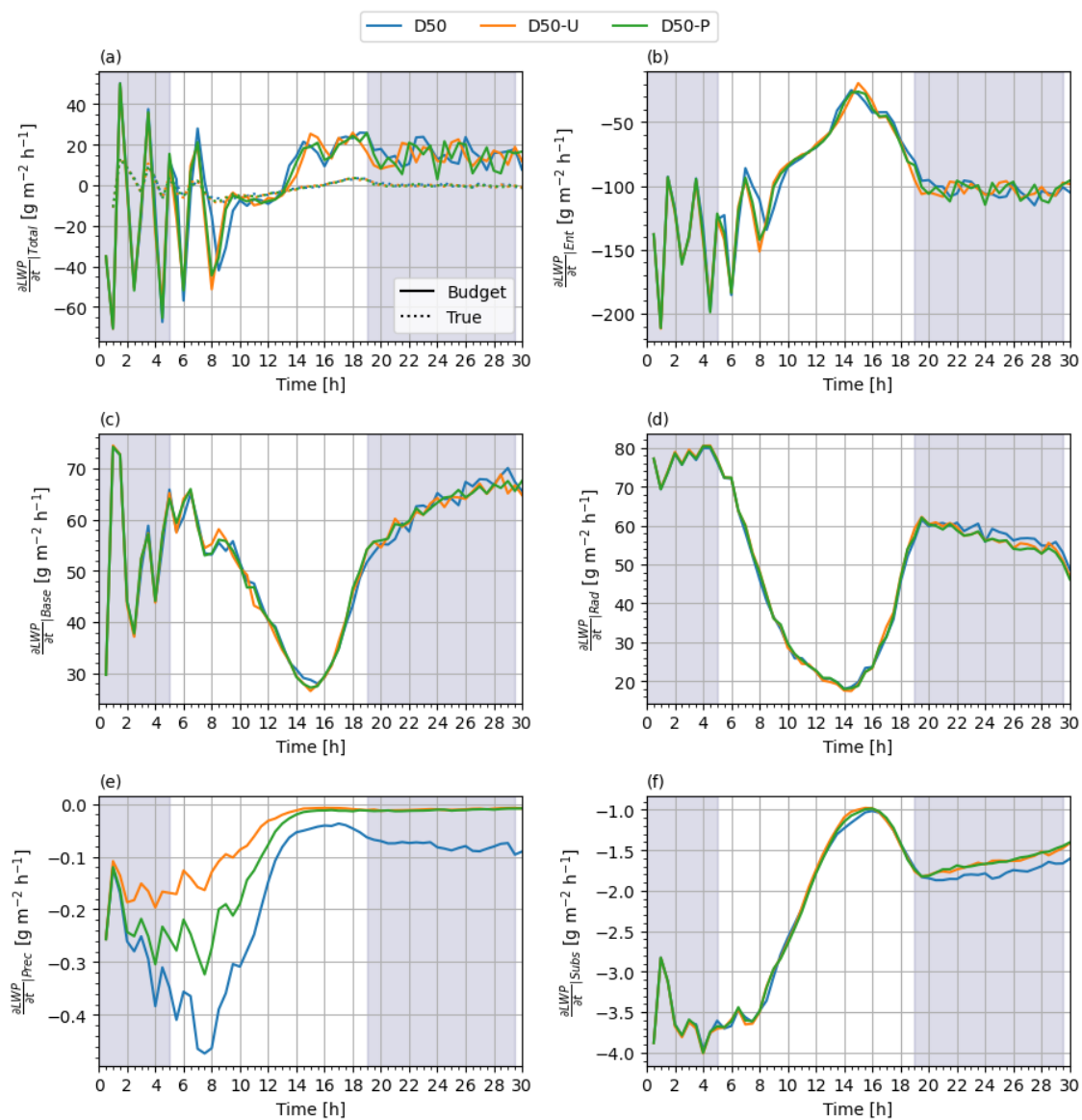


Figure 5.9: Same as Figure 5.4, but for the drier and warmer RF01 case, with a polluted maritime aerosol number concentration ($N_{ae,kg} = 50 \text{ cm}^{-3}$).

to be further decreased due to its smaller droplet size.

The small relative difference of the contribution of cloud-base fluxes can be attributed to the combination of the differences in cloud-base height and cloud cover, causing the cloud-base contributions of the seeded experiments D50-U and D50-P to be slightly below that of the unseeded experiment D50 during the second night.

The effect of the smaller cloud thickness in D50-U and D50-P relative to that of D50 is reflected in the less negative contribution by subsidence.

The slightly faster rise in cloud-top and cloud-base height, shown in Figure 5.7(e), can be explained by the changes in the contributions of entrainment and turbulent fluxes near the cloud base. The difference in cloud-top height is generated around 8 hours, which corresponds to the moment of pronounced difference in the entrainment contribution of the seeded experiments with respect to D50. After this peak in entrainment contribution, periods of increased and reduced contributions are approximately balanced, such that the difference in cloud-top does not further increase. The slightly lowered contribution of cloud-base turbulent fluxes reduces water replenishment at the cloud-base, which thins the cloud from below.

5.4.3. Summary

The most important findings for the experiments of the dry and warm stratocumulus-topped boundary layer (RF01) with average and clean pollution levels, as presented in Figures 5.6, 5.7, 5.8 and 5.9, are summarised as follows:

- By obtaining a reduction of approximately a fifth of the objective value of 21.1 W m^{-2} , seeding the RF01 case with average pollution levels (D100) is slightly more effective in reducing the mean solar radiation reaching the surface than for the RF02 case with average pollution levels (W100), but is less effective than seeding stratocumulus-topped boundary layers with clean pollution levels (D50 and W50).
- Seeding the RF01 case with clean pollution levels (D50) is approximately as effective in reducing the mean solar radiation reaching the surface as seeding the moister RF02 case with clean pollution levels (W50).
- For both the RF01 cases with average and clean pollution levels (D100 and D50, respectively), the enhanced radiation reflection is caused by the first indirect aerosol effect. For the W100 and W50 experiments, this is due to a combination of the first and second indirect aerosol effects.
- For the RF01 case with average pollution levels (D100), seeding with the point source strategy causes a more localised cloud break-up. A higher cloud cover is maintained, making it a more effective strategy in enhancing the reflection of solar radiation compared to the uniform source strategy.
- As the difference in cloud cover and liquid water path between the uniform spraying strategy and point source strategy is minimal for the RF01 cases with clean pollution levels (D50), the more evenly distributed cloud droplet number concentration enhancement by the uniform spraying strategy generates more solar radiation reflection than the point source strategy.
- For both the RF01 cases with average and clean pollution levels (D100 and D50, respectively), the differences in liquid water path are small between the seeded and unseeded experiments due to the minimal precipitation rate in all experiments.

- Similar to the moister RF02 cases, the positive correlation between cloud cover and radiation contribution to the liquid water path is found for the RF01 experiments as well.
- The RF01 cases with average pollution conditions (D100) show a positive correlation of cloud cover with both the entrainment rate (causing a decrease in the liquid water path) and the turbulent fluxes near the cloud-base (causing an increase in the liquid water path).
- The increase in cloud droplet number concentration by cloud seeding is most likely over-estimated because the effect of the limited supersaturation is not taken into account in our parameterisation of aerosol activation, which causes our modelled cloud albedo to be about twice as high as the cloud albedo modelled by WANG11 for the RF01 case with average pollution levels (D100).

5.5. Results: Wet and Dry STBL with High Pollution Levels

This section treats the W200 and D200 cases, which resemble the wet and dry STBLs, respectively, with relatively high levels of aerosol pollution ($N_{ae,kg} = 200 \text{ cm}^{-3}$). Because the experiments show similar trends in Figures 5.10 and 5.11 with respect to the figures discussed earlier, the results will be discussed briefly, focusing on the differences compared to earlier findings.

5.5.1. Reflection Enhancement

Compared to the average and clean maritime pollution levels, seeding the W200 and D200 cases is found to be least effective to enhance the cloud reflectivity, as can be seen in Table 5.4. Uniform aerosol seeding results in a $\Delta \overline{SW}_{d,sfc}$ of -0.5 and -2.9 W m^{-2} for respectively W200-U and D200-U. For the experiment W200-P, the mean downwelling shortwave radiation at the surface is even increased by 0.6 W m^{-2} , due to the loss of LWP and cloud cover compared to the base case W200 at times when the solar zenith angle is largest (see Figure 5.10(c) and (d)). For the base case D200, the cloud cover shows a dip around 15 hours compared to the seeded experiments D200-U and D200-P. As the difference in LWP between the experiments is negligible around that time, the D200-U and D200-P have a slightly thinner cloud layer than D200. The reduction in $\Delta \overline{SW}_{d,sfc}$ of -1.2 W m^{-2} for D200-P is relatively small compared to the results of the clean and average polluted environments, which have a $\Delta \overline{SW}_{d,sfc}$ around -9 W m^{-2} . Similar to what is found for the D50 experiments, the difference in $\Delta \overline{SW}_{d,sfc}$ between D200-U and D200-P can be attributed to the more evenly distributed N_d enhancement of the D200-U experiment, while the LWP and cloud cover remain approximately equal throughout the simulation.

The minor effects of the cloud seeding on both A and A_c can be explained by the parameterisation equation for aerosol activation, Eq. (3.1). When comparing the enhancement of N_d in Figures 5.10(g) and 5.11(g) with their less polluted equivalents (the W100 and D100 experiments, respectively), it is shown that N_d increases less quickly for the seeded W200 and D200 experiments, although an equal surface spraying rate is applied. Eq. (3.1) prescribes that increasingly more aerosols are required to increase N_d by the same amount. The result is an increase in N_d between the start and end of the day of approximately 30 cm^{-3} instead of nearly 25 cm^{-3} for the seeded W100 simulations and 45 vs 30 cm^{-3} for the seeded D100 simulations. As mentioned earlier, the loss of LWP during daytime of the W200-U and W200-P adds to the diminished effective albedo enhancement.

The effect of cloud seeding on cloud albedo for the W200 cases showed to be minimal in the study of WANG11 as well. In WANG11, the high aerosol number concentration suppresses

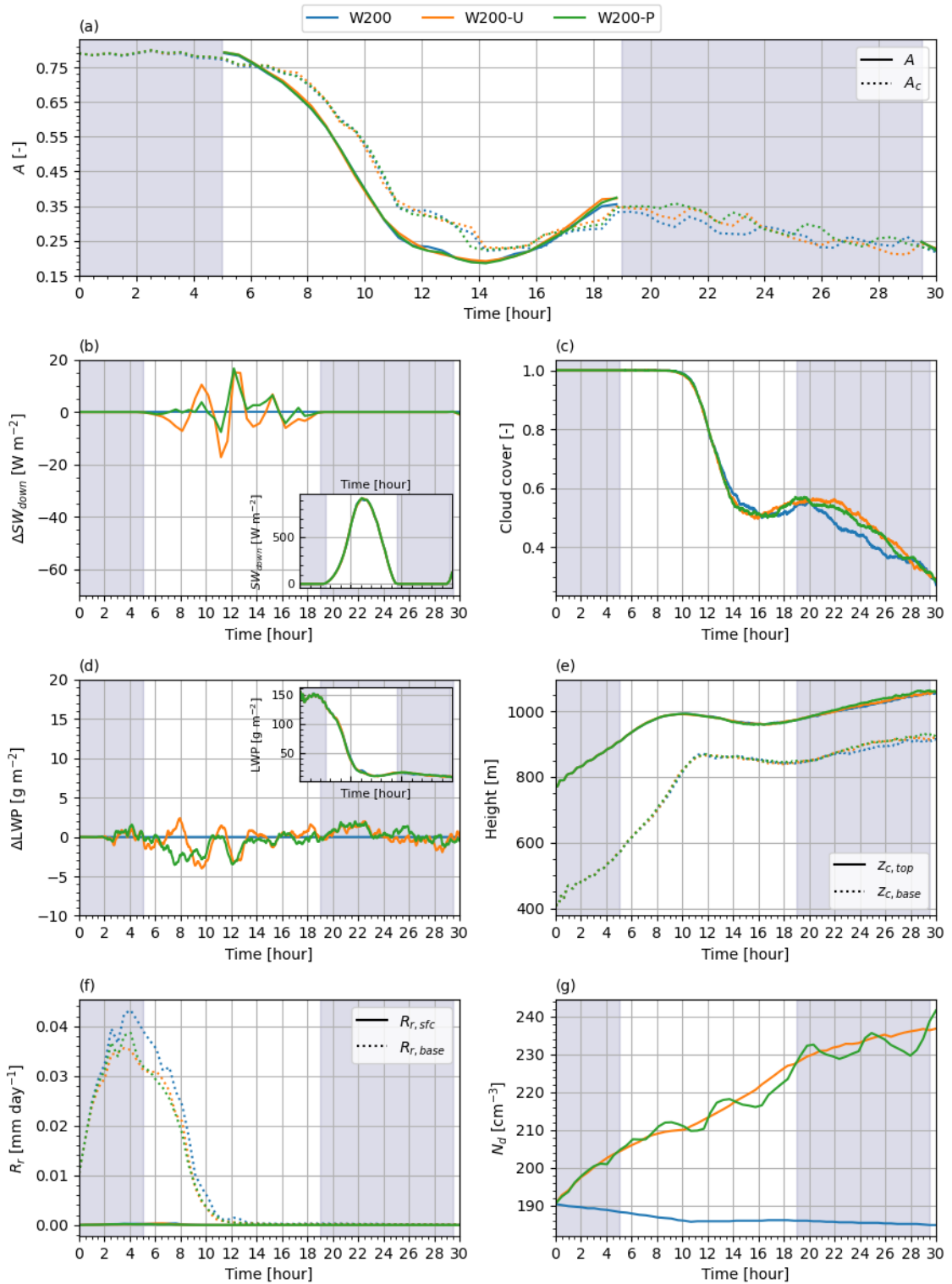


Figure 5.10: Same as Figure 5.2, but with a polluted maritime aerosol number concentration ($N_{ae,kg} = 200 \text{ cm}^{-3}$).

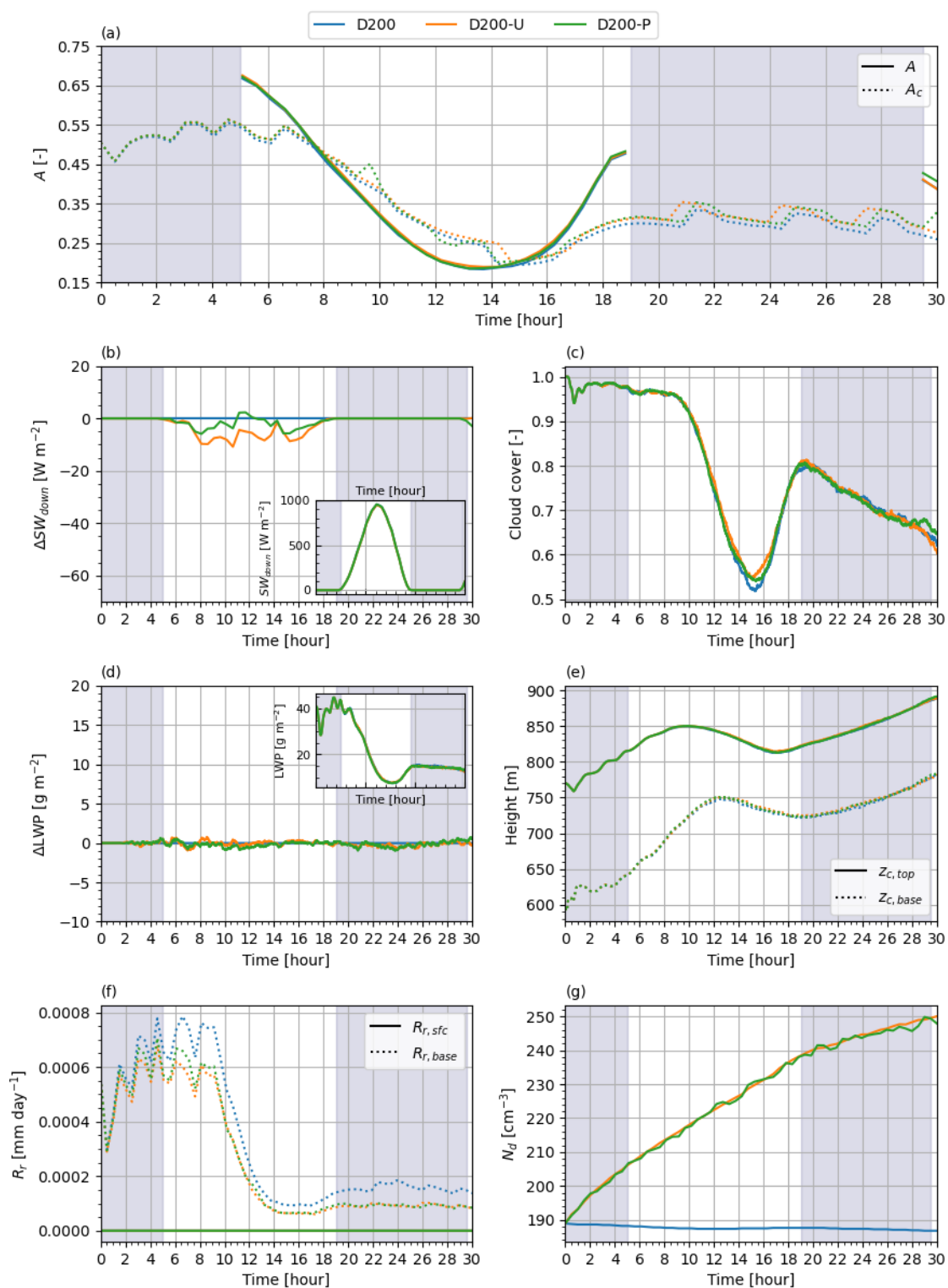


Figure 5.11: Same as Figure 5.2, but for the drier and warmer RF01 case, with a polluted maritime aerosol number concentration ($N_{ae,kg} = 200 \text{ cm}^{-3}$).

precipitation completely, causing the LWP to be above 100 g m^{-2} throughout the entire simulation. As our modified DALES model does not incorporate the effect of limited LWP on aerosol activation, the resulting N_d in our simulations are comparable to those found by WANG11. In contrast to the strongly diminishing cloud cover in our simulations, WANG11 found a reduction in LWP due to cloud seeding while the cloud fraction was sustained near unity. The loss of LWP minimised the brightening induced by the enhancement of N_d , making the W200 the least effective scenario for MCB activities.

5.5.2. LWP Budget Analysis

The LWP tendency contributions for the polluted cases W200 and D200 shown in Figures 5.12 and 5.13. The total LWP tendencies of W200 and D200 are in the same order of magnitude compared to the experiments with average and clean pollution levels. When comparing W200 with W50 and W100, the reduced loss of LWP due to precipitation is compensated by an increased loss due to entrainment during the first night. This is in line with the expectations of smaller cloud droplets, due to larger N_d , to suppress precipitation and with earlier findings of enhanced negative entrainment contribution when LWP levels are relatively higher. As the cloud reflectivity, cloud-base height, and cloud-top height for all pollution levels are approximately equal, the order of magnitude of the radiation contribution of the W200 experiments is similar to those of the W100 and W50 experiments and of the D200 experiments to those of the D100 and D50 experiments.

No significant deviations are found between the various contributions of the seeded and unseeded experiments of both W200 and D200. This result is in agreement with the minimal effect of N_d enhancement on both the cloud reflectivity and precipitation rate as seen in Figures 5.10 and 5.11.

The smaller contribution of cloud-base fluxes and radiation of the W200 experiment compared to those of W200-U and W200-P during the second night is again attributed to the reduced cloud cover. For the D200 experiment, the dip in cloud cover around 15 hours is not reflected in the contributions of cloud-base fluxes and radiation. This can be explained by the same domain-averaged LWP of D200 compared to D200-U and D200-P, causing the D200-U and D200-P to have a slightly thinner cloud layer. A thinner cloud layer causes less difference in radiation at the cloud-top and cloud-base, compensating for the increased difference due to a higher cloud cover. Similarly, the effect of reduced cloud cover for the radiation-driven turbulence below the cloud base is approximately nullified.

5.5.3. Summary

Finally, summarising the most important findings for the experiments of both the moist and cool (RF02) stratocumulus-topped boundary layer and the dry and warm stratocumulus-topped boundary layer (RF01) with high pollution levels, as presented in Figures 5.10, 5.11, 5.12 and 5.13:

- Seeding the RF02 cases with high pollution levels (W200) causes the liquid water path to decrease, while the increase in aerosol number concentration is less effective in increasing the cloud droplet number concentration than for the cases with cleaner pollution levels, generating a negligible reduction in shortwave radiation reaching the surface for the uniform spraying strategy and a slight increase for the point source strategy.
- For the RF01 cases with high pollution levels (D200), the liquid water path is not further reduced by the aerosol injection, but the increase in cloud droplet number concentration is less effective for these experiments compared to the cases with cleaner pollution levels

as well. Consequently, the aerosol injection generates a slightly higher solar radiation reflection than the RF02 cases with high pollution levels (W200).

- For all cases with high pollution levels, the different contributions to the liquid water path showed no deviations between the seeded and unseeded experiments, due to the minimal effect of cloud droplet number concentration enhancement on the cloud reflectivity and the precipitation rate.
- For the seeded RF01 cases with high pollution levels (D200-U and D200-P), the positive effect of a higher cloud cover on the contribution to the liquid water path of radiation and cloud-base turbulent fluxes is compensated by the negative effect of the thinner cloud layer on these contributions.

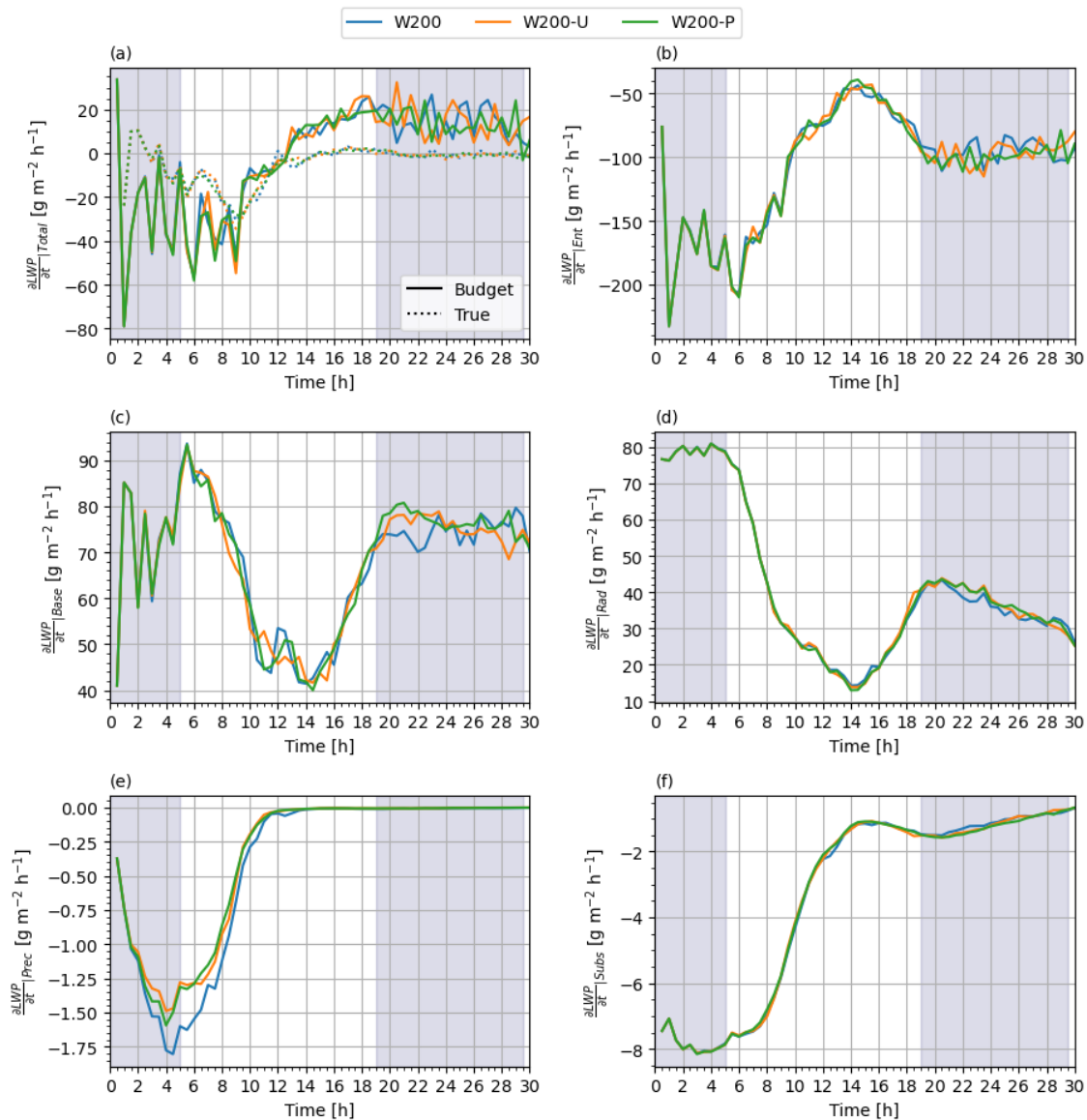


Figure 5.12: Same as Figure 5.4, but with a polluted maritime aerosol number concentration ($N_{ae,kg} = 200 \text{ cm}^{-3}$).

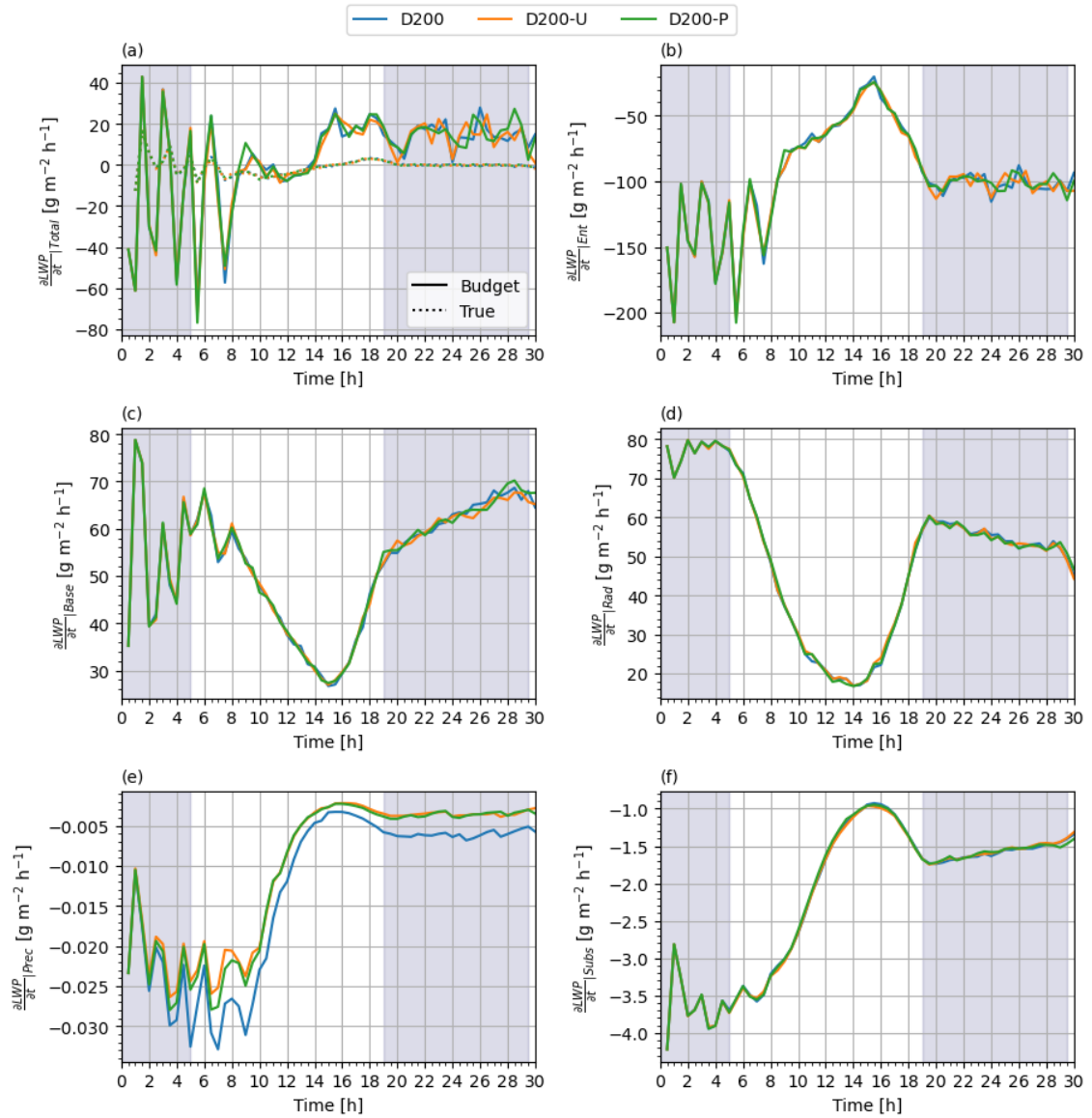


Figure 5.13: Same as Figure 5.4, but for the drier and warmer RF01 case, with a polluted maritime aerosol number concentration ($N_{ae,kg} = 200\ cm^{-3}$).

6

Entrainment Aerosol Transport Simulations

In this chapter, we present and discuss the simulations with various aerosol number concentration jumps across the inversion layer. With these simulations, the efficacy of cloud seeding with a surface aerosol source is examined under non-uniform vertical $N_{ae,kg}$ conditions. First, additional theoretical background is provided on the change of N_{ae} due to the jump in aerosol number concentration across the inversion layer, after which the simulation setup is discussed. Next, the results of the simulations will be presented and discussed, starting with the unseeded experiments to assess the effect of the inversion jump in N_{ae} . Then, these results will be compared to the experiments including a uniform aerosol source to assess the effectiveness of cloud seeding in STBLs with vertically non-uniform N_{ae} distributions.

6.1. Additional Theoretical Background

As stated in Subsection 2.2.2, both previous research on MCB as well as our simulations of Chapter 5 assume an initially uniform N_{ae} for the background concentration. However, Dadashazar et al. (2018) has shown that the N_{ae} in the STBL and the free troposphere can deviate considerably. Polluted air masses advected towards the marine region or nucleation in the free troposphere can cause the free-tropospheric concentration to be larger than in the STBL. On the other hand, Dadashazar et al. (2018) showed some cases for which the highest N_{ae} were found in the STBL as well. For remote marine boundary layers, a cleaner free troposphere compared to the STBL is common. Dadashazar et al. (2018) showed that the differences in N_{ae} between just above the cloud-top and the beginning of the free troposphere vary considerably, ranging from about $+400 \text{ cm}^{-3}$ to -100 cm^{-3} . The non-uniform vertical N_{ae} profile results in an additional source or sink of aerosols in the STBL. The derivation of the change of N_{ae} in time is provided in Section D in the appendix. The result of this derivation is as follows: assuming a well-mixed boundary layer and considering the flux-jump relation by Lilly (1968), the change of N_{ae} in the STBL over time can be expressed by:

$$\frac{\partial N_{ae}}{\partial t} = \frac{S_{N_{ae}} + w_e \Delta N_{ae}}{H}, \quad (6.1)$$

where $S_{N_{ae}}$ is surface spraying rate, ΔN_{ae} the difference in the aerosol number concentration just above the inversion height (N_{ae}^+) and just below the inversion height (N_{ae}^-) and H is the depth of the STBL. In this equation, H is equal to the inversion height z_i . This equation shows that with a positive w_e , N_{ae} in the STBL is enhanced when N_{ae} above the inversion layer is

larger than below the inversion layer and decreases when the opposite is true. Deepening of the STBL causes the effect of the fluxes $S_{N_{ae}}$ and $w_e \Delta N_{ae}$ on the change in aerosol number concentration to reduce, as can be seen by the inverse relation between $\frac{\partial N_{ae}}{\partial t}$ and H .

6.2. Simulation Setup

The entrainment aerosol transport simulations are performed for the W100 cases (no aerosol source, uniform source and point source at the domain surface) with various aerosol number concentration jumps across the inversion layer ($\Delta N_{ae,kg} = N_{ae,kg}^+ - N_{ae,kg}^-$). An overview of the simulations is given in Table 6.1, in which a prefix resembling the $\Delta N_{ae,kg}$ in percentage is added to the experiment notation presented in Section 5.2.

6.2.1. Aerosol Input

The aerosol number concentration in the free troposphere of RF01 and RF02 showed to be larger than in the STBL, with concentrations of about 350 and 250 cm^{-3} , respectively (Stevens et al., 2001). As this is an approximate difference of 50%, this value is chosen to be the maximum relative difference in aerosol number concentration between the STBL and the inversion layer.

As can be seen in Table 6.1, the base condition of the aerosol number concentration is 100 kg^{-1} , from which the initial number concentration above the inversion layer is modified by plus and minus 10%, 25% and 50%. Hence, the free-tropospheric $N_{ae,kg}^+$ cover the range of $N_{ae,kg}^+ = 50 \text{ kg}^{-1}$ to $N_{ae,kg}^+ = 150 \text{ kg}^{-1}$ for the aerosol number concentration in the STBL of $N_{ae,kg}^- = 100 \text{ kg}^{-1}$ in our simulations.

Table 6.1: Overview of the entrainment aerosol transport experiments. The same notation as in 5.1 is used with an additional prefix resembling the difference in aerosol number concentration between the STBL and the free troposphere ($\Delta N_{ae,kg} = N_{ae,kg}^- - N_{ae,kg}^+$), expressed as a percentage of the aerosol concentration in the STBL.

| Experiment | $N_{ae,kg}^- [\text{mg}^{-1}]$ | $N_{ae,kg}^+ [\text{mg}^{-1}]$ | $\Delta N_{ae,kg} [\%]$ |
|------------|--------------------------------|--------------------------------|-------------------------|
| 0W100 | 100 | 100 | 0 |
| 0W100-U | 100 | 100 | 0 |
| 10W100 | 100 | 110 | +10 |
| 10W100-U | 100 | 110 | +10 |
| 25W100 | 100 | 125 | +25 |
| 25W100-U | 100 | 125 | +25 |
| 50W100 | 100 | 150 | +50 |
| 50W100-U | 100 | 150 | +50 |
| -10W100 | 100 | 90 | -10 |
| -10W100-U | 100 | 90 | -10 |
| -25W100 | 100 | 75 | -25 |
| -25W100-U | 100 | 75 | -25 |
| -50W100 | 100 | 50 | -50 |
| -50W100-U | 100 | 50 | -50 |

6.2.2. Settings and Simulation Domain

For these simulations, a similar domain as for the validation simulation is modelled, using a horizontal domain of 128 by 128 grid points with a mesh size of 25 m and 100 vertical grid points with a mesh size of 20 m. The simulations are initiated at midnight and the simulation time is 6 hours. Statistics are sampled every 60 seconds, which are averaged every 600 seconds.

The 3200 m wide domain increases the source density in the point source experiments significantly, decreasing the spraying rate correspondingly. In this case, the simulated point source is no longer a suitable approximation of the point source proposed by Salter et al. (2008). Therefore, the point source strategy will not be considered for the entrainment aerosol transport simulations.

As these simulations cover a period during the night, the earlier used effective albedo A cannot be used, and the cloud albedo A_c is used to assess the efficacy of cloud seeding for the different conditions. Because A_c depends on N_{ae} through its relation with N_d , the focus of the discussion of the results will be on the cloud parameters that influence the change of N_{ae} over time, as expressed in Eq. (D.4): the inversion jump in N_{ae} , the boundary layer depth H , which is equal to the inversion height z_i , and the entrainment rate w_e . LWP is included in the analysis to assess whether changes in A_c result from changes in N_d , LWP or both. Precipitation is included to determine its contribution to the LWP budget.

6.3. Results: Excluding Surface Aerosol Source

First, the focus will be on the experiments excluding aerosol seeding. In Figure 6.1, the results for the simulations without a uniform surface aerosol source are presented as the difference, represented by δ , with respect to the base case 0W100 for which the vertical distribution of N_{ae} is uniform, and no surface aerosol source is applied. Figures 6.1(a1) and (a2) show the expected decrease and increase of the average aerosol number concentration in the cloud layer (N_{ae}^c) for the negative and positive inversion jump, respectively, due to the transport of aerosols between the STBL and the free troposphere. The relative differences between δN_{ae}^c between the experiments are related to the magnitude of the inversion jump in N_{ae} , where the loss of N_{ae} for -50W100 is about twice as large as that of -25W100 and about five times larger than for -10W100. The same is true for the positive inversion jumps 50W100, 25W100 and 10W100, where aerosols are not lost to the free troposphere but gained from it. The relation between δN_{ae}^c and the magnitude of the inversion jump in N_{ae} robustly shows a continuous entrainment aerosol transport between the STBL and the free troposphere, which should ideally be taken into consideration when simulating meteorological conditions with strong gradients in N_{ae} across the inversion layer. Note, however, that we do not take N_{ae} -reducing processes such as coagulation into account, which could affect the computed N_{ae}^c .

The differences in z_i , shown in Figures 6.1(b1) and (b2), are small compared to mean inversion height of $z_i^0 = 899.0$ m of the base case 0W100, indicating that the effect of z_i on $\frac{\partial N_{ae}}{\partial t}$ enhancement is minimal. This is reflected in the differences in entrainment rate, presented in Figures 6.1(c1) and (c2), which are relatively small as well compared to the base case mean entrainment rate of $w_e^0 = 1.08$, with a maximum deviation of about -0.08 cm s⁻¹. The relatively small differences in z_i and w_e are reflected in the values of δN_{ae}^c , which would have shown deviations from their direct relation with the jump in N_{ae} across the inversion if differences in z_i or w_e were to be higher (e.g. a mean w_e for -25W100 that is twice as large as that of -50W100 would result in an equal δN_{ae}^c).

The time-averaged¹ δw_e of Figures 6.1(c1) and (c2) are negative for all experiments. For the negative N_{ae} jumps, this is in agreement with the idea of fewer aerosols near the cloud-top causing the cloud droplet size to increase, which enhances precipitation near the cloud-top, limiting the available liquid water to be evaporated and thereby the entrainment rate. Surpris-

¹When referred to time-averages in this chapter, we refer to the time-average taken over the last 4 hours of the simulation to exclude the results generated during the approximately 2-hour spin-up period at the start of the simulation.

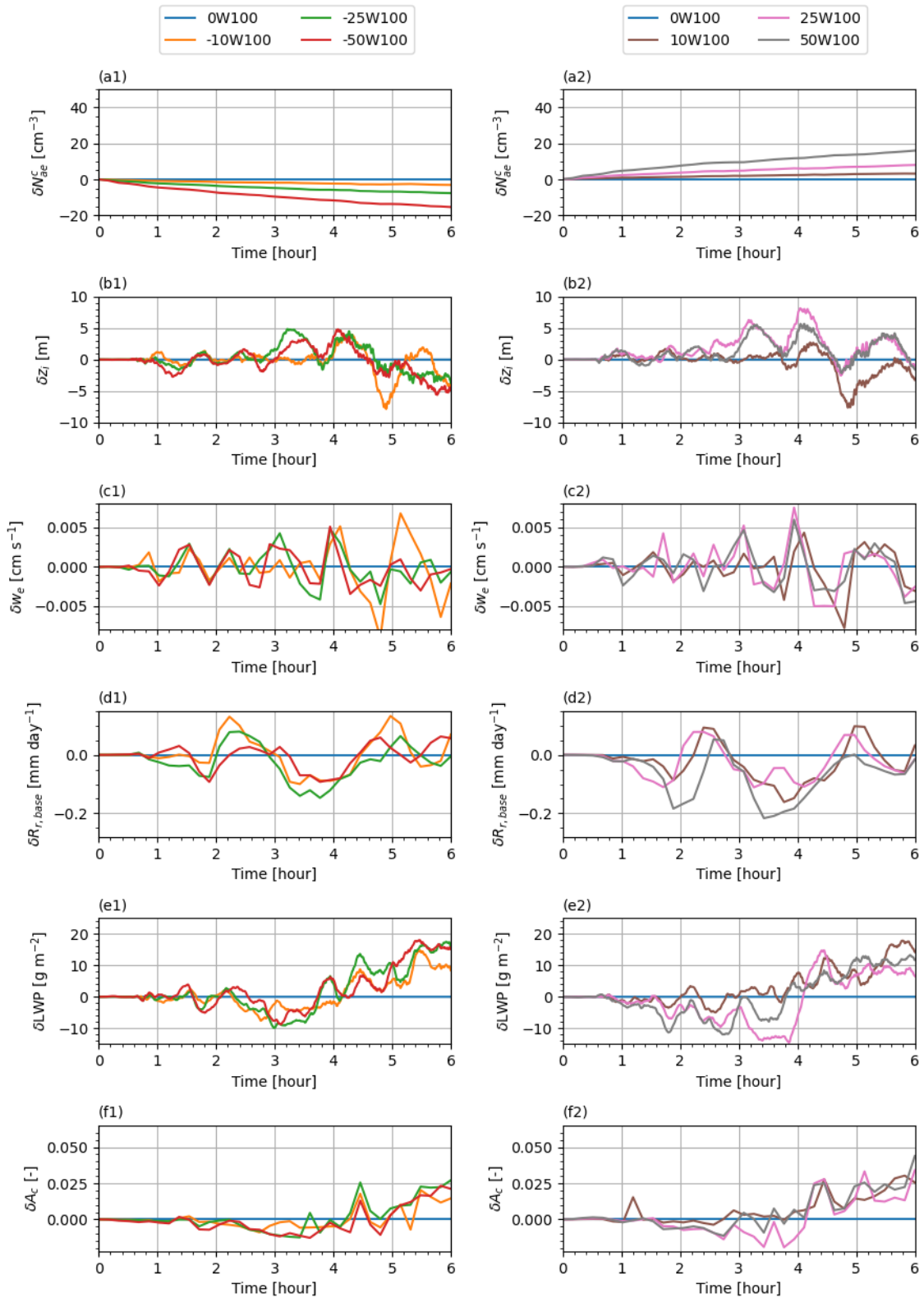


Figure 6.1: Domain-averaged differences of cloud properties to those of the 0W100 experiment with a vertically uniform aerosol number concentration (N_{ae}), for simulations with a range of negative and positive jumps in N_{ae} across the inversion layer. No surface aerosol source is applied in these simulations. The legend labels represent the experiments as presented in Table 6.1. The Figures on the left side show the results of the experiments with a negative jump in N_{ae} across the inversion layer. On the right side, the results of a positive jump are shown. Figures (a1) and (a2) show the difference in N_{ae} averaged over the cloud layer, (b1) and (b2) the difference in inversion height, (c1) and (c2) the difference in entrainment rate, (d1) and (d2) the difference in precipitation rate near the cloud-base, (e1) and (e2) the difference in LWP and (f1) and (f2) the difference in cloud albedo.

ingly, however, Figure 6.1(d1) shows no pronounced enhancement of the precipitation rate compared to that of 0W100. An alternative explanation for the reduced mean w_e is that N_{ae}^c reduction causes cloud droplet sedimentation to be larger, due to increased droplet mass. This removes liquid water from the upper cloud layer and consequently reduces the entrainment rate as well. However, this does not explain the intermittently reduced precipitation rates, which a reduction in LWP could explain. Upon analysing the LWP tendency contributions using the approach in Chapter 5, the negative δLWP between about 1.5 and 3.5 hours in Figure 6.1(e1) is caused by the stronger LWP reduction due to entrainment during this time interval, refuting the effect of sedimentation. More detailed investigation shows that the stronger LWP reduction due to entrainment is caused by relative increases in q_t and reduction in θ_l below the inversion layer with respect to 0W100, which together indicate a relative increase in q_l below the inversion layer. This result can be explained as follows: Reduced N_d at the cloud-top enhances the cloud droplet size in the upper layer of the cloud. The evaporative effect of entrainment on larger cloud droplets is smaller than for the smaller cloud droplets of 0W100 due to their smaller surface area. Consequently, a higher q_l is maintained in the upper layer, triggering higher entrainment-driven evaporation than for 0W100 for a short period. The increased evaporation reduces the LWP stronger than the increased cloud droplet size enhances the LWP relative to 0W100, causing a net reduction of LWP. The diminished LWP causes the precipitation rate to decrease as well, despite the increase in droplet size. As the LWP reduces and cloud droplet size increases in time, the negative effect of entrainment on the LWP reduces with respect to 0W100, and δw_e becomes more negative. Now the loss of LWP at the cloud-top is lower for the experiments with negative aerosol jumps, and the δLWP enhances, causing the mean increase in LWP that is obtained for the negative jumps in N_{ae} .

Another unexpected outcome is found when time-averaging the time evolutions of δw_e of the positive inversion jumps, shown in Figure 6.1(c2). These turn out to be slightly negative, which would be expected to be positive based on the theories of enhanced N_d causing a reduction in cloud droplet sedimentation and precipitation (which is generally shown in Figure 6.1(d2) and is significant compared to the mean precipitation rate of $0.205 \text{ mm day}^{-1}$ of 0W100) and an increase in evaporation. This challenges the explanation of increased sedimentation being the source of w_e reduction as well. What causes the counter-intuitive effects on entrainment for the positive jumps is as yet unclear. In addition, the time evolution of δw_e of 25W100 shows a relatively strong correlation with that of 50W100, whereas the time evolutions of $\delta R_{r,base}$ do not. This indicates that the additional aerosols entering at the cloud-top in the 50W100 experiment with respect to the 25W100 experiment have a relatively strong effect on the suppression of precipitation, but have limited additional effect on the entrainment rate.

The differences in LWP are shown in Figures 6.1(e1) and (e2). A potential explanation of the time evolutions of the negative aerosol jumps is provided above. For the positive aerosol jumps, the reduction in precipitation rate is insufficient to compensate for the loss of LWP due to changes in the other process that contribute to the LWP caused by the increase in N_{ae}^c , generating a net decrease in δLWP during the first 4 hours. After the first 4 hours, δLWP becomes positive, which can be explained by the general decrease in the difference in entrainment rate compared to the entrainment rate of 0W100, indicating a reduction in the loss of LWP due to entrainment.

The net effects of the inversion jumps in N_{ae} on the cloud albedo are shown in Figures 6.1(f1) and (f2). For the negative aerosol jumps, both the loss of N_{ae}^c due to the entrainment aerosol transport and the initial reduction in LWP contribute to a reduction in A_c compared to that of 0W100. However, when δLWP becomes positive, this compensates for the reduction of A_c due to the reduction in N_{ae}^c , and δA_c becomes positive. For the positive aerosol jumps, the

negative δA_c during the approximate first 4 hours of the simulation is caused by the decrease in LWP in this period. This effect is damped by the increase in N_{ae}^c , which can be seen by the nearly equal δA_c of 25W100 and 50W100 just before 2 hours, despite the pronounced difference in δLWP at this point in time.

The time-averaged differences in cloud albedo of all experiments are relatively small compared to the mean albedo of 0.711 of the base case with a vertically uniform N_{ae} , as they do not surpass 0.01 in any of them. However, the precipitation-suppressing effect on the cloud layer of the positive jumps in N_{ae} potentially have a larger effect on A_c than modelled in this study. If N_{ae}^c depletion due to precipitation is incorporated in the microphysics scheme of the simulation model, the more concentrated free troposphere serves as an additional source of N_{ae} that may dampen the positive feedback mechanism between precipitation and aerosol depletion. Similarly, additional aerosol depletion for the negative jumps in N_{ae} may amplify this feedback mechanism, although the relation of precipitation enhancement and loss of aerosols at the inversion jump is not evident from the experiments. As a consequence of the potential damping or amplification, other cloud properties and processes such as the entrainment rate and the radiation budget are affected. This adds to the interest in constructing a microphysical model that includes the role of aerosols as cloud condensation nuclei to improve cloud simulations.

6.4. Results: Including Surface Aerosol Source

To assess the efficacy of MCB in STBLs with vertically non-uniform N_{ae} distributions, the results of the experiments including aerosol injection (Figure 6.2) are compared to those without (Figure 6.1). Figure 6.2(a2) shows that for a vertically uniform N_{ae} distribution, the increase due to the surface source is about 30 cm^{-3} after 6 hours. Comparing δN_{ae}^c of the seeded experiments with that of their unseeded equivalents shows the same increase in N_{ae}^c as a result of the surface injection. This indicates that no significant differences in the vertical transport of aerosols into the cloud layer are induced by the N_{ae} inversion jump. This is in agreement with the resulting δz_i , which are still relatively small compared to the z_i^0 of 889.0 m, and thereby have no significant effect on $\frac{\partial N_{ae}}{\partial t}$.

The inversion jump of -50 mg^{-1} , corresponding to experiment -50W100, causes a decrease in N_{ae}^c of about 15 cm^{-3} after 6 hours, which is half of the enhancement due to the applied spraying rate. Due to the proportionality of decreasing N_{ae}^c with the inversion jump in N_{ae} , the aerosol source is able to fully replenish an STBL with an inversion jump up to about -100 mg^{-1} .

The inversion heights of -50W100-U, -10W100-U and all positive jumps show to be generally increased due to the aerosol injection, which corresponds to their general increase in δw_e . The negative Δz_i and Δw_e for 0W100-U are surprising, as it would be expected that the entrainment rate would increase due to the higher cloud droplet number concentration. The largest positive aerosol jump without an aerosol source (50W100) generates only half of the increase in δN_{ae}^c compared to 0W100-U, but does show a general increase in δw_e and δz_i , unlike 0W100-U. This indicates that introducing additional aerosols from below or above the cloud affects the cloud differently. What processes cause these differences are as yet unclear, but might be of interest for future studies.

In agreement with the expected effect of enhanced N_{ae}^c , all experiments show a significant reduction of the precipitation rate. Compared to their unseeded equivalents, the strongest precipitation suppression is generated in the experiments -50W100-U and -10W100-U. For these experiments, the positive $\delta R_{r,base}$ around 5 hours in Figure 6.1(d1) are replaced by a reduction in precipitation rate with respect to the 0W100 case in Figure 6.2(d1). 0W100-U,

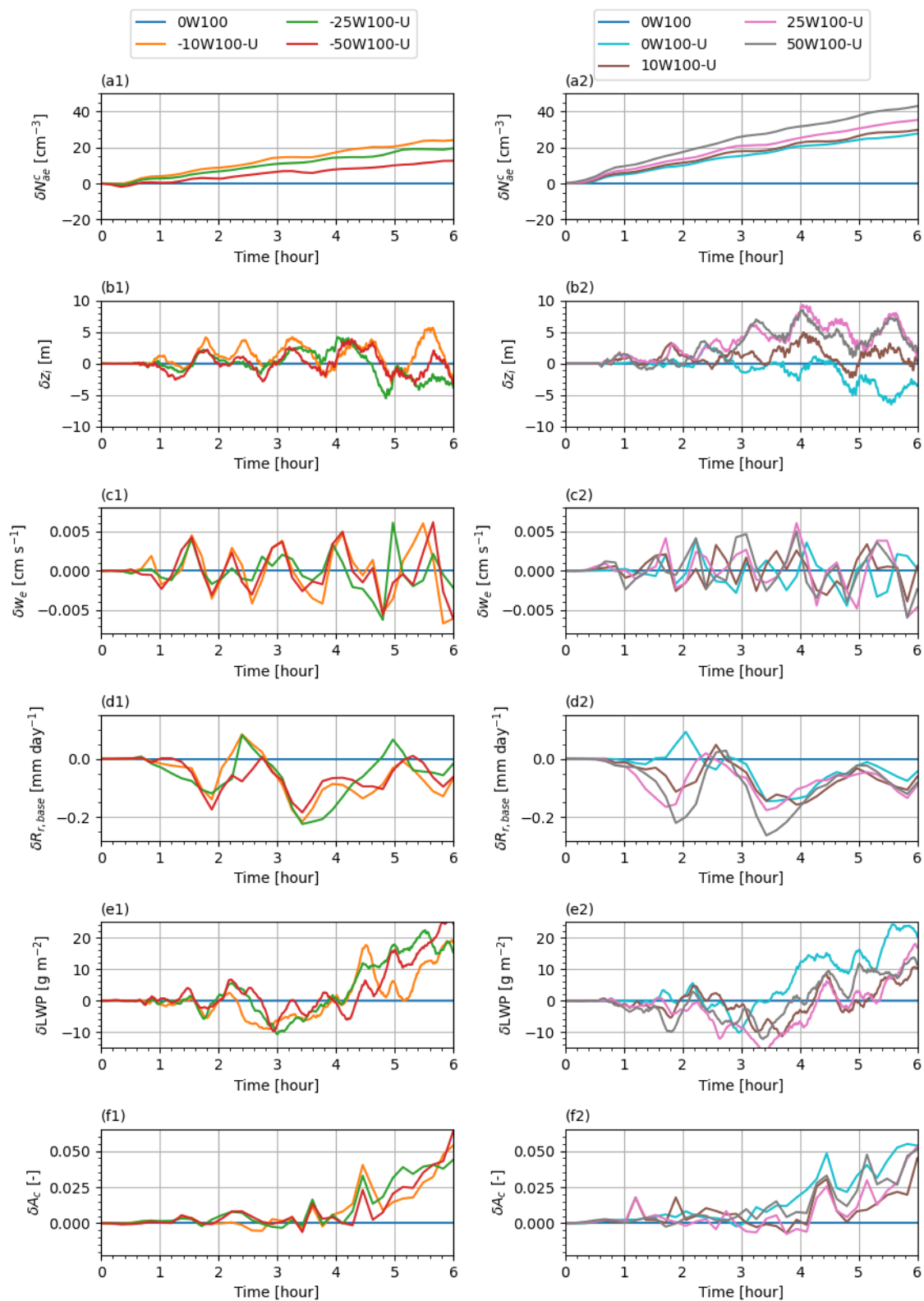


Figure 6.2: Same as in Figure 6.1, with the addition of a uniform surface aerosol source applied in the simulations. The domain-averaged differences in cloud properties are again with respect to those of the 0W100 experiment.

10W100-U and 25W100-U show a similar reduction in Figure 6.2(d2). For -25W100-U and especially for 50W100-U, the extra precipitation suppression with respect to their unseeded equivalents (-25W100 and 50W100, respectively) is relatively marginal. The small difference in $\delta R_{r,base}$ between 50W100 and 50W100-U can be explained by the fact that the enhancement in N_{ae}^c , as a result of entrainment aerosol transport, already causes the precipitation to be largely suppressed. This way, the additional enhancement in N_{ae}^c has limited effect on the precipitation rate. For -25W100-U, however, it would be expected that $\delta R_{r,base}$ is comparable with that of -50W100 and -10W100, but the aerosol injection is less effective in reducing the precipitation rate. From these results, it can be deduced that an increase in N_{ae}^c generates the suppression of R_{cb} , but no general statement can be made on the relation between the loss of N_{ae}^c to the free troposphere and R_{cb} . The fact that the reduction in R_{cb} cannot simply be scaled with the increase in N_{ae}^c is in line with the earlier findings of varying sensitivity of R_{cb} to N_d with varying LWP, for which even the sign of the sensitivity is uncertain (Wood, 2012).

The strongest increase in LWP due to aerosol injection is generated for 0W100-U, due to the general reduction in w_e and R_{cb} . In combination with the enhanced N_{ae}^c , this experiment gives the largest increase in δA_c compared to its unseeded variant 0W100 with a difference of about 0.055 after 6 hours. For the negative aerosol jumps, the period of negative δLWP found in Figure 6.1(e1) is found in Figure 6.2(e1) as well, but the precipitation suppression causes a significant increase in δLWP after about 4 hours. Due to the aerosol seeding, the period of reduced δA_c found in Figure 6.1(f1) is nearly completely replaced by a positive δA_c . Due to the strong increase in δLWP after about 4 hours, δA_c after 6 hours is approximately 0.45 higher for -50W100-U compared to that of -50W100. This is also the case for -10W100-U compared to -10W100. For -25W100-U, the increase in δA_c is less pronounced after 6 hours than that of -25W100, but shows a comparable mean increase in δA_c due to the aerosol injection compared to -50W100-U and -10W100-U. As stated earlier, the effect of aerosol injection has the potential to be larger for STBLs with a negative inversion jump in N_{ae} that cause precipitation enhancement when the loss of aerosols in the cloud layer is coupled to the precipitation rate in the simulation model. For 25W100-U and 50W100-U, the increases in δA_c with respect to their unseeded equivalents after 6 hours are only about 0.03 and 0.01, respectively. However, the time-averaged δA_c show an increase of approximately 0.075 and 0.09, respectively. For both experiments, the δLWP is reduced due to an increase in δw_e , which causes more liquid water to be evaporated than is suppressed to rain-out due to the enhancement in N_{ae}^c . The net positive effect on A_c of 25W100-U and 50W100-U is because the enhancement in N_{ae}^c , and thereby in N_d , has a larger positive effect than the negative effect of LWP loss. For 10W100-U, the strong reduction in δLWP causes the effect of enhancement in N_{ae}^c on A_c to be nearly completely cancelled, resulting in a negligible increase in δA_c compared to its unseeded base case 10W100.

Conclusions and Recommendations

7.1. Conclusions

One of the goals of this thesis was to assess how cloud properties and processes are altered by injecting aerosols from the oceanic surface into the cloud layer and how this affects its ability to reflect solar radiation back into space. This was done by performing simulations with the Dutch Atmospheric Large-Eddy Simulation (DALES) model. Several modifications had to be made to the simulation model to incorporate the representation of aerosols into DALES. The aerosol number concentration N_{ae} is added to the model as an additional scalar that is subject to advection, subsidence and diffusion. The vertically uniform and time-constant cloud droplet number concentration N_d in the standard DALES model is replaced by a parameterisation equation that prescribes the translation of N_{ae} to N_d , which is based on the findings of Twohy et al. (2005). The aerosol injection was performed using a horizontally uniformly distributed source or a point source. The former is readily available in DALES, and the latter was obtained by applying the surface flux to a single grid cell only.

The effect of surface aerosol injection on marine stratocumulus cloud properties that determine its radiative balance shows varying results for the different meteorological scenarios and pollution levels considered in this study. LES simulations were performed for a relatively wet and dry stratocumulus-topped boundary layer (STBL), based on measurement of the DYCOMS-II, and for relatively clean, average and polluted aerosol background number concentrations. Results showed that reducing downwelling solar radiation at the surface was most effective for clean background pollution levels in both the wet and dry STBL, approaching about half of the radiative forcing required to compensate the forcing resulting from CO₂ doubling fully. This is attributed to the more pronounced precipitation rate in clean STBLs, which is partially suppressed due to the aerosol seeding (the second indirect aerosol effect), and to the relatively large increase of N_{ae} with respect to its background concentration (the first indirect aerosol effect). For the wet conditions, both indirect aerosol effects contributed to realised radiative forcing, whereas the first indirect aerosol effect was dominant for the dry conditions.

For the experiments with average marine pollution levels, the efficacy of marine cloud brightening was smaller than for the cleaner STBLs. For the wet experiments, the produced radiative forcing diminished to about a third of that of the cleaner conditions, whereas about 50% to 75% remained for the dry experiments. The higher aerosol background concentration generated a significantly lower precipitation rate for the wet conditions than for the cleaner STBL, which reduced the suppressing effect of N_d enhancement and its related effect on solar radiation

reflection. For the drier conditions, the enhancement in solar reflection is mainly due to the first indirect aerosol effect and of secondary importance due to the temporary enhancement of cloud cover for the simulation including the point source.

The experiments with the highest pollution level generated the least reduction in solar radiation reaching the surface, approaching values that are insignificant in the eye of MCB. The dry experiments showed the largest efficacy of these experiments, because the LWP is nearly unaltered by the N_d enhancement. The sublinear N_{ae} to N_d parameterisation causes a reduced first indirect aerosol effect compared to the less polluted experiments. For the wet experiments, the slightly higher LWP of the unseeded experiment allows some residual cloud water to be evaporated when N_d is enhanced, which further decreases its impact on solar radiation reflection.

The difference in efficacy between the uniform and point source variate among the experiments as well. For the wet and clean experiment and the dry and average polluted experiment, the point source was most effective, attributed to the higher cloud cover than for the uniform source due to more local cloud thinning. For the wet and averagely polluted experiment, the opposite is true and shows a minor difference in radiative forcing in favour of uniform seeding. For the dry and clean environment, for which the first aerosol effect is most important for the radiative forcing, the effect of more localised cloud thinning is surpassed by the effect of an evenly spread brightening effect of the uniform source. The positive effect of the more localised cloud thinning was not evident for the experiments with the highest pollution levels, and the difference in radiative forcing between the spraying strategies is caused by the more evenly distributed first indirect aerosol effect.

The results in this study turned out to deviate strongly from the findings of WANG11. This is most likely due to the difference in the modelled precipitation rate. Both the standard and our modified version of DALES does not incorporate the loss of aerosols and consequently of cloud droplets due to precipitation, which is included in the microphysics scheme of the model of WANG11. As this both dilutes the aerosol number concentration in the cloud layer and hereby enhances the precipitation rate, the effect of aerosol replenishment by surface injections has the potential to have more impact on precipitation suppression than modelled in this study. Moreover, the reduced N_d enhances the cloud droplet size, which reduces the loss of LWP by entrainment. In addition, the parameterisation of N_{ae} to N_d implicitly incorporates the effect of N_d on the supersaturation, but this no longer holds for the relatively low LWP found in this study. Explicit modelling of this effect, as in WANG11, is expected to reduce the activation of aerosols and lower the radiative forcing generated for drier and more polluted conditions.

For precipitating STBLs, the main effect of the increased aerosol concentrations on LWP is the suppression of rain-out, which positively affect the LWP. For the drier STBLs, the differences in LWP tendencies showed to be considerably smaller due to the absence of precipitation. The main cause of differences in LWP tendencies for these experiments was attributed to the differences in cloud cover.

When precipitation is suppressed due to aerosol seeding, the reduced loss of LWP is countered by a reduction of positively contributing turbulent fluxes in q_t and θ_t near the cloud-base, because of the reduction in water vapor in the sub-cloud layer as a result of the precipitation suppression.

Enhanced loss of LWP due to entrainment is only apparent when the increase in LWP due to precipitation suppression is sufficiently high (order of $1 \text{ g m}^{-2} \text{ h}^{-1}$), as for the clean and

average polluted wet conditions. This effect is absent for the most polluted wet conditions and all drier conditions, which all produce such a low precipitation rate in their unseeded cases that further suppression has a limited effect on the LWP.

The effect of cloud seeding on the cloud cover is reflected in the LWP tendency contribution of the radiation difference between cloud-top and cloud-base and in the contribution of subsidence. Enhancing cloud cover has the potential to significantly increase the contribution of radiation, as it is one of the main contributors to the total LWP tendency. In addition, as increased cloud cover shows a positive effect on the LWP, which then has a positive effect on the cloud cover, this indicates a positive feedback mechanism. Because the order of magnitude of the contribution of subsidence is much smaller than the contribution of entrainment, cloud-base fluxes or radiation, differences in LWP due to alterations in subsidence are of minor importance.

All in all, for MCB to exploit the second indirect aerosol effect, it is most effective to suppress rain-out of precipitating clouds and enhance cloud cover to trigger the feedback mechanisms of the radiation contribution to the LWP.

The incorporation of jumps in N_{ae} across the inversion layer showed the expected changes in the N_{ae} of the cloud layer (N_{ae}^c) based on the flux-jump relation, indicating proportional entrainment aerosol transport between the free troposphere and the boundary layer with respect to the ratio of free-tropospheric and boundary layer N_{ae} . Effects on the entrainment rate for positive inversion jumps in N_{ae} and on the precipitation rate for negative jumps are relatively marginal, but do show deviations that cannot be explained by the effects of changes in cloud droplet size on the entrainment rate, the sedimentation- and evaporation-entrainment effects and the coupling between precipitation and entrainment. All positive jumps in N_{ae} showed some enhancement in cloud albedo in various degrees, depending on the balance between the first and second indirect aerosol effect. For the negative jumps in N_{ae} , the LWP increased considerably towards the end of the simulations. However, its effect on the cloud albedo was largely compensated by the continuous reduction in N_{ae}^c and consequently in N_d .

The applied aerosol injection rate is sufficiently strong to more than fully replenish the aerosols lost to the free troposphere. Cloud seeding turned out to be most effective for the negative and neutral aerosol jumps. This is due to the combination of its ability to sustain the largest LWP by precipitation suppression at the cloud-base and reduced evaporation at the cloud-top and the contribution to the first indirect aerosol effect of the injected aerosols. For the positive aerosol jumps, the additional loss of LWP to entrainment and the reduced susceptibility of N_d to increases in N_{ae}^c causes MCB to be less effective in enhancing cloud albedo.

Although the precipitation rate did not show the expected enhancement of the precipitation rate due to the loss of aerosols to the free troposphere in this study, cloud seeding could be even more effective if N_d and precipitation rate showed to be more directly coupled as stated in other studies.

All in all, the results presented in this thesis provide valuable first insights into how modifications of cloud droplet number concentration from surface sources and free-tropospheric sources and sinks alter the cloud processes and feedback mechanisms that affect the cloud's radiative forcing. However, the conclusions on the efficacy of MCB producing a significant cooling effect deviate from previous research, which is most likely due to the relatively simplistic parameterisation of the aerosol activation process. Hence, the presented results are inconclusive on this matter. However, they do highlight the importance of more physical treatment of aerosol and cloud droplet number concentrations in DALES if it is to be used to study

processes like MCB further.

7.2. Recommendations

As stated above, a significant improvement on the performed simulations can be made by incorporating the aerosol depleting effect of precipitation. A first step in this is to incorporate aerosol rain-out for precipitating clouds, which has been shown to be an essential factor in the LWP budget in the study of WANG11. For non-precipitating clouds, it is suggested to improve the results by including the relation between the cloud droplet number concentration and the cloud's relative humidity to prevent overestimating the number of activated aerosols and consequently the first indirect aerosol effect. Further model refinement could be realised by including the microphysical processes behind aerosol activation.

In this thesis, the size distribution of the injected aerosols is implicitly taken equal to that of the background concentration. However, for MCB, it is useful to seed the boundary layer with aerosols of a specific size distribution to generate the most activation and prevent the formation of large cloud droplets that are likely to precipitate. When an aerosol activation scheme that includes the microphysics is realised, this enables to research the effect of injecting aerosols of different size distributions on the efficacy of MCB.

Next to the recommended improvements on the parameterisation model, reducing the grid size may provide additional insights into the processes that happen on the scale below a few tens of metres. This is especially recommended for the vertical grid size as the chosen grid size of 20 m is coarse compared to the scale of entrainment-driven processes, which are a major factor in cloud processes that control the radiative forcing. A wider horizontal domain is recommended as well. This allows creating more virtual distance between the point sources, mimicking vessel-based aerosol injections more closely, and determining the effects of more concentrated cloud injections.

The simulations in this thesis are performed for a shallow stratocumulus-topped boundary layer, because a shallow stratocumulus-topped boundary layer is expected to be more susceptible to aerosol injections compared to deeper ones (see Chapter 2). However, most of the stratocumulus-topped boundary layers are found to be of the deeper variant (Possner et al., 2020). It is advisable to diversify the MCB simulations to various meteorological scenarios to further assess their efficacy in generating a cooling radiative forcing. Aerosol injection into deeper regimes may affect cloud processes and properties differently, altering the conclusions drawn for shallow regimes.

Although in this thesis only the first step in incorporating the representation of aerosols is made to which many basic refinements can be applied to improve modelling the first and second indirect effect, it is recommended to include the radiative effects of aerosol concentrations and compositions to incorporate the direct and semi-direct as well. Previous research has shown that these effects can lead to modified radiative forcings, even in the absence of clouds (Ahlm et al., 2017; Jenkins et al., 2013).

Due to the horizontal periodic boundary conditions, the simulated domain can be regarded as part of a larger system in which MCB is deployed. Therefore, our results do not represent the effects of aerosol injection for domains near the edges of this larger system. Moreover, one might be interested in determining the effects of MCB in an isolated domain. To simulate an isolated domain or a domain at the edge of a larger system, the diffusion of N_{ae} near the domain's edges is recommended to be included in the simulation. A suggestion of a module to do so is provided in Chapter E in the appendix, which gives the option to nudge the aerosol number concentrations to the initial background values near the edges of the domain.

In addition to the performed simulations including differences in aerosol number concentrations across the inversion jump, two recommendations can be made. First, it is suggested to consider the difference in size and composition between free-tropospheric aerosols and boundary layer aerosols. Aerosols in the free troposphere that are advected from continental regions or result from nucleation are different from those in the STBL. They may be activated differently and grow differently, affecting other cloud properties as a result. Secondly, in this research, an immediate aerosol inversion jump is taken instead of an inversions entrainment layer in which the aerosol concentration increases or decreases more gradually. By considering a gradual inversion, the efficiency of the entrainment aerosol transport may be reduced as it reduces the difference in aerosol number concentration in the exchanging layers.

Last of all, it is recommended to perform the MCB simulations using a variety of LES models. As shown in Chapter 4, DALES generates a relatively high entrainment rate and low precipitation rate, which both have a negative effect on the LWP and reduce the potential of MCB efficacy beforehand. An inter-comparison study in which different LES models deploy a similar MCB strategy would provide more robust insight into the workings of aerosol injections in stratocumulus-topped boundary layers.

Bibliography

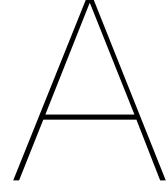
- Ackerman, A., Kirkpatrick, M., Stevens, D., & Toon, O. (2004). The impact of humidity above stratiform clouds on indirect aerosol climate forcing. *Nature*, *432*, 1014–1017.
- Ackerman, A., vanZanten, M., Stevens, B., Savic-Jovicic, V., Bretherton, C., Chlond, A., Golaz, J., Jian, H., Khairoutdinov, M., Krueger, S., Lewellen, D., Lock, A., Moeng, C., Nakamura, K., Petters, M., Snider, J., Weinbrecht, S., & Zulauf, M. (2009). Large-eddy simulations of drizzling, stratocumulus-topped marine boundary layer. *Monthly Weather Review*, *137*(3), 1083–1110. <https://doi.org/10.1175/2008MWR2582.1>
- Ahlm, L., Jones, A., Stjern, C., Muri, H., Kravitz, B., & Krstjansson, J. (2017). Marine cloud brightening - as effective without clouds. *Atmospheric Chemistry and Physics*, *17*, 13071–13087. <https://doi.org/10.5194/acp-17-13071-2017>
- Albrecht, B. (1989). Aerosols, cloud microphysics, and fractional cloudiness. *Science*, *245*(4923), 1227–1230. <https://doi.org/10.1126/science.245.4923.1227>
- Alterskjær, K., & Kristjánsson, J. (2013). The sign of the radiative forcing from marine cloud brightening depends on both particle size and injection amount. *Geophysical Research Letters*, *40*, 210–215. <https://doi.org/10.1029/2012GL054286>
- Bader, D., Covey, C., Gutowski, W. J., Held, I., Kunkel, K., Miller, R., Tokmakian, R., & Zhang, M. (2008). Climate models: An assessment of strengths and limitations. *Geological and Atmospheric Sciences Reports*, (3). https://lib.dr.iastate.edu/ge_at_reports/3
- Bala, G., Caldeira, K., Nemani, R., Cao, L., Ban-Weiss, G., & Shin, H.-J. (2011). Albedo enhancement of marine clouds to counteract global warming: Impacts on the hydrological cycle. *Climate Dynamics*, *37*, 915–931. <https://doi.org/10.1007/s00382-010-0868-1>
- Bretherton, C., Blossey, P., & Uchida, J. (2007). Cloud droplet sedimentation, entrainment efficiency, and subtropical stratocumulus albedo. *Geophysical Research Letters*, *34*(L03813). <https://doi.org/10.1029/2006GL027648>
- Connolly, P., McFiggans, G., Wood, R., & Tsiamis, A. (2014). Factors determining the most efficient spray distribution for marine cloud brightening. *Philosophical Transactions of the Royal Society A*, *372*(2031). <https://doi.org/10.1098/rsta.2014.0056>
- Cronin, T. (2014). On the choice of average solar zenith angle. *Journal of the Atmospheric Sciences*, *71*(8), 2994–3003. <https://doi.org/10.1175/JAS-D-13-0392.1>
- Curry, J., & Webster, P. (1999). *Thermodynamics of atmospheres and oceans* (65th ed.). International Geophysics.
- Dadashazar, H., Braun, R., Crosbie, E., Chuang, P., Woods, R., Jonsson, H., & Sorooshian, A. (2018). Aerosol characteristics in the entrainment interface layer in relation to the marine boundary layer and free troposphere. *Atmospheric Chemistry and Physics*, *18*, 1495–1506. <https://doi.org/10.5194/acp-18-1495-2018>
- Eastman, R., & Wood, R. (2018). The competing effects of stability and humidity on subtropical stratocumulus entrainment and cloud evolution from a lagrangian perspective. *Journal of the Atmospheric Sciences*, *75*, 2563–2578. <https://doi.org/10.1175/JAS-D-18-0030.1>
- Feingold, G., Balsells, J., Glassmeier, F., Yamaguchi, T., Kazil, J., & McComiskey, A. (2017). Analysis of albedo versus cloud fraction relationships in liquid water clouds using heuristic models and large eddy simulation. *JGR Atmospheres*, *122*(13), 7086–7102. <https://doi.org/10.1002/2017JD026467>

- Galbraith, J. (2021). Values in early-stage climate engineering: The ethical implications of “doing the research”. *Studies in History and Philosophy of Science*, 86, 103–113. <https://doi.org/10.1016/j.shpsa.2021.01.009>
- Grosvenor, D., Sourdeval, O., Zuidema, P., Ackerman, A., Alexandrov, M., Bennartz, R., Boers, R., Cairns, B., Chiu, J., Christensen, M., Deneke, H., Diamond, M., Feingold, G., Fridlind, A., Hünerbein, A., Knist, C., Kollias, P., Marshak, A., McCoy, D., ... Quaas, J. (2018). Remote sensing of droplet number concentration in warm clouds: A review of the current state of knowledge and perspectives. *Reviews of Geophysics*, 56(2), 409–453. <https://doi.org/10.1029/2017RG000593>
- Gultepe, I., & Isaac, G. (1996). The relationship between cloud droplet and aerosol number concentrations for climate models. *International Journal of Climatology*, 16(8), 941–946. [https://doi.org/10.1002/\(SICI\)1097-0088\(199608\)16:8<941::AID-JOC57>3.0.CO;2-O](https://doi.org/10.1002/(SICI)1097-0088(199608)16:8<941::AID-JOC57>3.0.CO;2-O)
- Hede, T. (2013). *Beyond köhler theory* (tech. rep.). Stockholm University.
- Heus, T., Van Heerwaarden, C., Jonker, H., Siebesma, A. P., Axelsen, S., Van den Dries, K., Geoffroy, O., Moene, A., Pino, D., De Roode, S., & Vilà-Guerau de Arellano, J. (2010). Formulation of the dutch atmospheric large-eddy simulation (dales) and overview of its applications. *Geoscientific Model Development*, 3, 415–444. <https://doi.org/10.5194/gmd-3-415-2010>
- Hill, A., Feingold, G., & Jiang, H. (2009). The influence of entrainment and mixing assumption on aerosol-cloud interactions in marine stratocumulus. *Journal of the Atmospheric Sciences*, 66(5), 1450–1464. <https://doi.org/10.1175/2008JAS2909.1>
- Hoffmann, F., & Feingold, G. (2019). Entrainment and mixing in stratocumulus: Effects of a new explicit subgrid-scale scheme for large-eddy simulations with particle-based microphysics. *Journal of the Atmospheric Sciences*, 76(7), 1995–1973. <https://doi.org/10.1175/JAS-D-18-0318.1>
- Hundsdoerfer, W., Koren, B., vanLoon, M., & Verwer, J. (1993). *A positive finite-difference advection scheme applied on locally refined grids* (tech. rep.). Centrum Wiskunde en Informatica. Department of Numerical Mathematics [NM].
- IPCC. (2019). *Emission gap report 2019* (tech. rep.). United Nations Environment Programme.
- Jansson, F., Edeling, W., Attema, J., & Crommelin, D. (2021). Assessing uncertainties from physical parameters and modelling choices in an atmospheric large eddy simulation model. *Philosophical Transactions of the Royal Society A*, 379(2197). <https://doi.org/10.1098/rsta.2020.0073>
- Jenkins, A., Forster, P., & Jackson, L. (2013). The effects of timing and rate of marine cloud brightening aerosol injection on albedo changes during the diurnal cycle of marine stratocumulus clouds. *Atmospheric Chemistry and Physics*, 13, 1659–1673. <https://doi.org/10.5194/acp-13-1659-2013>
- Karset, I., Gettelman, A., Storelvmo, T., Alterskjær, K., & Berntsen, T. (2020). Exploring impacts of size-dependent evaporation and entrainment in a global model. *Journal of Geographical Research: Atmospheres*, 125(e2019JD031817). <https://doi.org/10.1029/2019JD031817>
- Kim, D.-H., Shin, H.-J., & Chung, I.-U. (2020). Geoengineering: Impact of marine cloud brightening control on the extreme temperature change over east asia. *Atmosphere*, 11(1345). <https://doi.org/doi.org/10.3390/atmos11121345>
- Lacis, A., & Hansen, J. (1974). A parameterization for the absorption of solar radiation in the earth's atmosphere. *Journal of the Atmospheric Sciences*, 31, 118–133. [https://doi.org/10.1175/1520-0469\(1974\)031](https://doi.org/10.1175/1520-0469(1974)031)
- Latham, J. (1990). Control of global warming? *Nature*, 347(6291), 339.

- Latham, J., Bower, K., Choulaton, T., Coe, H., Connolly, P., Cooper, G., Craft, T., Foster, J., Gadian, A., Galbraith, L., Iacovides, H., Johnston, D., Launder, B., Leslie, B., Meyer, J., Neukermans, A., Ormond, B., Parkes, B., Rasch, P., ... Wood, R. (2012). Marine cloud brightening. *Philosophical Transactions of the Royal Society A-Mathematical Physical and Engineering Sciences*, 370(1974). <https://doi.org/10.1098/rsta.2012.0086>
- Latham, J., Rasch, P., Chen, C., Kettles, L., Gadian, A., Gettelman, A., Morrison, H., K., B., & Choulaton, T. (2008). Global temperature stabilization via controlled albedo enhancement of low-level maritime clouds. *Philosophical Transactions of the Royal Society A-Mathematical Physical and Engineering Sciences*, 366(1882). <https://doi.org/10.1098/rsta.2008.0137>
- Lilly, D. (1968). Models of cloud-topped mixed layers under a strong inversion. *Quarterly Journal of the Royal Meteorological Society*, 94(401), 292–309. <https://doi.org/10.1002/qj.49709440106>
- Lu, M., Conant, W., Jonnson, H., Varutbangkul, V., Flagan, R., & Seinfeld, J. (2007). The marine stratus/stratocumulus experiment (mase): Aerosol–cloud relationships in marine stratocumulus. *Journal of Geophysical Research, Atmospheres*, 112(D10). <https://doi.org/10.1029/2006JD007985>
- Olivier, J., & Peters, J. (2020). *Trends in global co2 and total greenhouse gas emissions* (tech. rep.). PBL Netherlands Environmental Assessment Agency.
- Pincus, R., & Stevens, B. (2009). Monte carlo spectral integration: A consistent approximation for radiative transfer in large eddy simulations. *Journal of Advances in Modeling Earth Systems*, 1(2). <https://doi.org/10.3894/JAMES.2009.1.1>
- Possner, A., Eastman, R., Bender, F., & Glassmeier, F. (2020). Deconvolution of boundary layer depth and aerosol constraints on cloud water path in subtropical stratocumulus decks. *Atmospheric Chemistry and Physics*, 20, 3609–3621. <https://doi.org/10.5194/acp-20-3609-2020>
- Possner, A., Wang, H., Wood, R. C. K., & Ackerman, T. (2018). The efficacy of aerosol–cloud radiative perturbations from near-surface emissions in deep open-cell stratocumuli. *Atmospheric Chemistry and Physics*, 18, 17475–17488. <https://doi.org/10.5194/acp-18-17475-2018>
- Sagaut, P. (2006). *Large eddy simulation for incompressible flows: An introduction*. Springer Science & Business Media.
- Salter, S., Sortino, G., & Latham, J. (2008). Sea-going hardware for the cloud albedo method of reversing global warming. *Philosophical Transactions of the Royal Society A-Mathematical Physical and Engineering Sciences*, 366(1882), 3989–4006. <https://doi.org/10.1098/rsta.2008.0136>
- Schmaltz, J. (E. O. I. (2013). Ship tracks off north america. Retrieved June 7, 2021, from <https://earthobservatory.nasa.gov/images/80203/ship-tracks-off-north-america>
- Stevens, B., & Feingold, G. (2009). Untangling aerosol effects on clouds and precipitation in a buffered system. *Nature*, 461, 607–613. <https://doi.org/10.1038/nature08281>
- Stevens, B., Lenschow, D., & Savic-Jovcic, V. (2001). *Dycoms-ii* (tech. rep.).
- Stevens, B., Lenschow, D., Vali, G., Faloona, I., Moeng, C., Lilly, D., Blomquist, B., Bandy, A., Campos, T., Gerber, H., Haimov, S., Morley, B., & Thorton, D. (2003). On entrainment rates in nocturnal marine stratocumulus. *Quarterly Journal of the Royal Meteorological Society*, 129(595), 3469–3493. <https://doi.org/10.1256/qj.02.202>
- Stevens, B., Moeng, C., Ackerman, A., Bretherton, C., Chlond, A., De Roode, S., Edwards, J., Golaz, J., Jiang, H., Khairoutdinov, M., Kirkpatrick, M., Lewellen, D., Lock, A., Müller, F., Stevens, D., Whelan, E., & Zhu, P. (2005). Evaluation of large-eddy simulations

- via observations of nocturnal marine stratocumulus. *Monthly Weather Review*, 133(6), 443–462. <https://doi.org/10.1175/MWR2930.1>
- Stjern, C., Muri, H., Ahlm, L., Boucher, O., Cole, J., Ji, D., Jones, A., Haywood, J., Kravitz, B., Lenton, A., Moore, J., Niemeier, U., Phipps, S., Schmidt, H., Watanabe, S., & Kristjánsson, J. (2018). Response to marine cloud brightening in a multi-model ensemble. *Atmospheric Chemistry and Physics*, 18, 621–634. <https://doi.org/10.5194/acp-18-621-2018>
- Twohy, C., Petters, M., Snider, J., Stevens, B., Tahnk, M., W. Wetzel, Russell, L., & Burnet, F. (2005). Evaluation of the aerosol indirect effect in marine stratocumulus clouds: Droplet number, size, liquid water path, and radiative impact. *Journal of Geophysical Research, Atmospheres*, 110(D8). <https://doi.org/10.1029/2004JD005116>
- Twomey, S. (1974). Pollution and the planetary albedo. *Atmospheric Environment*, 8(12), 1251–1256. [https://doi.org/10.1016/0004-6981\(74\)90004-3](https://doi.org/10.1016/0004-6981(74)90004-3)
- Van der Dussen, J., De Roode, S., & Siebesma, A. P. (2014). Factors controlling rapid stratocumulus cloud thinning. *Journal of the Atmospheric Sciences*, 71(2), 655–664. <https://doi.org/10.1175/JAS-D-13-0114.1>
- Vaughan, N., & Lenton, T. (2011). A review of climate geoengineering proposals. *Climatic Change*, 109(3-4), 745–790. <https://doi.org/10.1007/s10584-011-0027-7>
- Wang, H., Rasch, P., & Feingold, G. (2011). Manipulating marine stratocumulus cloud amount and albedo: A process-modelling study of aerosol-cloud-precipitation interactions in response to injection of cloud condensation nuclei. *Atmospheric Chemistry and Physics*, 11, 4237–4249. <https://doi.org/10.5194/acp-11-4237-2011>
- Wang, T., Skamarock, W., & Feingold, G. (2009). Evaluation of scalar advection schemes in the advanced research wrf model using large-eddy simulations of aerosol–cloud interactions. *Monthly Weather Review*, 137(8), 2547–2558. <https://doi.org/10.1175/2009MWR2820.1>
- Wang, Y., Niu, S., Lu, C., Fan, S., Lv, J., Xu, X., Jin, Y., & Sun, W. (2021). A new ccn activation parameterization and its potential influences on aerosol indirect effects. *Atmospheric Research*, 253, 105491. <https://doi.org/10.1016/j.atmosres.2021.105491>
- Wismans, L. (2020). We kunnen het klimaat ook vertimmeren. *NRC*. Retrieved June 7, 2021, from <https://www.nrc.nl/nieuws/2020/06/19/knutselen-aan-het-klimaat-a4003371>
- Wood, R. (2007). Cancellation of aerosol indirect effects in marine stratocumulus through cloud thinning. *Journal of the Atmospheric Sciences*, 64(7), 2657–2669. <https://doi.org/10.1175/JAS3942.1>
- Wood, R. (2012). *Stratocumulus clouds* (tech. rep.). University of Washington, Seattle, Washington.
- Wood, R., & Ackerman, T. (2013). Defining success and limits of field experiments to test geoengineering by marine cloud brightening. *Climate Change*, 121, 459–472. <https://doi.org/10.1007/s10584-013-0932-z>
- Zhang, Y., Stevens, B., & Ghil, M. (2005). On the diurnal cycle and susceptibility to aerosol concentration in a stratocumulus-topped mixed layer. *Quarterly Journal of the Royal Meteorological Society*, 131(608), 1567–1583. <https://doi.org/10.1256/qj.04.103>
- Zheng, Y., Rosenfeld, D., & Li, Z. (2018). The relationships between cloud top radiative cooling rates, surface latent heat fluxes, and cloud-base heights in marine stratocumulus. *Journal of Geophysical Research: Atmospheres*, 123(20), 11678–11690. <https://doi.org/10.1029/2018JD028579>
- Zhou, X., Heus, T., & Kollias, P. (2017). Influences of drizzle on stratocumulus cloudiness and organization. *Journal of Geophysical Research*, 122(13), 6989–7003. <https://doi.org/10.1002/2017JD026641>

-
- Zhu, Y., Zhang, Z., & Crabbe, M. (2021). Extreme climate response to marine cloud brightening in the arid sahara-sahel-arabian peninsula zone. *International Journal of Climate Change and Management*. <https://doi.org/10.1108/IJCCSM-06-2020-0051>



Governing Equations of DALES

The prognostic variables in DALES are the three velocity components u_i , the liquid water potential temperature θ_l , the total water mixing ratio q_t and in our simulations three scalars: the rainwater droplet number concentration $N_{d,rain}$, the rainwater mixing ratio q_{rain} , and the aerosol number concentration $N_{ae,kg}$. The turbulence kinetic energy e is an additional prognostic variable used in parameterising sub-filter scale dynamics. These variables, for example θ , can be written as the sum of the filtered part $\tilde{\theta}$ and the sub-grid part θ' :

$$\theta = \tilde{\theta} + \theta' \quad (\text{A.1})$$

If we apply the LES filtering to, for example, the heat equation, the filtering procedure is as follows:

$$\frac{\partial \theta}{\partial t} + \frac{\partial u\theta}{\partial x} + \frac{\partial v\theta}{\partial y} + \frac{\partial w\theta}{\partial z} = 0 \quad (\text{A.2})$$

$$\frac{\partial(\tilde{\theta} + \theta')}{\partial t} + \frac{\partial(\tilde{u} + u')(\tilde{\theta} + \theta')}{\partial x} + \frac{\partial(\tilde{v} + v')(\tilde{\theta} + \theta')}{\partial y} + \frac{\partial(\tilde{w} + w')(\tilde{\theta} + \theta')}{\partial z} = 0 \quad (\text{A.3})$$

When the equation above is filtered again and it is assumed that $\tilde{\tilde{\theta}} = \tilde{\theta}$ and $\tilde{\theta}' = 0$, it reduces to:

$$\frac{\partial \tilde{\theta}}{\partial t} + \frac{\partial \tilde{u}\tilde{\theta}}{\partial t} + \frac{\partial \tilde{v}\tilde{\theta}}{\partial t} + \frac{\partial \tilde{w}\tilde{\theta}}{\partial t} = -\frac{\partial \tilde{u}'\tilde{\theta}'}{\partial t} - \frac{\partial \tilde{v}'\tilde{\theta}'}{\partial t} - \frac{\partial \tilde{w}'\tilde{\theta}'}{\partial t}, \quad (\text{A.4})$$

where $\frac{\partial \tilde{\theta}}{\partial t}$ represents the tendency, $\frac{\partial \tilde{u}\tilde{\theta}}{\partial t} + \frac{\partial \tilde{v}\tilde{\theta}}{\partial t} + \frac{\partial \tilde{w}\tilde{\theta}}{\partial t}$ represents the resolved flux and $-\frac{\partial \tilde{u}'\tilde{\theta}'}{\partial t} - \frac{\partial \tilde{v}'\tilde{\theta}'}{\partial t} - \frac{\partial \tilde{w}'\tilde{\theta}'}{\partial t}$ represents the sub-grid flux of θ , which requires parameterisation. In DALES, the Boussinesq approximation is assumed and with the application of the filtering, the Navier-Stokes equations can be written as (Heus et al., 2010):

$$\frac{\partial \tilde{u}_i}{\partial x_i} = 0 \quad (\text{A.5})$$

$$\frac{\partial \tilde{u}_i}{\partial t} = -\frac{\partial \tilde{u}_i \tilde{u}_j}{\partial x_j} - \frac{\partial \pi}{\partial x_i} + \frac{g}{\theta_{l,0}} \tilde{\theta}_v \delta_{i3} + \mathcal{F}_i - \frac{\partial \tau_{ij}}{\partial x_j} \quad (\text{A.6})$$

$$\frac{\partial \tilde{\phi}}{\partial t} = -\frac{\partial \tilde{u}_j \tilde{\phi}}{\partial x_j} - \frac{\partial R_{u_j, \phi}}{\partial x_j} + \mathcal{S}_\phi, \quad (\text{A.7})$$

Here, ϕ represents the variables θ_l , q_t , q_{rain} , $N_{d,rain}$ and $N_{ae,k,g}$. π is the modified pressure and is written as $\pi = \frac{\tilde{p}}{\rho_0} + \frac{2}{3}e$, the virtual potential temperature $\theta_v = \theta(1 + \epsilon_I q_v)$ with $\epsilon_I \approx 0.608$ a thermodynamic constant, δ_{ij} is the Kronecker delta and \mathcal{F}_i represents other forcings, including the Coriolis acceleration. $R_{u_j,\phi}$ represents the sub-filter-scale scalar fluxes and the sub-grid momentum flux arising from the filtering procedure is given by $\tau_{ij} \equiv u_i \tilde{u}_j - \tilde{u}_i \tilde{u}_j - \frac{2}{3}e$. S_ϕ represents the source terms for the scalar ϕ , which may include microphysical, radiative, chemical, large-scale and relaxation terms when applicable. The expression for the turbulence kinetic energy e is the following:

$$\frac{\partial e}{\partial t} = -\frac{\partial \tilde{u}_j e}{\partial x_j} - \tau_{ij} \frac{\partial \tilde{u}_i}{\partial x_j} + \frac{g}{\theta_0} R_{w,\theta_v} - \frac{\partial R_{u_j,e}}{\partial x_j} - \frac{1}{\rho_0} \frac{\partial R_{u_j,\pi}}{\partial x_j} - \epsilon, \quad (\text{A.8})$$

with g Earth's gravitational constant, θ_0 and ρ_0 the surface values of the liquid water potential temperature and the density. The sub-filter-scale turbulence kinetic energy dissipation rate is represented by ϵ and the two eddy diffusivity coefficients $R_{u_j,\phi}$ and τ_{ij} are expressed as:

$$R_{u_j,\phi} = -K_h \frac{\partial \tilde{\phi}}{\partial x_j} \quad (\text{A.9})$$

and

$$\tau_{ij} = -K_m \left(\frac{\partial \tilde{i}}{\partial x_j} + \frac{\partial \tilde{j}}{\partial x_i} \right) \quad (\text{A.10})$$

The first right-hand-side term of Eq. (A.8) is solved by the model and the second right-hand-side term can be solved with the use of Eq. (A.10). The other terms require parameterisation. The approach of the parameterisation in DALES can be found in Heus et al. (2010).

B

Choice of Advection Scheme For Aerosols

To validate that this advection scheme can be properly used for the simulations of this thesis, the order of magnitude of the produced tendencies will be mathematically determined. This will be compared to that of the 52 scheme, a scheme often used for DALES simulations, which uses fifth-order upwind advection in the horizontal and second-order upwind advection in the vertical. The analysis will be done only for the vertical advection for the Kappa scheme, as the equations can simply be modified to resemble the horizontal advection by swapping the vertical velocity for the horizontal velocity (w to u or v), the vertical coordinate to the horizontal one (k to i or j) and setting all ρ_k to unity. Moreover, a homogeneous scalar field is assumed to provide a clear view of the mathematics. In addition, the conservation of the scalar will be proven as well.

B.1. The Kappa Advection Scheme

First the Kappa advection scheme will be considered. For conciseness, this is only done for a positive vertical velocity $w > 0$ and a constant vertical grid size Δz . In this case the tendencies produced by advection for scalar ϕ at vertical levels $k - 1$ and k are:

$$\frac{d\phi_{k-1}}{dt} = -\frac{w_k}{\rho_{k-1}\Delta z} \left[\rho_{k-1}\phi_{k-1} + \frac{1}{2}A_k (\rho_{k-1}\phi_{k-1} - \rho_{k-2}\phi_{k-2}) \right] \quad (\text{B.1})$$

$$\frac{d\phi_k}{dt} = \frac{w_k}{\rho_k\Delta z} \left[\rho_{k-1}\phi_{k-1} + \frac{1}{2}A_k (\rho_{k-1}\phi_{k-1} - \rho_{k-2}\phi_{k-2}) \right] \quad (\text{B.2})$$

For every vertical level k (except for $k = 1$ and $k = 2$) Eqs. B.1 and B.2 are calculated. Together, they form the total tendency due to vertical advection:

$$\begin{aligned} \frac{d\phi_{k,tot}}{dt} &= \frac{w_k}{\rho_k\Delta z} \left[\rho_{k-1}\phi_{k-1} + \frac{1}{2}A_k (\rho_{k-1}\phi_{k-1} - \rho_{k-2}\phi_{k-2}) \right] \\ &\quad - \frac{w_{k+1}}{\rho_k\Delta z} \left[\rho_k\phi_k + \frac{1}{2}A_{k+1} (\rho_k\phi_k - \rho_{k-1}\phi_{k-1}) \right] \end{aligned} \quad (\text{B.3})$$

where ρ_k is the air density at vertical level k in kg/m^3 and ϕ_k is the scalar quantity in unit per kg of air. Without going into the derivations, A_k is defined as :

$$A_k = \max \left(0, \min \left[2r_k, \min \left(\frac{1}{3} + \frac{2}{3}r_k, 2 \right) \right] \right) \quad (\text{B.4})$$

where $\min(a,b)$ returns the minimum value of a and b , $\max(a,b)$ returns the maximum value and r_k is:

$$r_k = \frac{\rho_k \phi_k - \rho_{k-1} \phi_{k-1} + \epsilon}{\rho_{k-1} \phi_{k-1} - \rho_{k-2} \phi_{k-2} + \epsilon} \quad (\text{B.5})$$

and $\epsilon = 10^{-10}$ is added to prevent divisions by 0. For $A_k = 0$, Eqs. B.1 and B.2 reduce to $\frac{d\phi_{k-1}}{dt} = -\frac{w_k}{\rho_{k-1}\Delta Z}\rho_{k-1}\phi_{k-1}$ and $\frac{d\phi_k}{dt} = \frac{w_k}{\rho_k\Delta Z}\rho_{k-1}\phi_{k-1}$, which are the equations for the first-order upwind advection. A_k can have a maximum value of 2, which can be increased to obtain higher accuracy near the peaks with the downside of requiring much smaller time steps to maintain positivity. If this is desired, Hundsdorfer et al. (1993) showed that reducing Δz is computationally more efficient to improve the accuracy than increasing the maximum value of A_k . $A_k = \frac{1}{3} + \frac{2}{3}r_k$ returns the third-order advection scheme, whereas $A_k = 2r_k$ ensures that no negative values are produced. Additional information about the derivation of the Kappa scheme and the values for A_k can be found in the study of Hundsdorfer et al. (1993).

Assuming a strong upwind gradient ($\rho_k \phi_k \ll \rho_{k-1} \phi_{k-1}$ or $\rho_{k-1} \phi_k \ll \rho_{k-1} \phi_{k-2}$) it follows that r_k either approaches 0 or is negative and consequently A_k approaches 0 or is equal to 0. In this case, the first-order upwind advection is applied. The disadvantage of the first-order upwind advection is that it enhances numerical dissipation, causing the underestimation of the local maximum values and overestimates neighbouring values.

In this research, the scalar to which the Kappa advection scheme is applied to is the aerosol number concentration. In the cloud seeding simulations, a vertically uniform background concentration is used in units of kg^{-1} , resembling a well-mixed boundary layer. As can be seen in Eq. (B.3), the tendency due to vertical advection depends on the gradient in $\rho_k \phi_k$ rather than on the gradient in ϕ_k . In other words, a background concentration that is vertically uniform has no vertical gradients in units of number of aerosols per kg of air (kg^{-1}), but it does when expressed in units of number of aerosols per cubic meter (m^{-3}). Depending on whether a first-, second- or higher-order upwind advection scheme is applied, the associated accuracy and thereby the resulting tendencies vary.

For domains with constant scalars $\phi_k = \phi$, which is the case for homogeneous background concentrations without any sources or sinks, the Kappa scheme will always use the third-order upwind advection for $w > 0$, because $r_k = \frac{\phi(\rho_k - \rho_{k-1}) + \epsilon}{\phi(\rho_{k-1} - \rho_{k-2}) + \epsilon} \approx 1$. For a constant ϕ and approximating $r_k \approx 1$, Eq. (B.3) reduces to:

$$\begin{aligned} \frac{d\phi_{k,tot}}{dt} &\approx \frac{\phi}{\rho_k \Delta Z} \left(w_k \left[\rho_{k-1} + \frac{1}{2} (\rho_{k-1} - \rho_{k-2}) \right] - w_{k+1} \left[\rho_k + \frac{1}{2} (\rho_k - \rho_{k-1}) \right] \right) \\ &= \frac{\phi}{\rho_k \Delta Z} \left(w_k \left[\frac{3}{2} \rho_{k-1} - \frac{1}{2} \rho_{k-2} \right] - w_{k+1} \left[\frac{3}{2} \rho_k - \frac{1}{2} \rho_{k-1} \right] \right) \end{aligned} \quad (\text{B.6})$$

At the two bottom levels $k = 1$ and $k = 2$ the equations are slightly different. A_1 and A_2 are set to 0, because it requires the undefined levels of $k = 0$ and $k = -1$, which are below the surface. Hence, the first-order scheme is applied. For $k = 1$, Eq. (B.6) reduces to:

$$\frac{d\phi_{1,tot}}{dt} = -\frac{\phi}{\rho_1 \Delta Z} w_2 \rho_1 = \frac{\phi}{\Delta Z} w_2 \quad (\text{B.7})$$

For $k = 2$, the resulting total tendency is given by (again assuming $A_3 \approx 1$):

$$\frac{d\phi_{2,tot}}{dt} = \frac{\phi}{\rho_2 \Delta Z} \left(\frac{3}{2} w_2 \rho_1 - w_3 \left[\frac{3}{2} \rho_2 - \frac{1}{2} \rho_1 \right] \right) \quad (\text{B.8})$$

B.2. The 52 Advection Scheme

As mentioned earlier, the 52 advection scheme uses fifth-order upwind advection in the horizontal direction and second-order upwind advection in the vertical direction. For the vertical advection at all levels except $k = 1$ and a uniform scalar ϕ , the total vertical tendency is given by:

$$\frac{d\phi_{k,tot}}{dt} = \frac{\phi}{\rho_k \Delta z} \left(w_k \frac{\rho_{k-1} + \rho_k}{2} - w_{k+1} \frac{\rho_{k+1} + \rho_k}{2} \right) \quad (\text{B.9})$$

Rewriting this into the form of Eq. (B.6), this is equal to

$$\frac{d\phi_{k,tot}}{dt} = \frac{\phi}{\rho_k \Delta z} \left(w_k \left[\frac{3}{2} \rho_k - \frac{1}{2} \rho_{k-1} + (\rho_{k-1} - \rho_k) \right] - w_{k+1} \left[\frac{3}{2} \rho_{k+1} - \frac{1}{2} \rho_k + (\rho_k - \rho_{k+1}) \right] \right) \quad (\text{B.10})$$

For $k = 1$, the equation above reduces to:

$$\frac{d\phi_{1,tot}}{dt} = -\frac{\phi w_2}{\rho_1 \Delta z} \frac{\rho_2 + \rho_1}{2} = -\frac{\phi w_2}{\rho_1 \Delta z} \left(\frac{3}{2} \rho_2 - \frac{1}{2} \rho_1 + (\rho_1 - \rho_2) \right) \quad (\text{B.11})$$

When comparing Eq. (B.6) with Eq. (B.10) and Eq. (B.7) with Eq. (B.11), it can be noted that the equations are very similar with additional terms of the difference in air density between two upwind neighbouring cells in the 52 advection scheme. The air density gradient is relatively small compared to the air density magnitude. Therefore, it can be concluded that the order of magnitude of the vertical advection in the kappa advection scheme and the 52 advection scheme can be considered to be equal.

Horizontally, with again taking ϕ uniform, the advection in the x-direction is equal to:

$$\frac{d\phi_{i,tot}}{dt} = \frac{\phi}{\rho_k \Delta z} (w_k - w_{k+1}) \quad (\text{B.12})$$

When setting all ρ_k in Eq. (B.6) to unity and swapping w_k for u_i to obtain its horizontal counterpart, the same equation as stated above is derived, which naturally gives equal order of magnitude for the two advection schemes.

B.3. Conservation in the Kappa Advection Scheme

In order to be confident that no aerosol sinks or sources are introduced due to numerical artefacts originating from the Kappa advection scheme, the conservation of the scalar will be assessed. The scalar is said to be conserved if the following condition is met:

$$\sum_1^{k_{max}} \rho_k \phi_k(t) = \text{constant}, \quad (\text{B.13})$$

where k_{max} is the top layer of the domain. To assess the conservation, Eqs. (B.1) and (B.2) are considered. Here, the tendency at $k - 1$ is equal to the negative tendency at k scaled by $\frac{\rho_k}{\rho_{k-1}}$:

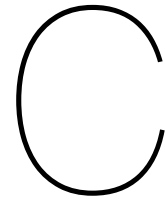
$$\frac{d\phi_{k-1}}{dt} = -\frac{d\phi_k}{dt} \frac{\rho_k}{\rho_{k-1}} \quad (\text{B.14})$$

In other words: the quantity that is advected out of grid point $k - 1$ is advected into grid point k scaled by the ratio in air density. Considering a system of two levels $k - 1$ and k and

implementing this into Eq. (B.13) gives:

$$\begin{aligned}
 \rho_{k-1}\phi_{k-1}(t) + \rho_k\phi_k(t) &= \rho_{k-1}\phi_{k-1}(t + \Delta t) + \rho_k\phi_k(t + \Delta t) \\
 &= \rho_{k-1}\left(\phi_{k-1}(t) + \frac{\Delta\phi_{k-1}}{\Delta t}\Delta t\right) + \rho_k\left(\phi_k(t) + \frac{\Delta\phi_k}{\Delta t}\Delta t\right) \\
 &= \rho_{k-1}\left(\phi_{k-1}(t) - \frac{\rho_k}{\rho_{k-1}}\frac{\Delta\phi_k}{\Delta t}\Delta t\right) + \rho_k\left(\phi_k(t) + \frac{\Delta\phi_k}{\Delta t}\Delta t\right) \\
 &= \rho_{k-1}\phi_{k-1}(t) + \rho_k\phi_k(t)
 \end{aligned} \tag{B.15}$$

Hence, the Kappa scheme ensures the conservation of aerosol number concentration and does not give rise to any numerical sinks or sources. As a final note, the output of DALES might indicate that the conservation is violated upon first impression. However, this can be attributed to the number of significant figures printed in the output file.



Additional Figures to MCB Simulations

C.1. Two-Dimensional Figures for the W50 Experiments

Figures C.1, C.2 and C.3 show the cloud albedo A_c , liquid water path LWP and the vertically integrated aerosol number concentration N_{ae} at every horizontal grid point of the W50 experiments at 6 hours, 9 hours, 12 hours, 15 hours and 18 hours into the simulation. The top row of these figures corresponds to the unseeded W50 experiment, the middle row to the uniformly seeded W50-U experiment, and the bottom row to the point source seeded W50-P experiment.

Figures C.1 and C.2 show the compact cloud structure at the beginning of the day (6 hours) for all simulations, which breaks down towards the end of the day. Most evident at 6 hours and 9 hours, the seeded experiments W50-U and W50-P show a slightly higher LWP and cloud albedo compared to W50 as a result of the aerosol injection.

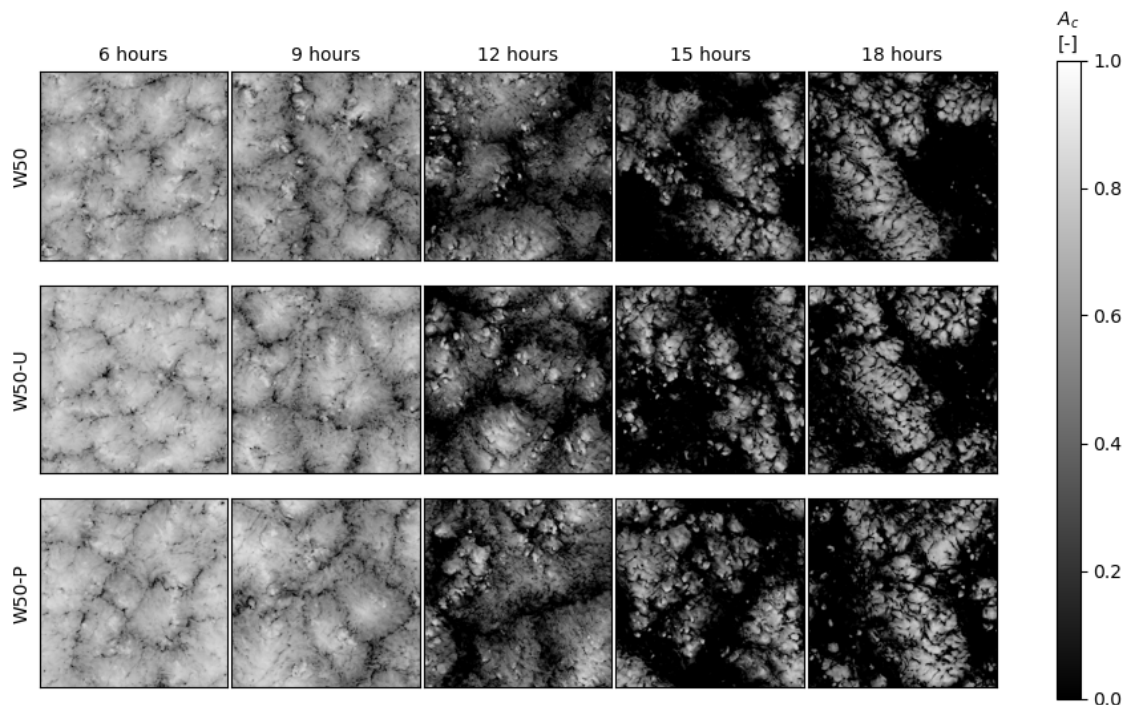


Figure C.1: Cloud albedo A_c for every horizontal grid point at 6 hours, 9 hours, 12 hours, 15 hours and 18 hours into the simulation of the W50 experiments. The top row illustrations show the results of the unseeded W50 experiment, the middle row corresponds to the uniformly seeded W50-U experiment and the bottom row corresponds to the point source seeded W50-P experiments.

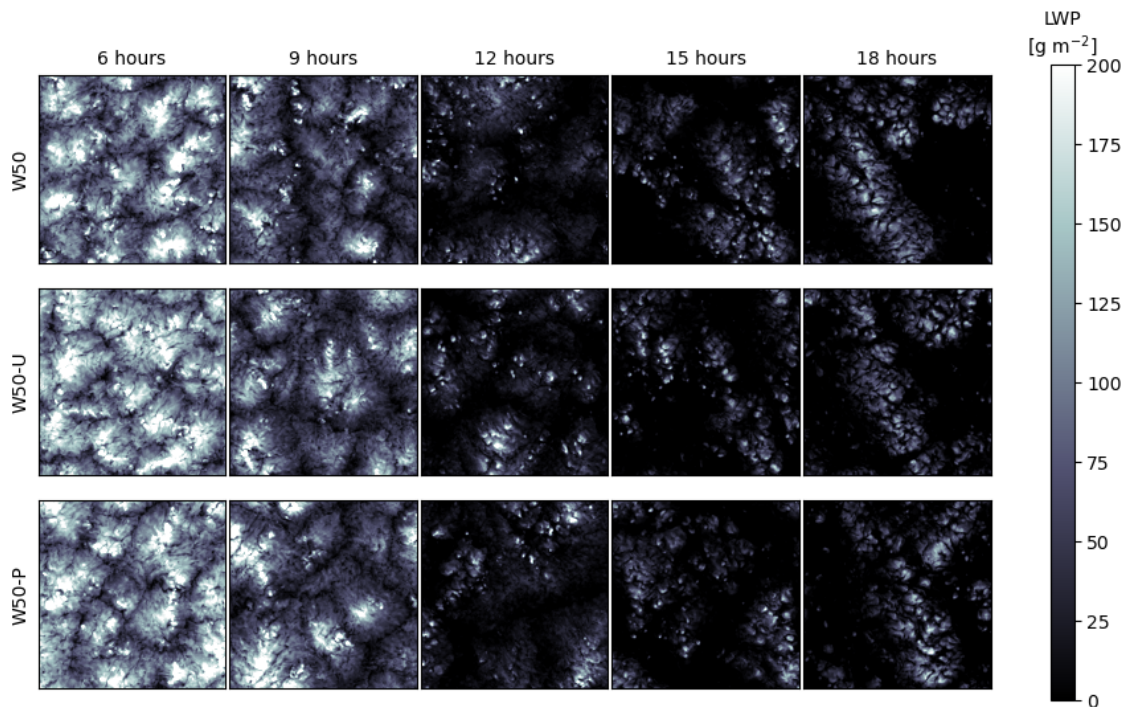


Figure C.2: Same as in Figure C.1, but showing the liquid water path LWP.

Figure C.3 shows the vertically integrated N_{ae} to illustrate the difference in aerosol distribution. The values are clipped to a maximum of $275 \cdot 10^4 \text{ mm}^{-2}$, as the results would be obscured by the extremely high concentrations near the point source. It must therefore be noted that the pronounced dark red band in the bottom row illustrations is caused by sub-cloud aerosol concentrations. These local variations in concentration are retrieved in the cloud layer as well, although much more diluted throughout the domain. The middle row illustrations, corresponding to the uniform aerosol source, shows the expected approximate uniform distribution of aerosol concentration throughout the domain. Variations are caused by local gradients in velocity, causing the uniform distribution to be slightly disturbed. The bottom row illustrations, which correspond to the aerosol point source, show more variability in the aerosol concentration. This is especially the case near the beginning of the day, showing a higher aerosol concentration near the sides and a lower aerosol concentration in the middle of the domain compared to that of W50-U.

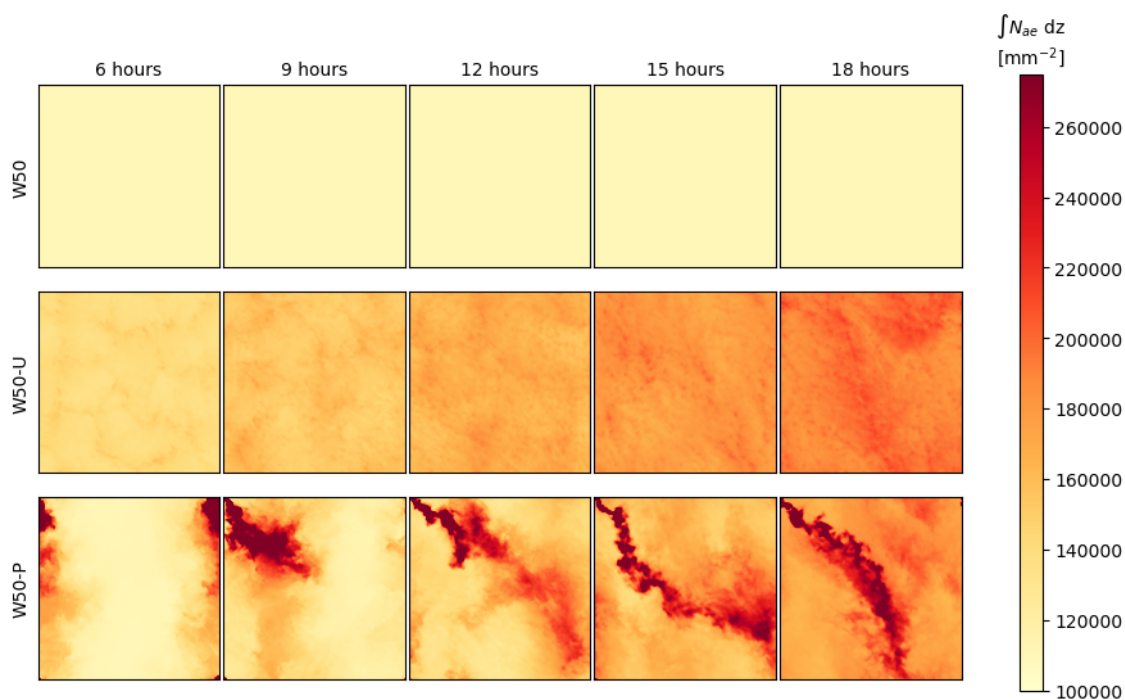


Figure C.3: Same as in Figure C.1, but showing the aerosol number concentration N_{ae} , integrated in the vertical. Values are clipped to a maximum of $275 \cdot 10^4 \text{ mm}^{-2}$ to prevent the results to be obscured by the highly concentrated values near the point source.

C.2. Indications of Decoupling

Figure C.4 below shows the indications for the decoupling of the W100 simulations. The negative buoyancy flux and minimum in vertical velocity variance indicate the cloud layer's decoupling from the surface layer. These indications are not seen in the profiles of the drier and warmer simulations of D100 shown in Figure C.5. The value ranges of the figures are clipped to amplify the characteristics indicating decoupling.

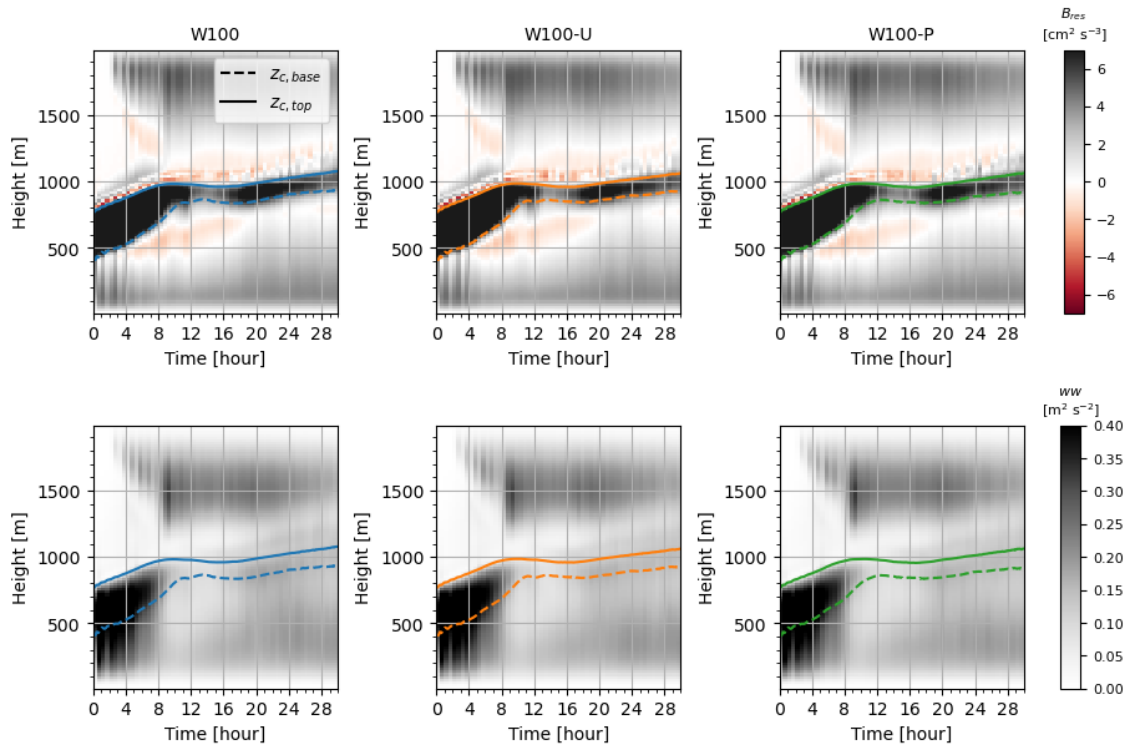


Figure C.4: The vertical profiles of the buoyancy flux (top) and vertical velocity variance for the W100 simulations. The values of all figures are clipped for visual clarity.

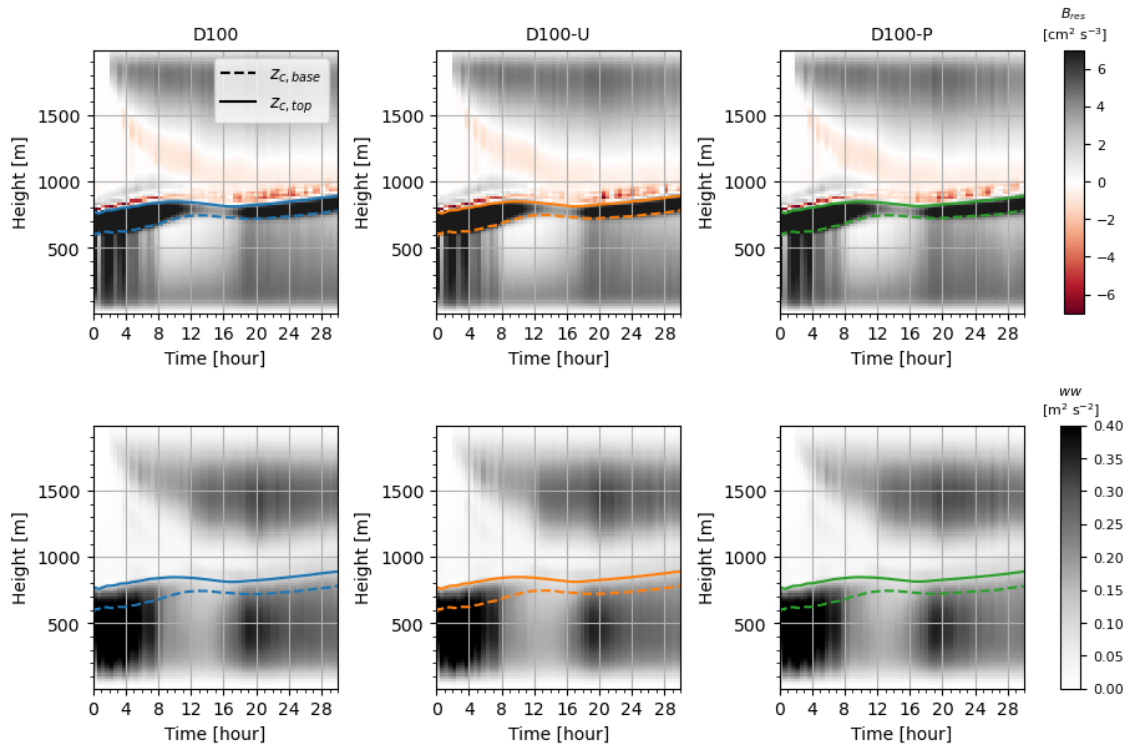
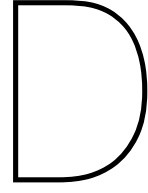


Figure C.5: Same as in Figure C.4, but for the drier and warmer D100 simulations.



Derivation of the Change of Aerosol Number Concentration in Time

The change of N_{ae} in time can be derived by starting with the budget equation:

$$\frac{\partial N_{ae}}{\partial t} = -\frac{\overline{\partial w' N'_{ae}}}{\partial z}, \quad (D.1)$$

where $\overline{w' N'_{ae}}$ is the turbulent flux of the aerosol number concentration. When assuming a well-mixed boundary layer, N_{ae} is vertically constant, which implies that the turbulent transport of N_{ae} is a linear function of height (Lilly, 1968). For a STBL with depth H , the turbulent transport of N_{ae} at height z is given by:

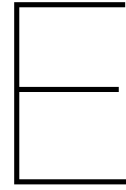
$$\overline{w' N'_{ae}} = \left(1 - \frac{z}{H}\right) \overline{w' N'_{ae}}^0 + \left(1 - \frac{H-z}{H}\right) \overline{w' N'_{ae}}^H = \left(1 - \frac{z}{H}\right) \overline{w' N'_{ae}}^0 + \frac{z}{H} \overline{w' N'_{ae}}^H, \quad (D.2)$$

where $\overline{w' N'_{ae}}^H$ is the turbulent flux of N_{ae} at the top of the STBL and $\overline{w' N'_{ae}}^0$ that at the surface. Applying Eq. (D.1) to Eq. (D.2) gives:

$$\frac{\partial N_{ae}}{\partial t} = \frac{\overline{w' N'_{ae}}^0 - \overline{w' N'_{ae}}^H}{H} \quad (D.3)$$

Considering the flux-jump relation by Lilly (1968), the turbulent flux of N_{ae} is rewritten to $\overline{w' N'_{ae}}^H = -w_e \Delta N_{ae}$, with ΔN_{ae} the difference in the aerosol number concentration just above the inversion height (N_{ae}^+) and just below the inversion height (N_{ae}^-). With $\overline{w' N'_{ae}}^0$ being the surface spraying rate $S_{N_{ae}}$, Eq. (D.3) can be rewritten to obtain the change of N_{ae} in the STBL over time:

$$\frac{\partial N_{ae}}{\partial t} = \frac{S_{N_{ae}} + w_e \Delta N_{ae}}{H} \quad (D.4)$$



Horizontal Boundary Nudging

DALES makes use of horizontal periodic boundary conditions, which causes advected atmospheric properties such as water or aerosols that are advected out of the domain at one side to be advected back into the domain at the opposite side. As stated in Subsection 3.2.2, when applying a surface aerosol source, this results in a simulated domain that can be regarded as a domain that is part of a larger system of equal domains from which the aerosols can be advected into our simulated domain. As a result of the horizontal periodic boundary conditions, these simulations do not represent the effects of aerosol injection for domains near the edges of this larger system or for isolated domains, for which the aerosols are not advected back into the domain. To simulate such domains, the diffusion of the aerosol number concentration N_{ae} near the domain's edges requires to be included in the simulation.

Based on the work of the former TU Delft master Student P.A. van Dorp, we developed a module that makes use of a cosine function to parameterise the diffusion near the edges of the domain, also known as nudging, of the scalar that represents N_{ae} (N_{ae_b}) to a predefined constant value. N_{ae_0} resembles the background N_{ae} value outside of the simulated domain. The strength of the diffusion can be regulated by adjusting the so-called nudge depth ($nudgedepthgr$), which is the number of grid points taken from the edges of the domain at which the diffusion is initiated.

Here, we explain the basic idea of the implementation of the aerosol number concentration diffusion. The Fortran90 code of the modules will be given hereafter. First, the nudge forcing ($fnudge$), the relative degree of nudging and ranges from 0 to 1, is calculated for each grid point from 0 to $nudgedepthgr$. Next, these values are written to the $fnudgeglob$ array, which stores the $fnudge$ values for each grid point within the $nudgedepthgr$ distance of the edges and is equal to 0 otherwise:

```
do i=1,nudgedepthgr
  fnudge = 0.5 + 0.5 * COS((pi/(nudgedepthgr-1))*(i-1))

  fnudgeglob( i           , i:(jtot-(i-1)) , :) = fnudge
  fnudgeglob( itot-(i-1)  , i:(jtot-(i-1)) , :) = fnudge
  fnudgeglob( i:(itot-(i-1)) , i           , :) = fnudge
  fnudgeglob( i:(itot-(i-1)) , jtot-(i-1)   , :) = fnudge
end do
```

Next, the nudging is applied to the aerosol number concentration for each grid point (ranging from $i=1$ to $i=i1$ and $j=1$ and $j=j1$ horizontally and from $k=1$ and $k=k1$ vertically), represented by the scalar $sv0(i, j, k, 3:$

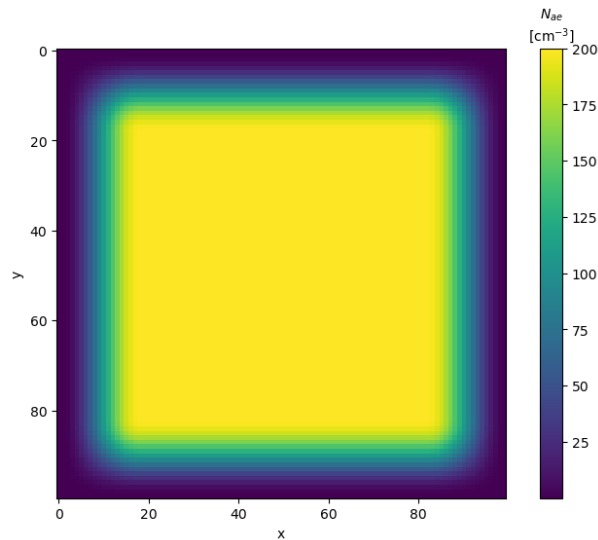


Figure E.1: Example of a horizontal domain with an initial N_{ae} of 200 cm^{-3} , which is nudged to 0 cm^{-3} towards the edges using a cosine function starting at 20 grid points from each edge.

```

do i=1,i1
do j=1,j1
do k=1,k1
sv0(i,j,k,3) = (sv0(i,j,k,3) - Nae_b) * (1 - fnudgeloc(i,j,k)) + Nae_b
enddo
enddo
endif

```

To illustrate the result of this process, Figure E.1 shows the horizontal plane of a domain for which the initial N_{ae} is set to 200 cm^{-3} and which is nudged to 0 cm^{-3} at the edges with a `nudgedepthgr` of 20 grid points.

The first module that is required to be added to incorporate the nudging of N_{ae} , is `modscalar-data.f90` in which it is defined whether the nudging is applied (`lboundary`) and the values for `nudgedepthgr` and `Nae_b`:

```

module modscalardata

implicit none
save

logical :: lboundary = .false.      !< Switch to enable sink-
sources at the boundaries: non-cyclic boundaries
integer :: nudgedepthgr = 0 ! number of nudge grid points
integer :: Nae_b = 100E+06 ! background aerosol number concentration [m^-3]
!< Field for the n-th scalar on position i,j
!integer, allocatable :: scalar_n(:, :) !< n-th scalar at grid pos x,y

end module modscalardata

```

The values for `lboundary`, `nudgedepthgr` and `Nae_b` can be adjusted by simply adding the code below to the `namoptions` file and changing their values:

```

&NAMSCALAR
lboundary = .true.

```

```
nudgedepthgr = 5
Nc_b          = 100e6
/
```

The second model that is required to be added is the modscalar.f90 module, which includes the following code:

```
module modscalar

  use modscalardata, only : lboundary, nudgedepthgr, Nae_b
  implicit none
  save
  public :: initscalardistribution, exitscalar, calcfnudge

  ! Fields
  real, allocatable :: fnudgeglob(:, :, :) ! global array of fnudge values
  real, allocatable :: fnudgeloc(:, :, :) ! local, cpu dependent array of fnudge values
  !real, allocatable :: Nae_b

contains
  subroutine initscalardistribution
    use modglobal, only : itot, jtot, ih, il, jh, jl, k1, imax, jmax, kmax, cexpnr, ifnamopt, if
    use modmpi,      only : myid, mpi_logical, comm3d, mpierr, MPI_INTEGER, myidx, myidy, my_real
    use modscalardata, only : lboundary, nudgedepthgr, Nae_b
    implicit none

    integer          :: i, j, k, ierr, kmin
    character(600)  :: readstring

    namelist/NAMSCALAR/ lboundary, nudgedepthgr, Nae_0

    write(6,*) 'initscalar distribution started'
    if(myid==0) then !first myid
      open(ifnamopt, file=fname_options, status='old', iostat=ierr)
      read (ifnamopt, NAMSCALAR, iostat=ierr)
      if (ierr > 0) then
        print *, 'Problem in namoptions NAMSCALAR'
        print *, 'iostat error: ', ierr
        stop 'ERROR: Problem in namoptions NAMSCALAR'
      endif
      write(6, NAMSCALAR)
      close(ifnamopt)
    endif

    call MPI_BCAST(lboundary, 1, mpi_logical, 0, comm3d, mpierr)
    call MPI_BCAST(nudgedepthgr, 1, mpi_integer, 0, comm3d, mpierr)
    call MPI_BCAST(Nae_b, 1, mpi_integer, 0, comm3d, mpierr)

    allocate(fnudgeglob(itot+1, jtot+1, k1+1))
    allocate(fnudgeloc(il+1, jl+1, k1+1))
    call calcfnudge

    return
  end subroutine initscalardistribution
```

```

subroutine calcfnudge
  use modglobal, only : pi, itot, jtot, kmax, il, j1, k1, imax, jmax
  use modmpi, only : myid, mpi_logical, comm3d, mpierr, myidx, myidy, my_real
  implicit none
  integer i,j,k
  real fnudge

  fnudgeglob(:, :, :) = 0.
  fnudgeglob(:, :, :) = 0.

  do i=1,nudgedepthgr
    fnudge = 0.5 + 0.5 * COS((pi/(nudgedepthgr-1))*(i-1))

    fnudgeglob( i           , i:(jtot-(i-1)) , :) = fnudge
    fnudgeglob( itot-(i-1)   , i:(jtot-(i-1)) , :) = fnudge
    fnudgeglob( i:(itot-(i-1)) , i           , :) = fnudge
    fnudgeglob( i:(itot-(i-1)) , jtot-(i-1)   , :) = fnudge
  end do

  do k=1,kmax
    do j=2,j1
      do i=2,il
        fnudgeglob(i,j,k) = fnudgeglob(iglob(i,myidx),jglob(j,myidy),k)
      end do
    end do
  end do

end subroutine calcfnudge

function iglob(iloc,myidxloc)
  use modglobal, only : imax
  implicit none
  integer iloc,iglob,myidxloc

  iglob = iloc + imax*myidxloc - 1
end function iglob

function jglob(jloc,myidyloc)
  use modglobal, only : jmax
  implicit none
  integer jloc,jglob,myidyloc

  jglob = jloc + jmax*myidyloc - 1
end function jglob

subroutine exitscalar
  use modmpi, only : myid
  implicit none
  write(6,*) 'Deallocating fnudgeglob'
  deallocate(fnudgeglob)
  write(6,*) 'Deallocating fnudgeglob'
  deallocate(fnudgeglob)
  !write(6,*) 'Deallocating Nae_b'

```

```

!deallocate(Nae_0)
if(myid==0) write(6,*) 'Finished with exitscalar'

```

```

return
end subroutine exitscalar

```

```
end module modscalar
```

Then, the module that regulates the boundary conditions in DALES, `modboundary.f90`, needs to be adjusted. More specifically, the subroutine *cyclich* is modified to:

```

subroutine cyclich

use modglobal,      only : il,ih,j1,jh,k1,nsv
use modfields,      only : thl0,thlm,qt0,qtm,sv0,svm
use modmpi,         only : excjs, myid
use modscalar,      only : lboundary, fnudgeloc, Nae_b
integer i,j,k,n

!call MPI_BCAST(Nc_b, 1, mpi_integer , 0, comm3d, mpierr)

call excjs( thl0      , 2,il,2,j1,1,k1,ih,jh)
call excjs( qt0       , 2,il,2,j1,1,k1,ih,jh)
call excjs( thlm      , 2,il,2,j1,1,k1,ih,jh)
call excjs( qtm       , 2,il,2,j1,1,k1,ih,jh)

do n=1,nsv
  call excjs( sv0(:, :, :, n) , 2,il,2,j1,1,k1,ih,jh)
  call excjs( svm(:, :, :, n) , 2,il,2,j1,1,k1,ih,jh)
enddo
!Added for non-periodic horizontal boundaries for scalar 3 (aerosols)
!by SdeB
if (lboundary) then
  do i=1,il
    do j=1,j1
      do k=1,k1
        sv0(i,j,k,3) = (sv0(i,j,k,3) - Nae_b) * (1 - fnudgeloc(i,j,k)) + Nae_b
        svm(i,j,k,3) = (svm(i,j,k,3) - Nae_b) * (1 - fnudgeloc(i,j,k)) + Nae_b
      enddo
    enddo
  enddo
endif

return
end subroutine cyclich

```

Finally, the `modstartup.f90` module should include the use-statements of the two new modules, `modscalardata.f90` and `modscalar.f90`, before the use-statement of the `modboundary.f90` module in order for DALES to be rightfully compiled and make use of the nudging of N_{ae} at the edges of the domain. The adjustment in `modstartup.f90` is in the first lines of the subroutine *startup(path)*:

```

subroutine startup(path)

!-----|
!
!   Reads all general options from namoptions
!
!   Chiel van Heerwaarden      15/06/2007
!   Thijs Heus                 15/06/2007
!-----|

use modglobal,          only : version,initglobal,iexpnr, ltotruntime,&
                        runtime, dtmax, dtav_glob,timeav_glob,&
                        lwarmstart,startfile,trestart,nsv,itot,&
                        jtot,kmax,xsize,ysize,xlat,xlon,xyear,&
                        xday,xtime,lmoist,lcoriol,lpressgrad,&
                        igrw_damp,geodamptime,lmomsubs,cu, cv,&
                        ifnamopt,fname_options,llsadv,ibasprf,&
                        lambda_crit,iadv_mom,iadv_tke,iadv_thl,&
                        iadv_qt,iadv_sv,courant,peclet,ladaptive,&
                        author,lnoclouds,lrigidlid,unudge,&
                        ntimedep,solver_id, maxiter, tolerance,&
                        n_pre, n_post, precondition, checknamelisterror

use modforces,          only : lforce_user
use modsurfdata,        only : z0,ustin,wtsurf,wqsurf,wsvsurf,ps,thls,isurf
use modsurface,         only : initsurface
use modfields,          only : initfields
use modpois,            only : initpois
use modradiation,       only : iniradiation
use modraddata,         only : irad,iradiation,rad_ls,rad_longw,&
                        rad_shortw,rad_smoke,useMcICA,timerad,rka,&
                        dlwtop,dlwbot,sw0,gc,reff,svsmoke,lcloudshading

use modtimedep,         only : inittimedep,ltimedep,ltimedepuv
use modtimedepsv,       only : inittimedepsv,ltimedepsv
use modtestbed,         only : inittestbed
use modscalardata,      only : nudgedepthgr, lboundary, Nc_b !added by SdeB
use modscalar,          only : initscalardistribution !added by SdeB
use modboundary,        only : initboundary,ksp
.
.
.

```